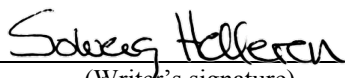




University of  
Stavanger

**Faculty of Science and Technology**

## MASTER'S THESIS

Study program/Specialization: Petroleum Geosciences Engineering	Spring semester, 2019 Open
Writer: Solveig Hellenen	 (Writer's signature)
Faculty supervisors: Dora Luz Marín Restrepo Carita Augustsson Sverre Ekrene Ohm	
Title of master's thesis: Lateral compositional variations in the Upper Jurassic source rock in the southwestern Barents Sea – an organic or inorganic disclosure	
Credits (ECTS): 30	
Keywords: Hekkingen Formation Alge Member Source rock composition Southwestern Barents Sea High-value gamma-ray spikes Uranium	Pages: 118  Stavanger, 15.06.2019

Copyright  
by  
Solveig Hellenen  
2019

**LATERAL COMPOSITIONAL VARIATIONS IN THE UPPER JURASSIC  
SOURCE ROCK IN THE SOUTHWESTERN BARENTS SEA – AN ORGANIC OR  
INORGANIC DISCLOSURE**

by

SOLVEIG HELLEREN

MASTER THESIS

Presented to the Faculty of Science and Technology

The University of Stavanger

THE UNIVERSITY OF STAVANGER

JUNE, 2019

## **ACKNOWLEDGEMENTS**

I would like to express my sincere gratitude to my supervisors Dora Marín, Carita Augustsson and Sverre Ekrene Ohm for their valuable guidance and support throughout this project.

Great thanks go to Alejandro Escalona for guidance and valuable suggestions, and to Paul Nadeau for aiding me with clay mineral interpretation.

Acknowledgements also go out to Ralph Bolanz, Frank Linde and Susanne Bock at the Friedrich-Schiller Universität Jena for valuable assistance with the XRD-analysis and the identification of clay minerals.

Thank you to the JuLoCrA Consortium sponsors; Aker BP, Equinor, DEA, Force, Lukoil, Lundin, NPD and Spirit Energy, for financial supporting this research project, Halliburton Landmark for the DesisionSpace software and Pattern Recognition Systems AS for the Sirius software.

Furthermore, a great thanks to my fellow students at the University of Stavanger, these two years of studying would not have been the same without you!

Lastly, I thank my family and friends for endless support through the duration of my studies. I could not have done this without you.

## **ABSTRACT**

### **LATERAL COMPOSITIONAL VARIATIONS IN THE UPPER JURASSIC SOURCE ROCK IN THE SOUTHWESTERN BARENTS SEA – AN ORGANIC OR INORGANIC DISCLOSURE**

Solveig Hellereen, MSc

The University of Stavanger, 2019

Supervisors: Dora Luz Marín Restrepo, Carita Augustsson & Sverre Ohm

Prominent high-value gamma-ray spikes in the maximum flooding surfaces of the Alge Member of the Hekkingen Formation display an uncommon stratigraphic and regional variation in the southwestern Barents Sea. The variation in the gamma-ray spikes indicates compositional variation in the Alge Member, thus, challenging the common perception that the Upper Jurassic source rock is a homogenous succession of black shale. The purpose of this study is to identify the compositional variation in the source rock that causes the high-value gamma-ray spikes in the Alge Member, and by comparing the lateral compositional changes in the Alge Member – be able to develop an improved understanding of the depositional environment and the paleogeography in the area during deposition. This study integrates data from X-ray diffraction of clay minerals, geochemical analysis, maceral analysis, seismic reflection data, well logs and sedimentary core logs.

The studied compositional elements of the Alge Member show no correlation to the high-value gamma-ray spike. However, their geographical distribution correlates with the depositional environments interpreted from the sedimentary core logs and the seismic facies observed in the Alge Member. West and northwest of the Loppa High, the composition of the Alge Member reveal that the deposition of the member was influenced by the ongoing rifting and uplift of the Loppa High. Whereas, in the Hammerfest Basin and in the area eastward toward and surrounding the Nordkapp Basin, the Alge Member experienced a low energy deposition in hypoxic to anoxic bottom conditions.

The high-value gamma-ray spikes are present when the Alge Member has been deposited in a hypoxic to anoxic environment. Moreover, the high-value gamma-ray spikes correlate to the uranium content in the member. The conditions that are required for uranium precipitation in the sediments could be used to reconstruct the development of the anoxic zone in the southwestern Barents Sea during the deposition of the Alge Member.

## CONTENTS

Acknowledgements .....	iv
Abstract .....	v
List of tables .....	ix
List of figures .....	xi
1. Introduction .....	1
1.1 Motivation & Objectives .....	6
2. Geological Setting .....	7
2.1 Stratigraphy .....	11
The Hekkingen Formation .....	11
3. Data & Methodology .....	14
3.1 Data .....	14
3.2 Methodology .....	16
3.2.1 X-ray Diffraction .....	16
3.2.2 Geochemical analyses .....	18
3.2.3 Maceral analysis .....	19
3.2.4 Seismic data & Well logs .....	20
3.2.5 Core logs .....	21
3.2.6 Principal Component Analysis .....	23
4. Observations & Interpretation .....	24
4.1 X-ray Diffraction .....	24
4.2 Geochemical composition .....	30
4.3 Mineral & maceral composition .....	36
4.3.1 Mineral composition .....	37
4.3.2 Maceral composition .....	41
4.4 Well logs & seismic data .....	47
4.4.1 Age & Sedimentation rate .....	47

4.4.2 Seismic reflectors & Well logs .....	51
4.4.3 Seismic facies.....	57
4.4.4 Gamma-ray signature.....	63
4.4.5 Spectral gamma-ray log .....	65
4.5 Core logs – Facies and depositional environment.....	67
4.5.1 Facies Associations.....	69
5. Discussion .....	80
5.1 Compositional variations in the Alge Member.....	80
5.2 Uranium precipitation.....	84
6. Conclusion.....	91
References .....	92

## LIST OF TABLES

<b>Table 1</b> Overview of wells, samples and performed analyses. Abbreviations: Son=sonic, Den=density, GR=gamma-ray, SGR=spectral gamma-ray, TOC=TOC-data from (NPD, 2019), Mac=maceral analysis. Data provided by JuLoCra are marked with *.	15
<b>Table 2</b> Depth of the logged core intervals and the length of the intervals in each well.	21
<b>Table 3</b> Overview of the sampled depths and depth of the MFSs in the Alge Member. The listed prominence of the spike is relative to the overall gamma-ray signature in the Alge Member. The stated depth for the MFS represents the depth where the peak displays the highest value in the gamma-ray log. The sampled depths marked in bold text represent a sampled depth that belongs to a MFS spike, although the centre of the spike is not always collected. All core samples are marked with a *.	22
<b>Table 4</b> Results from the XRD. The distribution of the clay minerals and pyrite. Samples in green are from the Krill Member, the samples in blue is from the Fuglen Formation.	24
<b>Table 5</b> The variables that correspond with the PCs, causing the greatest deviation in the data set. The variables with positive or negative value the furthest from zero correlate the strongest to the principal component.	26
<b>Table 6</b> Division of the samples into groups and subgroups based on mineral composition after the PCA.	26
<b>Table 7</b> Results from the Rock-Eval pyrolysis and TOC measurements. Well and depth marked with green are from the Krill Member, while blue is from the Fuglen Formation.	31
<b>Table 8</b> The variables in the geochemical composition that have the strongest correlation with the principal components, and thus causing the greatest variation in the dataset. The variables with positive or negative value the furthest from zero correlate the strongest to the principal component.	34
<b>Table 9</b> The counted grains for the maceral analysis, here divided into minerals and maceral groups. The wells and depths marked with green are from the Krill Member, whereas the blue belongs to the Fuglen Formation. The grouping named others comprise the minerals with overall few counts, and include calcite, chitin and sulfides.	36
<b>Table 10</b> The types of counted macerals present in the samples. The wells and depths marked with green are from the Krill Member, while the blue belongs to the Fuglen Formation.	43
<b>Table 11</b> The variables causing the most variation in the mineral and maceral data according to a PCA. The variables with positive or negative value the farthest from zero correlate the strongest to the principal component.	45

<b>Table 12</b> The ages and depths used to calculate the sedimentation rate for the Alge Member (NPD, 2019). .....	48
<b>Table 13</b> Calculation of the timespan needed to deposit a prominent high-value gamma-ray spike from the thickness of the spike and the sedimentation rate from Table 12. The thicknesses written in brackets represent lower value spikes at the MFSs. ....	49
<b>Table 14</b> Summary of the seismic facies identified around the studies wells. The highlighted areas represent the entire Hekkingen Formation, the dashed blue line represent top Alge Member. ....	57
<b>Table 15</b> The different gamma-ray signature observed in the wells. The signature follows the prominent spike observed in the gamma-ray log. ....	63
<b>Table 16</b> The interpreted facies from the viewed core logs.....	68
<b>Table 17</b> The facies association derived from the interpreted facies and the wells where the different facies and facies associations are observed. ....	69
<b>Table 18</b> Summary of the observed compositional variation in the sampled MFSs. ....	83
<b>Table 19</b> Summary of the possible reasons for oxia-anoxia changes leading to uranium precipitation and deposition of high-value gamma-ray spikes in the Alge Member. ....	89

## LIST OF FIGURES

- Fig. 1** Left: Bathymetric map over the Arctic Ocean modified from Jacobsen (2012) and location of the Barents Sea and the study area. Right: Study area with structural elements and the wells used in this study..... 2
- Fig. 2** Paleogeographic map of the Barents Sea during the Tithonian (Smelror et al. 2009). The map displays the deposition of the Hekkingen Formation as homogenous over large distances. This deposition would indicate a homogenous source rock, which is not the case. .... 3
- Fig. 3** Structural variation present in the study area, and the thickness variation in the Middle to Upper Jurassic succession marked with blue. Line A-A' display the thickest succession between the Loppa High and the Veslemøy High, and Middle to Upper Jurassic wedges are present in the fault blocks west of Loppa High. In the Hammerfest Basin (line B-B') the Middle to Upper Jurassic succession thins toward the Central High, whereas a thicker succession can be observed at the basin margins and in the internal graben. Line C-C' displays the thin Middle to Upper Jurassic succession eastward in the study area. The succession displays thinning over the Samson Dome, indicating halokinetic activity during deposition. Abbreviation: FC=Fault Complex. .... 4
- Fig. 4** Well correlation with sequences adapted from Koevoets et al. (2018) and map displaying the spike distribution in the southwestern Barents Sea provided by Marín (personal communication, October 15, 2018). The prominent gamma-ray spikes are marked with a yellow colour in the well correlation in the Alge Member (blue). The map displays the location of the well correlation (red line). .... 5
- Fig. 5** The geodynamic evolution of the Barents Sea region during the Late Jurassic. Modified by Smelror et al. (2009) after Ziegler (1988). .... 8
- Fig. 6** Map after Faleide et al. (2015) showing the main structural elements and the main periods of rifting and basin formation in the southwestern Barents Sea. Abbreviations: AFC=Asterias Fault Complex, BB=Bjørnøya Basin, BFC=Bjørnøya Fault Complex, HB= Harstad Basin, HFC=Hoop Fault Complex, HfB=Hammerfest Basin, LH=Loppa High, MB=Maud Basin, NB=Nordkapp Basin, OB=Ottar Basin, PSP=Polhem Subplatform, RLFC=Ringvassøy-Loppa Fault Complex, SB=Sørvestnaget Basin, SH=Stappen High, TB=Tromsø Basin, TFFC=Tromsø-Finnmark Fault Complex, VH=Veslemøy High, VVP=Vestbakken Volcanic Province. .... 9
- Fig. 7** Bottom: Map from Henriksen (2011a) showing the estimated net erosion for the Barents Sea region, variation from zero to more than 3000 m. The westernmost areas show no record of erosion, only subsidence. Top: Zoom in on the study area (marked with square on the map).

The southwestern part of the area has experienced the lower amount of erosion, compared to the rest of the study area is interpreted to have experience between 1000 and 2000 m of uplift. The interpretation by Henriksen (2011a) displays an increase in erosion toward the north and Stappen High. .... 10

**Fig. 8** Chrono- and lithostratigraphic chart for the main Jurassic and Cretaceous succession in the southwestern Barents Sea. Modified from Nøttvedt et al. (1993). .... 11

**Fig. 9** Gamma-ray logs (GR) and total organic carbon (TOC) content of the Hekkingen Formation with the members marked with blue (Alge) and green (Krill). Notice the difference in gamma-ray values and TOC-values for the two members. 7219/8-1S contain the thickest recorded succession of the Hekkingen Formation; 856 m. Well 7120/12-1 is the type well for the Hekkingen Formation while 7119/12-1 is the reference well. The vertical scale of the wells are in meters. .... 12

**Fig. 10** Cores from the Krill (top row) and Alge (bottom row) members show the differences in lithology between the two members and within the members. The sand rich successions of the Krill Member have been interpreted as clastic wedges (Braut 2018). The black shale of the Alge Member displays some variations in colour, texture (massive vs. brittle) and sedimentary structures (visible lamination in 7219/8-1S). A blue dashed line in the top left picture represent the transition between the Krill and the Alge members in well 7120/2-2. .... 13

**Fig. 11** Overview of the utilized seismic lines and surveys in the study. The blue lines represent 2D-lines and the grey squares represent 3D surveys. .... 16

**Fig. 12** Synthetic seismogram of well 7220/5-2 (Nunatak). Top and base of the Hekkingen Formation and the two MFS's of interest are marked. The wavelets are the Butterworth wavelet used for the synthetic seismogram (red), and an extracted wavelet from the Hekkingen Formation (black). The extracted wavelet peak at 37 Hz, but show a frequency-range of 25-45Hz. .... 20

**Fig. 13** XRD-measurements to illustrate the position of the clay-mineral peaks and the changes due to saturation and heat treatment, marked with red arrows. Abbreviations: I/S=interlayered smectite-illite, K=kaolinite, I=illite, Qz=quartz, Cr=corundum. .... 25

**Fig. 14** Transformation of interlayered illite-smectite to illite as the depths get shallower. The sampled depth in meters is marked to the left of each graph. All displayed measurements are from the airdried sample. Abbreviations: I/S=interlayered smectite-illite, K=kaolinite, I=illite, Qz=quartz, Cr=corundum, Py=pyrite. .... 25

**Fig. 15** A representative graph for each of the main clay-composition groups. The graph for group 1 (7219/8-1-4275.27) only has the peaks representing illite (I). Group 2 (7324/8-1-600)

displays the peaks for chlorite (Ch), interlayered illite-smectite (I/S) and kaolinite (K). Moreover, the graph for group 3 (7120/2-3S-2016) displays the peaks for interlayered illite-smectite and kaolinite. In this case, group 2 displays a high kaolinite count and belong in subgroup 2b, while group 3 displays a low kaolinite count and should be placed in 3a, but the high smectite peak (001) places the sample in 3c. Other abbreviations: Qz=quartz, Cr=corundum. .... 27

**Fig. 16** Distribution of the clay minerals by the groups defined in Table 6. The distribution showed that group 1, consisting of illite as the only clay mineral, was only occurring in one well (7219/8-1S). Group 2, containing chlorite, interlayered smectite-illite and kaolinite, was mainly concentrated on the west-northwestern side of the Loppa High. Group 3, containing smectite-illite and kaolinite, was mainly present southeast of the Loppa High and eastward. The sampled MFSs with prominent spike all belong to group 3. However, a low gamma-ray value spike was also encountered in this group. The samples belonging to group 2 had low value spikes in the sampled MFS. The current configuration of the Loppa High was marked in grey to illustrate that the area was uplifted and still uplifting at the time, but with an uncertain extent. .... 28

**Fig. 17** Pseudo van Krevelen diagram illustrating the kerogen types for the different samples from the Alge Member. The samples missing OI in the dataset (Table 7) are not represented in the plot. The Tmax value in the samples show that have the lowest HI, plotting as kerogen type III and IV, also have the highest Tmax measurements ..... 32

**Fig. 18** Map illustrating the variation in petroleum generating potential in the samples from the study area. The majority of the wells contain kerogen type I and II and are immature to early oil window based on the Tmax. The high S2 and low Tmax in several of the wells reflects great hydrocarbon production potential, but the burial of the source rock was not deep enough to start production. Please note that the values stated in this figure are the average-value of all the samples from the Alge Member collected in each well ..... 33

**Fig. 19** Sample 7120/2-3-2003 and 7220/5-2-1408 positioned themselves on opposite sides of the dataset when plotting PC1 and PC2 for the organic geochemistry against each other. The rest of the sampled spikes seem to be randomly distributed. .... 34

**Fig. 20** The mineral percentage and count for each sample. The amount of quartz and clay in the samples are inversely proportional. Note the high quartz content in 7220/5-2, 7321/9-1 and 7324/8-1, and the high pyrite content in 7120/2-3S. The samples that do not belong to the Alge Member is marked on the chart as well as sampled depths that correlate with a MFS. The MFSs in bold text have a prominent spike at the sampled depth. The grouping named others comprise

the minerals with overall few counts, and include calcite, chitin and sulphides. Abbreviation: Fm=Formation..... 37

**Fig. 21** The relationship between the clay and quartz to the gamma-ray value in API measured at the sampled depth display the relationship between quartz and clay in the samples, and display that the largest values are found in the clay-rich samples. However, low gamma-ray values can also be observed in the clay rich samples..... 38

**Fig. 22** Map with pie charts illustrating the mineral distribution in the study area. The quartz-content might be used as indicator of areas with tectonic activity. The percentage calculation is based on the mean of all the samples representing the Alge Member for each well. Values below 2 % were not display with numbers. The grouping named others comprise the minerals with overall few counts, and include calcite, chitin and sulphides. .... 39

**Fig. 23** The maceral-count for each of the samples. Solid bitumen and liptinite is the main component. The samples that do not belong to the Alge Member are marked on the chart as well as sampled depths that correlate with a MFS. The MFS's in bold text have a prominent spike at the sampled depth. .... 41

**Fig. 24** Map with pie charts illustrating the maceral distribution in the study area. The solid bitumen dominated the maceral count in most of the samples and is highlighted in the figure. The percentage calculation is based on the mean of all the samples representing the Alge Member for each well. Values below 2 % were not displayed with numbers. The wells marked in blue represent the wells with the highest maceral content. .... 42

**Fig. 25.** The amount of marine liptinite, terrestrial liptinite and vitrinite (terrestrial) in the samples. The percentage display the vertical variation in the well. The MFS's in bold text have a prominent spike at the sampled depth. .... 44

**Fig. 26** Map with pie charts illustrating the distribution of macerals grouped into marine liptinite, vitrine and terrestrial liptinite. The percentage calculation is based on the mean of all the samples representing the Alge Member for each well. .... 44

**Fig. 27** The age of the Hekkingen Formation and the MFSs (NPD, 2019). From left to right, the wells are located in the Hammerfest Basin and eastward. The black dashed lines represent the top and base of the Alge Member and the blue lines show the depth of the MFSs. Vertical scale is in m. .... 47

**Fig. 28** The age of the Hekkingen Formation and the MFSs (NPD, 2019). From left to right, the wells are located in the Ringvassøy-Loppa Fault Complex and northward on the western side of the Loppa High. The black dashed lines represent the top and base of the Alge Member and the blue lines show the depth of the MFSs. Vertical scale is in m. .... 47

<b>Fig. 29</b> Seismic reflectors of the Hekkingen Formation at well 7119/12-1 (top and base are marked with dashed lines) and the MFS's (blue marks and lines) compared to the sonic-, density- and gamma-ray logs together with the measured TOC-data for the entire succession from NPD (2019). Abbreviation GR is used for gamma-ray in the figure. ....	51
<b>Fig. 30</b> Seismic reflectors of the Hekkingen Formation at well 7120/2-2 (top and base are marked with dashed lines) and the MFS's (blue lines) compared to the sonic-, density- and gamma-ray logs together with the measured TOC-data for the entire succession from NPD (2019). Abbreviation: GR= gamma-ray. ....	52
<b>Fig. 31</b> Seismic reflectors of the Hekkingen Formation at well 7120/2-3S (top and base are marked with dashed lines) and the MFS's (blue lines) compared to the sonic-, density- and gamma-ray logs together with the measured TOC-data for the entire succession from NPD (2019). Abbreviation: GR= gamma-ray. ....	53
<b>Fig. 32</b> Seismic reflectors of the Hekkingen Formation at well 7125/1-1 (top and base are marked with dashed lines) and the MFS's (blue lines) compared to the sonic-, density- and gamma-ray logs together with the measured TOC-data for the entire succession from NPD (2019) Abbreviation: GR= gamma-ray. ....	53
<b>Fig. 33</b> Seismic reflectors of the Hekkingen Formation at well 7219/8-1S (top and base are marked with dashed lines) and the MFS's (blue lines) compared to the sonic-, density- and gamma-ray logs together with the measured TOC-data for the entire succession from NPD (2019). Abbreviation: GR= gamma-ray. ....	54
<b>Fig. 34</b> Seismic reflectors of the Hekkingen Formation at well 7220/5-2 (top and base are marked with dashed lines) and the MFS's (blue lines) compared to the sonic-, density- and gamma-ray logs together with the measured TOC-data for the entire succession from NPD (2019). Abbreviation: GR= gamma-ray. ....	55
<b>Fig. 35</b> Seismic reflectors of the Hekkingen Formation at well 7324/8-1 (top and base are marked with dashed lines) and the MFS's (blue lines) compared to the sonic-, density- and gamma-ray logs together with the measured TOC-data for the entire succession from NPD (2019). Abbreviation: GR= gamma-ray. ....	55
<b>Fig. 36</b> Distribution of the seismic facies in the study area. The wells surrounding the Nordkapp Basin, and northwards to well 7324/8-1 (Wisting) in the Hoop Fault Complex, all display low energy deposition. The seismic facies in the wells closest to the Loppa High, show sign of tectonic activity in the fault complexes and the high sediment input to well 7219/8-1S in the Bjørnøyrenna Fault Complex could be explained by erosion of a subaerial exposed island. The tectonic activity is likely to have caused the deformation structures observed in the Ringvassøy-	

Loppa Fault Complex, the Hammerfest Basin and in the Fingerdjupet Sub-basin (7321/7-1). The current configuration of the Loppa High is marked grey on the map as the amount of uplift the area had experienced during the deposition of the Hekkingen Formation is unknown. .... 62

**Fig. 37** The gamma-ray signature of the wells in the study. The top row (blue line on map) exhibit an overall low gamma-ray signature, corresponding to the wells with no prominent spikes. The lowest row contains the wells with high gamma-ray values only around one MFS (black line on map) and the erratic signature between the MFSs in the middle (green line on map). The dashed lines represent top and base of the Hekkingen Formation..... 64

**Fig. 38** Comparison of the spectral gamma-ray log and the prominent spikes. Note the correlation between increase in the uranium content and the prominent high value gamma-ray spikes. .... 66

**Fig. 39** Core photos of the identified lithofacies in the wells. a) Black shale (7125/1-1 at the depth of 1362.00 m), b) parallel laminated mudstone (7120/2-2 at the depth of 2009.80 m), c) siltstone (7120/2-3S at the depth of 2017.30 m), d) interbedded sandstone and siltstone (7219/8-1S at the depth of 4270.22 m), e) soft sediment deformation (7120/2-3S at the depth of 2003.30 m), f) parallel laminated sandstone (7120/2-2 at the depth of 2637.10 m ), and g) massive sandstone (7120/2-3S at the depth of 2018.30 m). All listed depths represent the depth at the top at the top of the photos. Photo e) display ptygmatic folding observed in 7120/2-3S, while the neighbouring, well 7120/2-2 in photo f) display a layer of flame structures toward the base of the photo. Flame structures can also be observed in d) in the middle of the lower core piece. In photo, g) the sharp and erosive boundaries between the mudstone and the sandstone in well 7120/2-3S can be observed. The line in the left lower corner of the photos represent 1 cm on the photos. .... 67

**Fig. 40** Left photo: A lense shaped pyrite nodule exhibiting zonation from well 7120/2-2, depth 2640.50. Middle photo: The bivalve fossils observed in well 7120/2-2–2642.50 show that pyrite has acted as a replacement mineral in the fossilized shell. Right photo: Woody material from well 7120/2-2, depth. The white line the left lower corner of the photos represents 1 cm. .... 70

**Fig. 41** The sandstone interpreted as sand injectites observed in well 7120/2-3S. Left: the base of the upper sandstone package display a lightly eroded base, while the top of the lower sandstone package have a sharp boundary to the overlying mudstone. Middle: Random orientation of the sandstone within the mudstone, and mud clasts is also present within the sand package. Right: Several mudclasts present within the sandstone and the sandpackage displays an erosive top. The line the left lower corner of the photos represents 1 cm..... 70

**Fig. 42** Sedimentological log and gamma-ray of well 7120/2-3S. The sampled areas are marked with a blue dot on the sedimentological log. The gamma-ray log of the entire Hekkingen Formation is included on the left side of the sedimentological logs. The location of the sedimentological log is marked in with grey on the left in the gamma-ray log. The exact depth of the core can be seen between the gamma-ray log and the sedimentological log. The vertical scales in figure are in m. .... 72

**Fig. 43** Sedimentological log and gamma-ray of well 7125/1-1 and 7228/9-1S. Both belong to FA1. The gamma-ray log of the entire Hekkingen Formation is included on the left side of the sedimentological logs. The location of the sedimentological log is marked in with grey on the left in the gamma-ray log. The exact depth of the core can be seen between the gamma-ray log and the sedimentological log. The vertical scales in figure are in m. .... 73

**Fig. 44** Left photo: transition from parallel lamination to wavy lamination toward the top of the FA in well 7120/2-2. A layer of authigenic glauconite is located at the top of the FA (marked with red arrow). Middle and right photo: The FA in well 7219/8-1, display asymmetric ripples and flaser bedding, here shown at depths 4270.00 and 4272.45, respectively. The line in the left lower corner of the photos represent 1 cm. .... 76

**Fig. 45** Sedimentological log and gamma-ray of well 7120/2-2 and 7219/8-1S. The gamma-ray log of the entire Hekkingen Formation is included on the left side of the sedimentological logs. The location of the sedimentological log is marked in with grey on the left in the gamma-ray log. The exact depth of the core can be seen between the gamma-ray log and the sedimentological log. The vertical scales in figure are in m. .... 78

**Fig. 46** The lithofacies marked around the wells and the area between in shaded colour. The Alge Member is interpreted to have low energy anoxic deposition in the Hammerfest Basin and eastward to the areas surrounding the Nordkapp Basin. On the western side of the Loppa High, the depositional environment of the Alge Member is interpreted to be a gravity flow complexes (turbidity flow). The gravity flow complexes can be linked to the tectonic activity in the fault complexes (Bjørnøyrenna Fault Complex and the Ringvassøy-Loppa Fault Complex) located on the western side of the high (Fig. 6). Note that the great distance between the wells. .... 79

**Fig. 47** Relative paleowater depth based on the maceral content in the wells and compared with the thickness of the Alge Member. The gamma-ray signature of the Alge Member can be seen to the right of the thickness of the member. The gamma-ray shows a higher-value signature in the Alge Member deposited at shallower water depths. .... 82

**Fig. 48** Conceptual model of uranium precipitation and relation to the gamma-ray signatures and the prominent gamma-ray spikes. The uranium is sourced from continental weathering and

follow the oxic water in its soluble and mobile form U(VI). The hypoxic zone allows the oxic water to encounter anoxic sediments and uranium is precipitated as U(IV). With a rapid sea-level rise, the hypoxic zone will leave a trail of precipitated uranium, whereas at shallower water depth, the hypoxic zone will be more sensitive to minor changes in sea-level and get an erratic gamma-ray signature. Areas where the Alge Member has low value gamma-ray signatures are either deposited in deep-water environment with no oxic (or uranium) input or in shallow and oxic conditions. .... 86

**Fig. 49** Paleogeographic map of the development of the anoxic zone the southwestern Barents Sea based on the model from Fig. 49 and the gamma-ray signature of the wells in the dataset. Left: Deposition of MFS2. Right: Deposition of MFS3. .... 87

**Fig. 50** Paleogeographic map of the development of the anoxic zone the southwestern Barents Sea based on the wells analysed by Marín (personal communication, October 15, 2018). Left: Deposition of MFS2. Right: Deposition of MFS3. Pink areas represent salt structures with recorded halokinetic activity during the Late Jurassic (Gabrielsen et al., 1990; Rojo & Escalona, 2018). .... 88

**Fig. 51** Conceptual sketch of distribution and preservation of uranium in the impermeable layers in the source rock. Assuming constant precipitation of uranium in anoxic conditions, the source rock would have an overall high gamma-ray reading throughout the succession. Circulation of oxic formation fluids would dissolve the precipitated uranium in the permeable layers of the source rock (illustrated with blue), leaving the uranium in the impermeable layers which caused the prominent spikes in the gamma-ray log. .... 90

## 1. INTRODUCTION

An estimate done by the Norwegian Oil Directorate shows that half of the Norwegian oil and gas yet to be discovered is located in the Barents Sea region (Fig. 1; Oljedirektoratet, 2019). The Barents Sea region has been in the focus of petroleum exploration since the first licenses were awarded in the start of the 1980s, but there is still limited information and understanding of the petroleum potential in the area (Smelror et al., 2009). The area has undergone different extensional events, and extensive uplift and erosion during the Cenozoic, complicating the prospectivity and petroleum systems in the area (Nyland et al., 1992; Riis & Fjeldskaar, 1992; Ohm et al., 2008; Henriksen et al., 2011a). The most widespread deposition of organic-rich shale in the Arctic region occurred during the Late Jurassic (Leith et al., 1993). This organic-rich shale is known in the Barents Sea as the Hekkingen Formation and it is time equivalent to the Kimmeridge Clay of the North Sea. The Hekkingen Formation is the most prolific source rock present in the Barents Sea, and also functions as an important cap rock in the southwestern Barents Sea (Gabrielsen & Kløvjan, 1997). The geochemical aspect of the formation is widely studied due to its importance for the hydrocarbon production in the Barents Sea, but there has been a limited focus on the lateral compositional and depositional variation within the formation (Leith et al., 1993).

Current knowledge suggests that deposition of the Hekkingen Formation occurred during an early stage of rift initiation, which caused diachronous faulting and uplift (Ohm et al., 2008; Henriksen et al., 2011a; Marín et al., 2018). In addition, a regional transgressional event reached its maximum during Late Jurassic time, causing the detritus to be deposited in a restricted to open shelf environment (Leith et al., 1993). Paleogeographic interpretations commonly display the Hekkingen Formation to have a homogenous depositional environment over large areas (Fig. 2; Smelror et al. 2009), but the formation shows great variation in thickness and composition both laterally and vertically (Fig. 3; Braut, 2018). Therefore, the current knowledge on the controls on the deposition of the Hekkingen Formation, its geographical distribution and compositional variations seems to be too general.

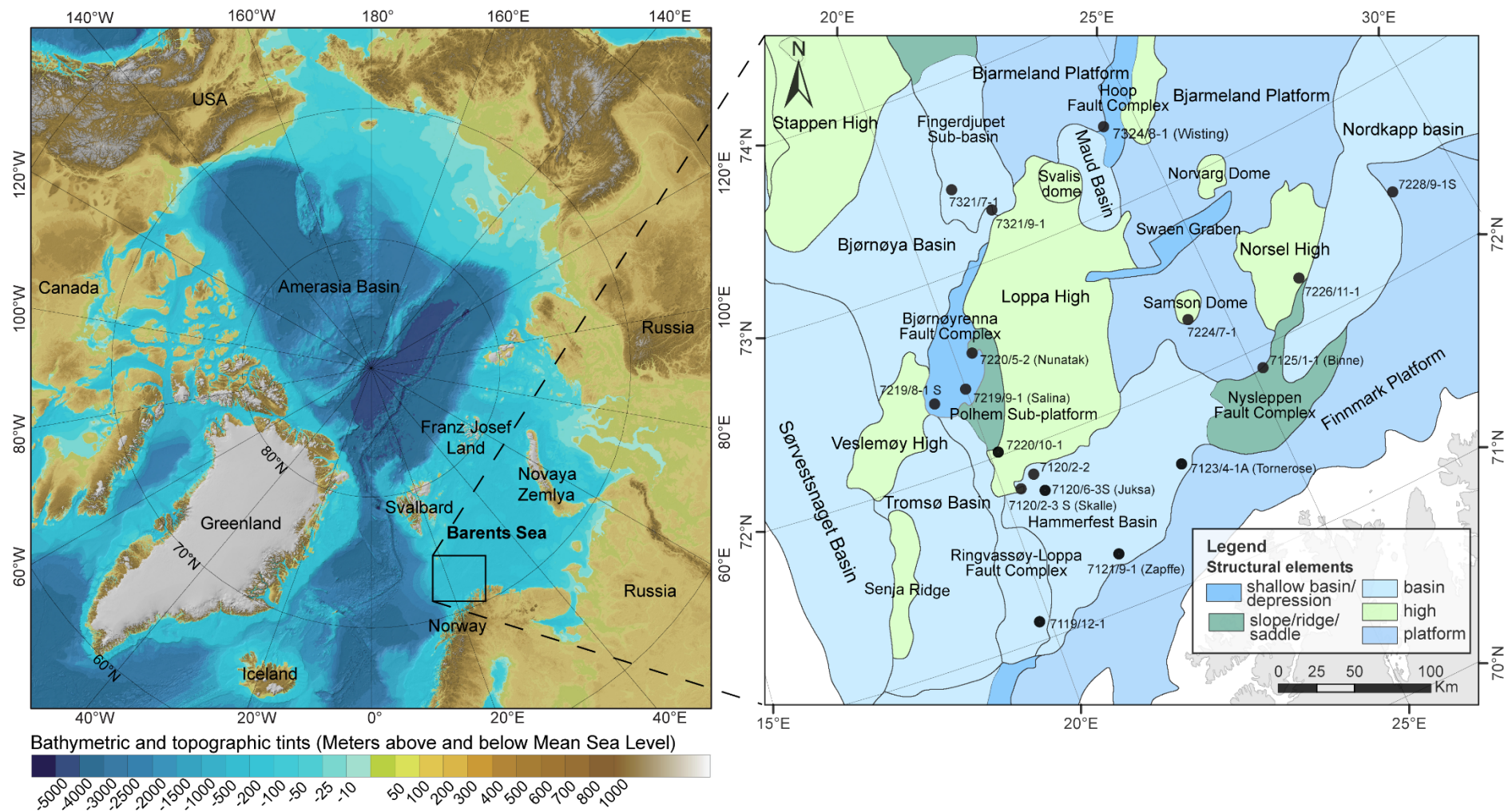


**Fig. 1** Left: Bathymetric map over the Arctic Ocean modified from Jacobsen (2012) and location of the Barents Sea and the study area. Right: Study area with structural elements and the wells used in this study.

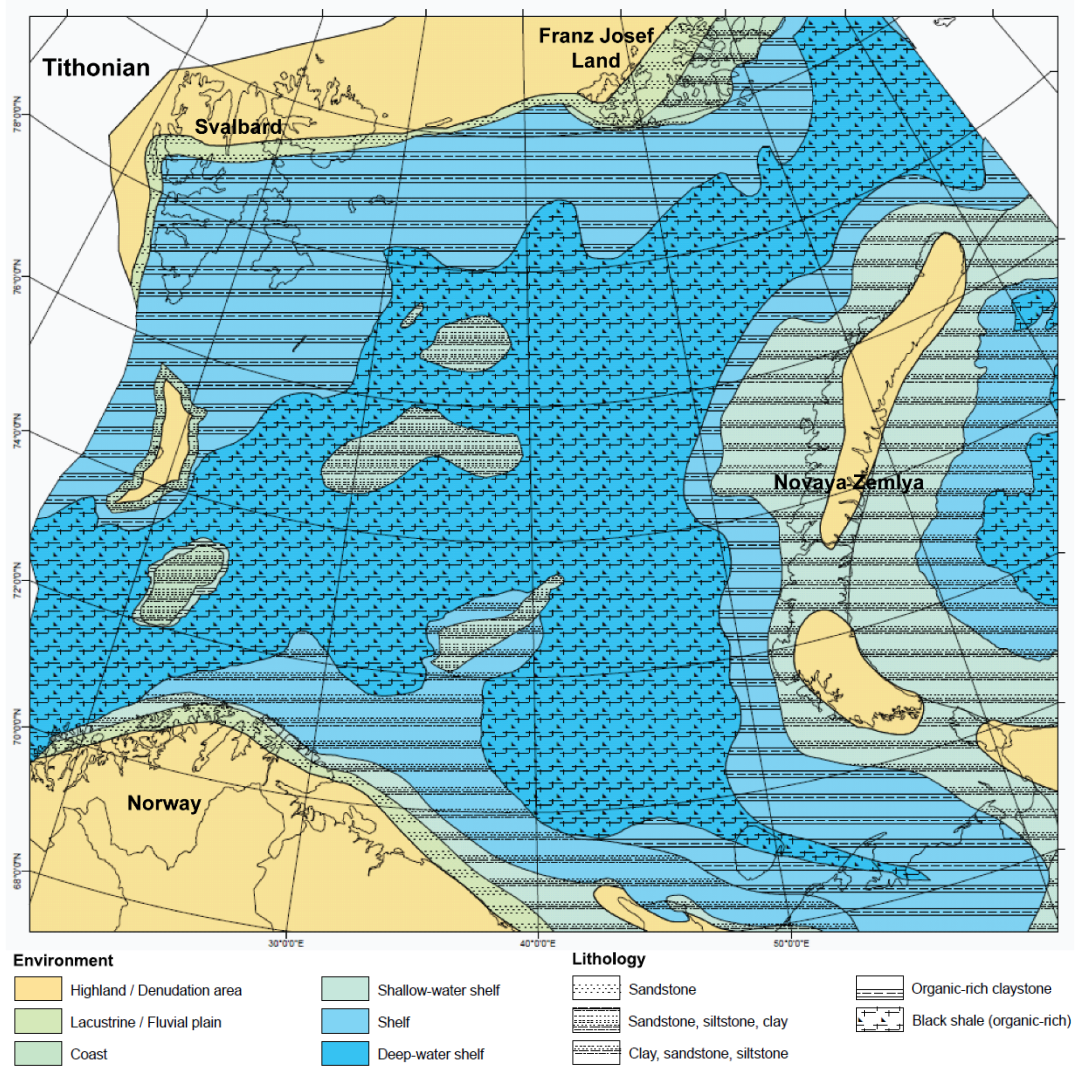


**Fig. 2** Paleogeographic map of the Barents Sea during the Tithonian (Smelror et al. 2009). The map displays the deposition of the Hekkingen Formation as homogenous over large distances. This deposition would indicate a homogenous source rock, which is not the case.

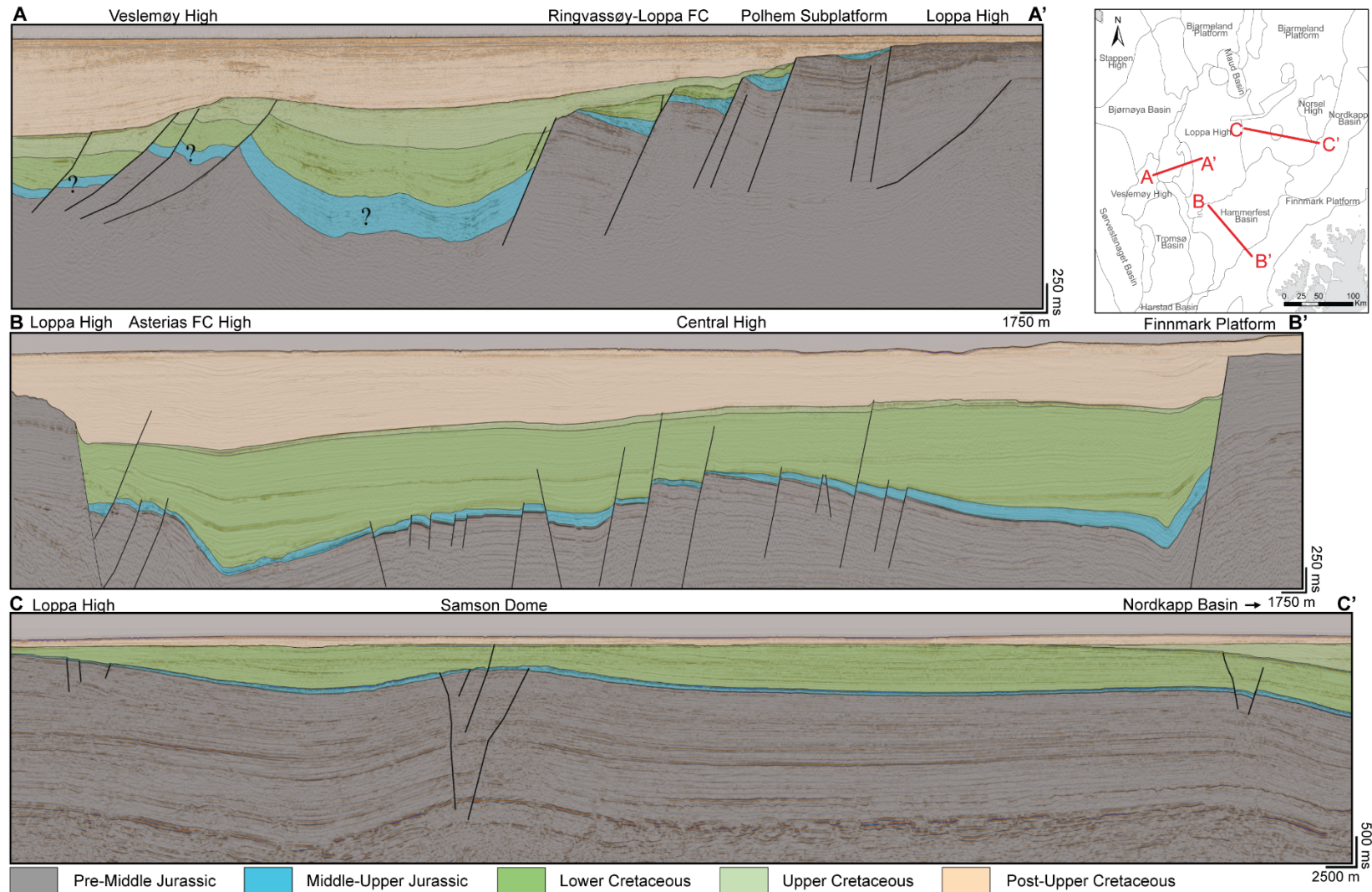


**Fig. 3** Structural variation present in the study area, and the thickness variation in the Middle to Upper Jurassic succession marked with blue. Line A-A' display the thickest succession between the Loppa High and the Veslemøy High, and Middle to Upper Jurassic wedges are present in the fault blocks west of Loppa High. In the Hammerfest Basin (line B-B') the Middle to Upper Jurassic succession thins toward the Central High, whereas a thicker succession can be observed at the basin margins and in the internal graben. Line C-C' displays the thin Middle to Upper Jurassic succession eastward in the study area. The succession displays thinning over the Samson Dome, indicating halokinetic activity during deposition. Abbreviation: FC=Fault Complex.

In the work of improving the current knowledge about the Middle to Upper Jurassic succession in the Barents Sea, the succession has been divided into transgressive-regressive sequences (Koevoets et al., 2018; Marín, personal communication, October 15, 2018). The correlation of the sequences across the southwestern Barents Sea made it clear that Sequence 2 and 3, correlating to the lower Alge Member of the Hekkingen Formation, shows large variability in the gamma-ray signature (Fig. 4). Identification of maximum flooding surfaces (MFSs) in the sequences was based on stacking patterns, where there is a change from retrogradational to progradational pattern and they are marked by high gamma-ray values creating spikes in the gamma-ray log (Catuneanu et al., 2011). However, the spikes representing the MFS in Sequence 2 (MFS2) and Sequence 3 (MFS3) display an uncommon stratigraphic and regional variation in the southwestern Barents Sea (Fig. 4). The wells west of Loppa High and northward display an overall low gamma-ray signature in the logs and have no prominent spikes to mark the MFSs. In the southernmost and the northernmost part of the study area, there is a prominent spike representing MFS2, but low gamma-ray values for MFS3. Moving eastward, the prominent spike is present for MFS3 only or in both the MFSs.

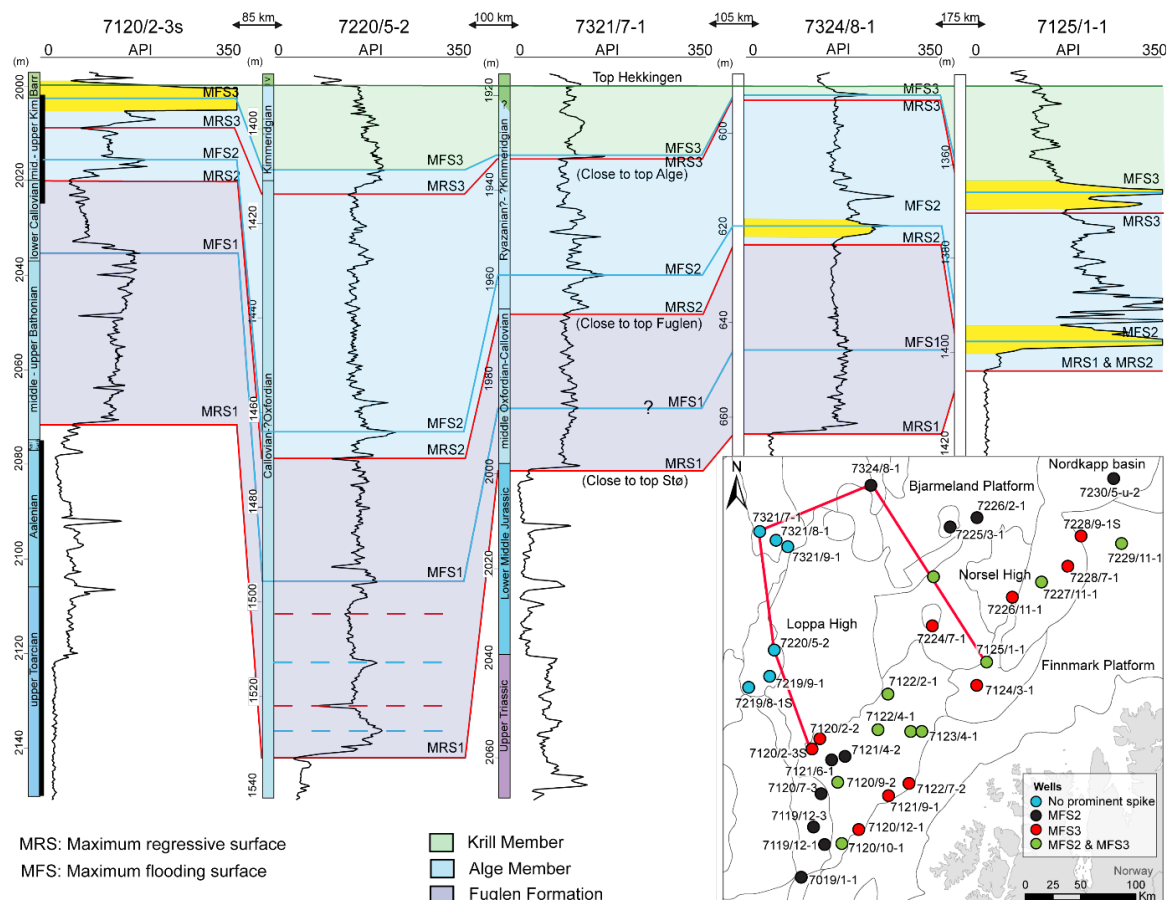


**Fig. 4** Well correlation with sequences adapted from Koevoets et al. (2018) and map displaying the spike distribution in the southwestern Barents Sea provided by Marín (personal communication, October 15, 2018). The prominent gamma-ray spikes are marked with a yellow colour in the well correlation in the Alge Member (blue). The map displays the location of the well correlation (red line).

## 1.1 Motivation & Objectives

The gamma-ray signature normally is assumed to be high for fine-grained material and low for coarse-grained. This is a simplification of reality as clay minerals, organic matter, feldspar and feldspar-rich lithoclasts all contain radioactive elements and can cause higher gamma-ray values than the lithology implies (Russell, 1941; Swanson, 1960; Rider, 1990). In the Alge Member, the lithology is reported to be homogenous black shale, regardless of the gamma-ray signatures and of the presence of prominent high-value spikes. Therefore, the aim of this study is to investigate if the prominent spikes in the gamma-ray log can be the result of compositional variations, (i.e. type of clay minerals, mineral composition) or variations in the organic matter content, and if these variations potentially can reflect differences in depositional environments, provenance areas, or reflect other changes in the Hekkingen Formation. As the Hekkingen Formation is an extensive and important source rock and hydrocarbon seal (Gabrielsen & Kløvjan, 1997; Ohm et al., 2008), increased knowledge of the lateral variability in composition and raised knowledge of the paleogeography are vital for further exploration in the Barents Sea.

Summarized main objectives for the thesis are to:

- Investigate the origin(s) of the prominent gamma-ray spike observed appearing at different flooding surfaces in the Alge Member of Hekkingen Formation,
- Combine the results from different scale data (seismic, 17 wells and samples of cores and cuttings) to develop an improved understanding of the lateral changes within the Alge Member and explain the changes with the depositional environment and paleogeography and,
- Study how the compositional variation affects the source rock quality of the Alge Member.

## 2. GEOLOGICAL SETTING

The Barents Sea is located at the northwestern corner of the Eurasian continental shelf in an intracratonic setting between Svalbard and the Norwegian mainland (Fig. 1; Fig. 5; Gabrielsen et al., 1990; Faleide et al., 1993). The Barents Sea is subdivided into numerous platforms, deep basins and structural highs (Gabrielsen et al., 1990; Faleide et al., 1993; Henriksen et al., 2011b). The eastern side of the Barents Sea is dominated by major basins, whereas in the westward direction the structures shift into widespread platforms and minor basins (Henriksen et al., 2011b). The structural configuration of the area is mainly caused by;

- two Pre-Mesozoic compressional events,
- three extensional events (late Paleozoic-Cenozoic) and,
- periodic uplift (late Mesozoic-Cenozoic).

The Caledonian Orogeny took place from Middle Ordovician to Early Devonian time, and represents the continent collision and consolidation of the Laurentian and the Baltic plate into the Laurasian continent, and thus the closing of the Iapetus Ocean (Doré, 1995; Smelror et al., 2009; Henriksen et al., 2011b). The Uralian orogeny was initiated during early Carboniferous time, but the orogenic phase started first during the late Permian, as the Laurentian plate started a further collision with Western Siberia (Fig. 5). The orogeny culminated during the Triassic, and lead to the formation and closure of a marginal basin in Novaya Zemlya (Gudlaugsson et al., 1998; Petrov et al., 2008; Smelror et al., 2009). This event seems to have affected only the eastern Barents Sea, whereas in the western part regional extension dominated (Smelror et al., 2009). The structural trends from the orogenies, the Caledonian in particular, dominate the basement substructure in the Barents Sea, causing N–S and NE–SW structural trends in the area (Doré, 1995; Gudlaugsson et al., 1998). Late Palaeozoic crustal extension can be connected to the northeast Atlantic rift between Greenland and Norway (Gudlaugsson et al., 1998). The rifting resulted in NE–SW trending horst and graben geometries (block faulting) in the southwestern Barents Sea, following the established lineaments in the Caledonian basement (Gabrielsen et al., 1990; Gudlaugsson et al., 1998).

The Barents Sea region experienced a relative tectonically quiescent period during the early Mesozoic before the tectonic activity increased during the Jurassic (Doré, 1995; Glørstad-Clark et al., 2010). During the late Middle Jurassic-Early Cretaceous, the tectonic activity comprised

of widespread rifting, resulting in a regional rift basin extending from the Rockall Trough west of Ireland to the Barents Sea (Fig. 5; Fig. 6; Faleide et al., 1993). Strike-slip fault movement along the basement lineaments, established rift basins in the southwestern Barents Sea (e.g. Bjørnøya, Trømsø and Harstad basins; Faleide et al., 1993). Several fault complexes show signs of tectonic activity from Middle Jurassic-Early Cretaceous; the Bjørnøyrenna Fault Complex, Ringvassøy-Loppa Fault Complex, Asterias Fault Complex and Hoop Fault Complex (HFC) all have recorded movement (Gabrielsen et al., 1990; Blauch et al., 2017; Indrevaer et al., 2017; Braut, 2018; Kairanov et al., 2019). The Middle Jurassic marked the reactivation of diachronous block faulting, which continued into the Cretaceous (Gabrielsen et al., 1990; Marín et al., 2018). The block-faulted Polhem Subplatform lacks the Jurassic sedimentary record and shows signs of active listric faulting from Late Jurassic-Early Cretaceous. The Loppa High, which is bounded by the Bjørnøyrenna Fault Complex and the Ringvassøy-Loppa Fault Complex in the west and the Asterias Fault Complex in the south, was uplifted due to the reactivation of the fault complexes (Gabrielsen et al., 1990). Moreover, the tectonic episodes triggered halokinetic movement, and the Svalis Dome, Samson Dome and the salt within the subsiding Nordkapp Basin experienced growth (Gabrielsen et al., 1990; Rojo & Escalona, 2018). For the southwestern Barents Sea, the rifting caused subsidence and combined with a regional transgression at the onset of Late Jurassic caused a widespread deposition of marine black shale. Anoxic conditions were established due to local submarine barriers (Worsley, 2008; Smelror et al., 2009).

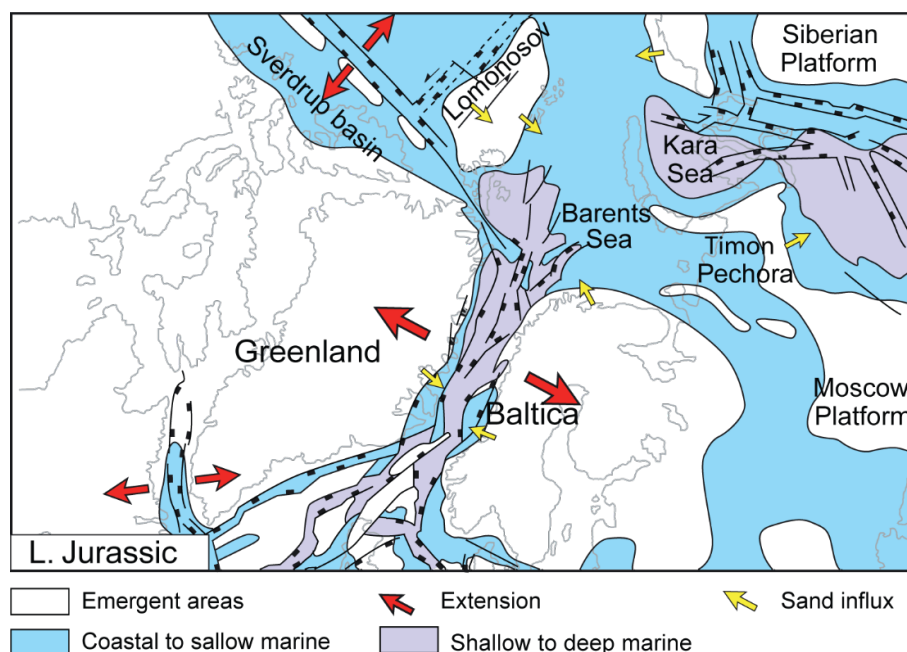


**Fig. 5** The geodynamic evolution of the Barents Sea region during the Late Jurassic. Modified by Smelror et al. (2009) after Ziegler (1988).

There are indications of both subsidence and inversion during the Early Cretaceous in the southwestern Barents Sea (Berglund et al., 1986; Gabrielsen et al., 1990; Indrevaer et al., 2017). The northernmost part of the Barents Sea, Svalbard and Franz Josef Land experienced uplift (Grantz et al., 2011). The uplift was related to the opening of the Amerasia Basin, which was accompanied by extensive magmatism and increased heat flow (Worsley, 2008). The Cenozoic uplift and erosion have been estimated to variate from zero to over 3000 m in the western Barents Sea, and it occurred in episodes (Fig. 7; Doré, 1991; Henriksen et al., 2011a). The main phases of subsequent Cenozoic uplift and erosion took place during Paleocene to Eocene, Oligocene and Pliocene to Pleistocene times, whereas the latest two was the most significant (Ohm et al., 2008). In the southwestern Barents Sea, the Stappen High, the Bjarmeland Platform, the Loppa High and the northern part of the Nordkapp Basin experienced the most uplift (Fig. 7).

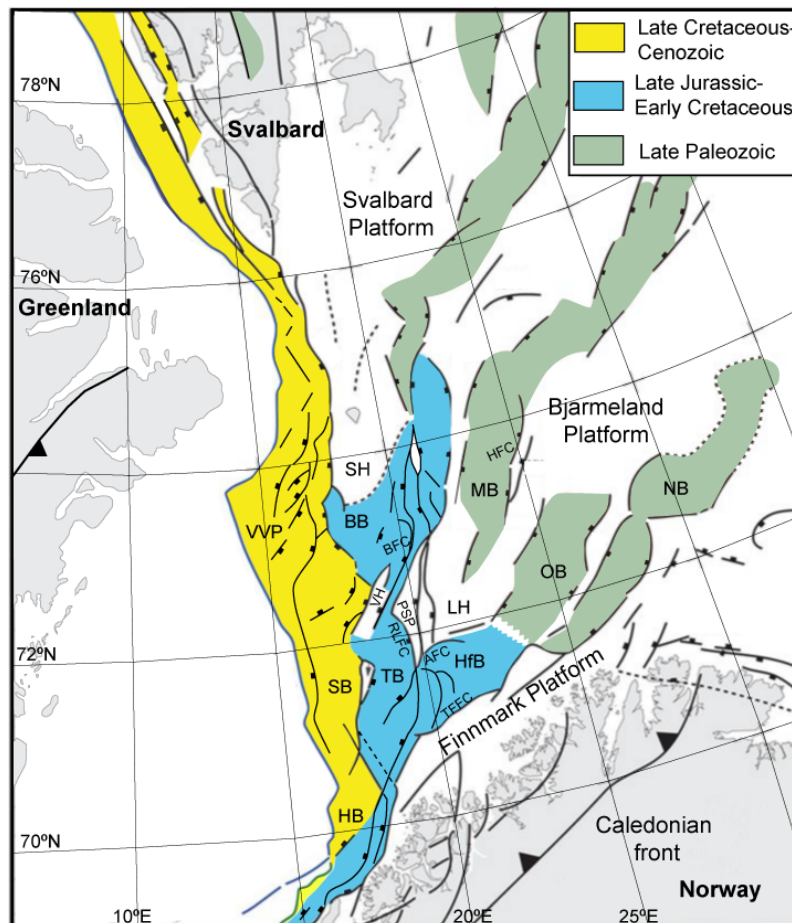


**Fig. 6** Map after Faleide et al. (2015) showing the main structural elements and the main periods of rifting and basin formation in the southwestern Barents Sea. Abbreviations: AFC=Asterias Fault Complex, BB=Bjørnøya Basin, BFC=Bjørnøya Fault Complex, HB= Harstad Basin, HFC=Hoop Fault Complex, HfB=Hammerfest Basin, LH=Loppa High, MB=Maud Basin, NB=Nordkapp Basin, OB=Ottar Basin, PSP=Polhem Subplatform, RLFC=Ringvassøy-Loppa Fault Complex, SB=Sørvestnaget Basin, SH=Stappen High, TB=Tromsø Basin, TFFC=Tromsø-Finnmark Fault Complex, VH=Veslemøy High, VVP=Vestbakken Volcanic Province.

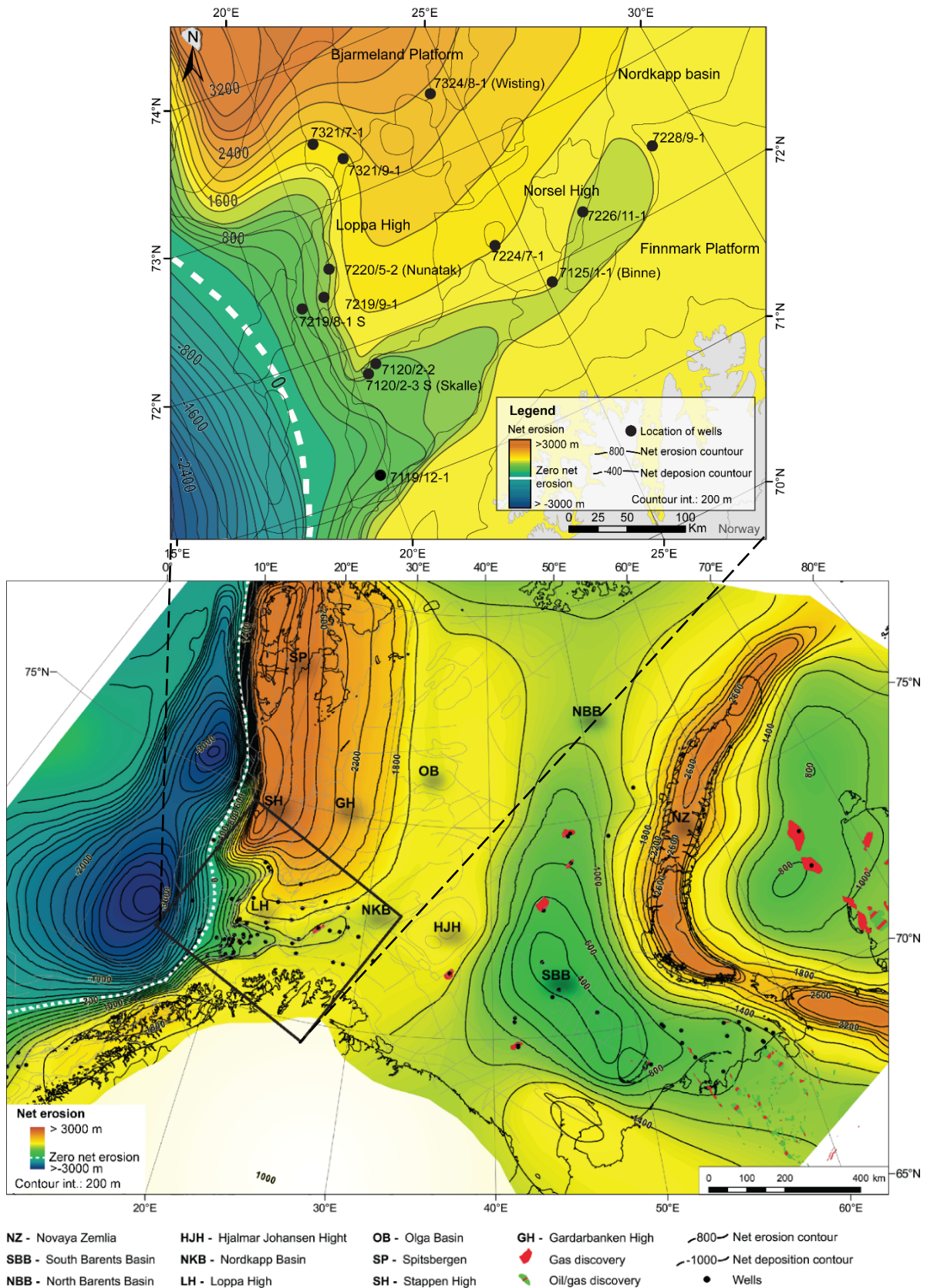


**Fig. 7 Bottom:** Map from Henriksen (2011a) showing the estimated net erosion for the Barents Sea region, variation from zero to more than 3000 m. The westernmost areas show no record of erosion, only subsidence. Top: Zoom in on the study area (marked with square on the map). The southwestern part of the area has experienced the lower amount of erosion, compared to the rest of the study area is interpreted to have experience between 1000 and 2000 m of uplift. The interpretation by Henriksen (2011a) displays an increase in erosion toward the north and Stappen High.

## 2.1 Stratigraphy

The Middle-Upper Jurassic succession in the southwestern Barents Sea includes grey, silty, bioturbated shale of the Fuglen Formation and the organic-rich shale of the Hekkingen Formation (Bugge et al., 2002). These two formations comprise the lowermost part of the Adventsdalen group (Fig. 8; Mørk et al., 1999).

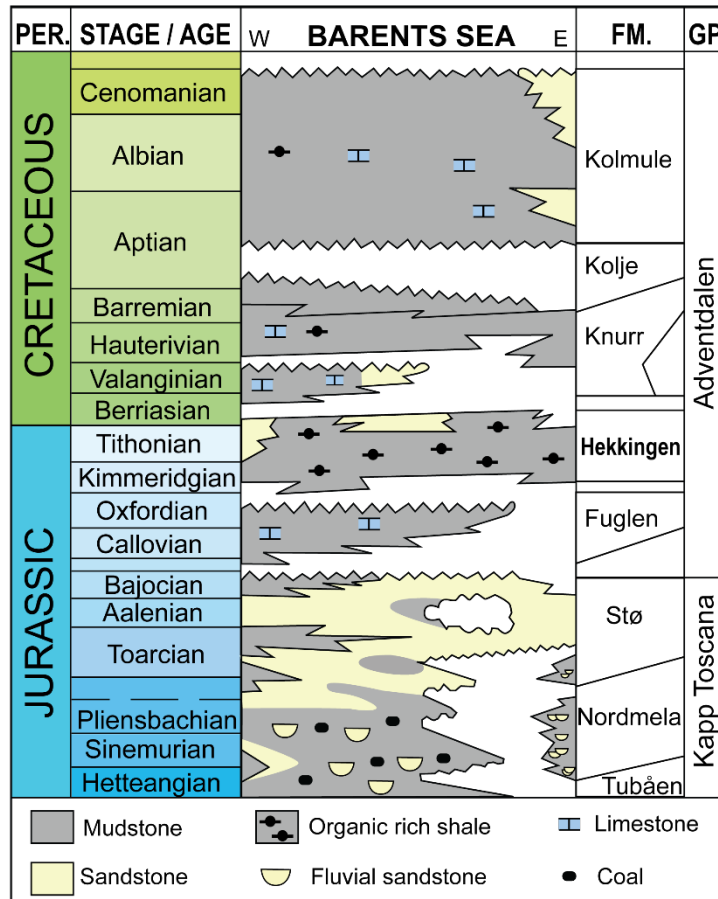


*Fig. 8 Chrono- and lithostratigraphic chart for the main Jurassic and Cretaceous succession in the southwestern Barents Sea. Modified from Nøttvedt et al. (1993).*

### THE HEKKINGEN FORMATION

The Hekkingen Formation was deposited in a deep shelf environment with anoxic to dysaerobic conditions based on organic matter content, kerogen type II and III, and an absence of oceanic current activity (Mørk et al., 1999; Smelror et al., 2001; Ohm et al., 2008). Low sedimentation rates and input of mostly fine-grained detritus in combination with a relatively high production of organic material in the water column, made excellent conditions for the preservation of organic material (Fig. 8). The deposition and preservation of the organic-rich sediments gave the formation excellent hydrocarbon-generating potential (Georgiev et al., 2017). Base and top of the Hekkingen Formation are marked by unconformities, and the thickness of the formation is variable (Bugge et al., 2002). The formation does not exceed a thickness of 100 m in the

greater part of the Barents Sea and thins toward the east (Leith et al., 1993). However, in the Bjørnøya Sør area in the westernmost part of the Barents Sea (well 7219/8-1S) the Hekkingen Formation exhibited a thickness of 856 m (Fig. 9). The formation is separated into two members, Alge and Krill, based on the gamma-ray intensity (Fig. 9; NPD, 2019).

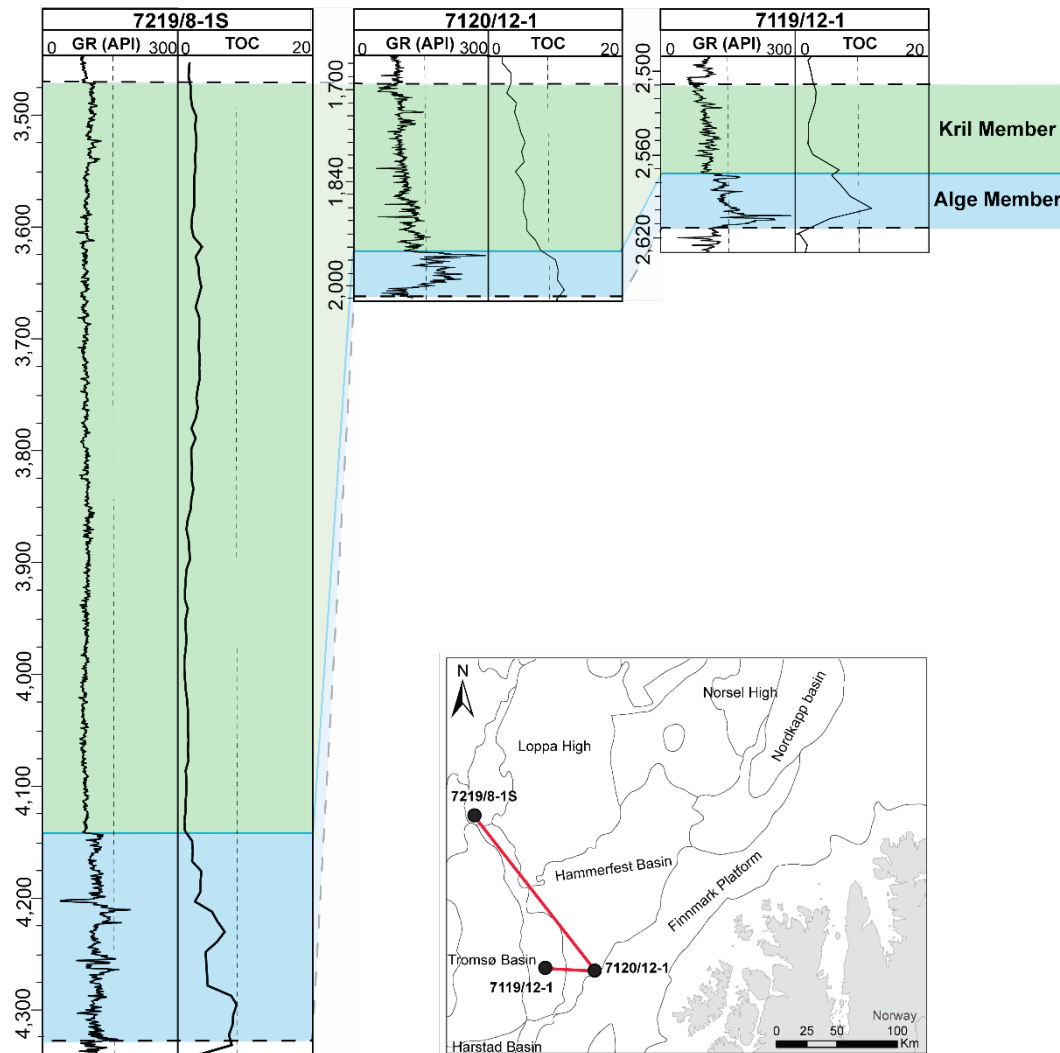


**Fig. 9** Gamma-ray logs (GR) and total organic carbon (TOC) content of the Hekkingen Formation with the members marked with blue (Alge) and green (Krill). Notice the difference in gamma-ray values and TOC-values for the two members. 7219/8-1S contain the thickest recorded succession of the Hekkingen Formation; 856 m. Well 7120/12-1 is the type well for the Hekkingen Formation while 7119/12-1 is the reference well. The vertical scale of the wells are in meters.

### The Alge Member

The lower Alge Member (late Oxfordian to Kimmeridgian), is dominated by organic-rich, black paper shale which displays high gamma-ray signatures (Fig. 9; Fig. 10; Mørk et al., 1999; Bugge et al., 2002), and a high total organic carbon content of 6-16 wt. % (Fig. 9; Smelror et al., 2001). A transition from pyritic and carbonate-cemented mudstone to poorly consolidated shale defines the base of the member (NPD, 2019).

## The Krill Member

The upper Krill Member (Kimmeridgian to Berriasian) has significantly lower gamma-ray readings and is therefore easily distinguished from the Alge Member (Fig. 9; Smelror et al., 2001). The low gamma-ray readings have been interpreted to be due to a lower content of organic matter (Bugge et al., 2002). The presence of clastic wedges within this member (Fig. 10; Braut, 2018), shows that the deposition was affected by the initiation of the Late Jurassic to Early Cretaceous rift event in the southwestern Barents Sea, and its diachronous faults (Marín et al., 2018). The member contains mudstone, limestone, shale, siltstone and sandstone (Mørk et al., 1999).

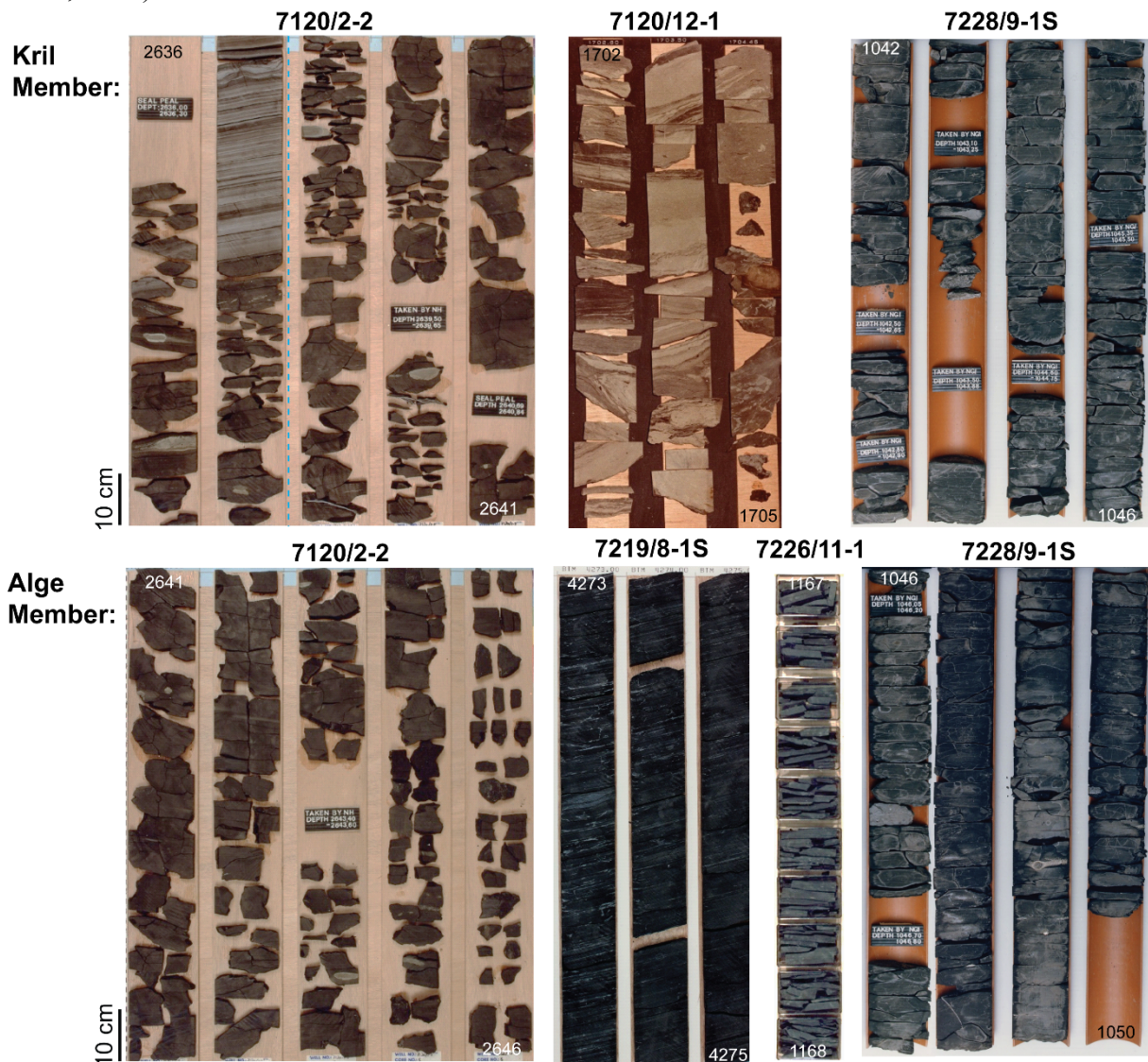


**Fig. 10** Cores from the Krill (top row) and Alge (bottom row) members show the differences in lithology between the two members and within the members. The sand rich successions of the Krill Member have been interpreted as clastic wedges (Braut 2018). The black shale of the Alge Member displays some variations in colour, texture (massive vs. brittle) and sedimentary structures (visible lamination in 7219/8-1S). A blue dashed line in the top left picture represent the transition between the Krill and the Alge members in well 7120/2-2.

### **3. DATA & METHODOLOGY**

#### **3.1 Data**

Seventeen wells in the southwestern Barents Sea represent the basis for this study (Table 1). The wells were chosen based on their location in the southwestern Barents Sea in order to investigate lateral and vertical variations in the Hekkingen Formation (Fig. 11). Five cores from the Hekkingen Formation were logged; two of the cores (7219/8-1S and 7228/9-1S) were analysed at the Norwegian Petroleum Directorate (NPD) in Stavanger, whereas the remaining cores (7120/2-2, 7120/2-3S (Skalle), and 7125/1-1 (Binne)) were studied at Weatherford Core Storage in Sandnes. The core from well 7228/9-1S was not sampled, but eleven samples were collected from the other four cores (Table 1). In addition, twenty samples of cuttings were collected from eight of the wells, 7119/12-2, 7120/2-2, 7125/1-1, 7220/5-2 (Nunatak), 7224/7-1, 7321/7-1, 7321/9-1 and 7324/8-1 (Wisting), giving a total of 31 samples (Table 1). The Norwegian DISKOS database provided 2D and 3D seismic reflection data in the area (Fig. 11). The dataset also comprises seismic data of variable quality, and with frequencies in the range of 15–45 Hz, which results in a seismic resolution in the range of 17–50 m in the Hekkingen Formation. The database contains full suites of wells and well logs for the study area (Table 1). In addition, the JuLoCra-consortium has provided geochemical data for wells 7219/9-1, 7226/11-1 and 7228/9-1S, and data for the other well where geochemical data had been collected prior to this thesis.

Additional TOC-data for the wells were collected from the geochemical reports accessed on the webpages of NPD (NPD, 2019). Age-data for 12 of the wells (excluding 7120/6-3S (Juksa), 7121/9-1 (Zapffe), 7123/4-1A (Tornerose), 7220/10-1 (Salina) and 7324/8-1 (Wisting)), were found in the completion reports for the wells on NPD webpages (NPD, 2019).

**Table 1** Overview of wells, samples and performed analyses. Abbreviations: Son=sonic, Den=density, GR=gamma-ray, SGR=spectral gamma-ray, TOC=TOC-data from (NPD, 2019), Mac=maceral analysis. Data provided by JuLoCra are marked with \*.

Well	Sampled depths (m)	Sample type	Available well logs & data	Performed analyses
7119/12-1	2586 2595 2508	cuttings	Son, Den, GR, TOC	XRD, Rock-Eval, Mac
7120/2-2	2640	core	Son, Den, GR, TOC	XRD, Rock-Eval, Mac
	2635	cuttings		XRD, Rock-Eval, Mac
7120/2-3S	2003.75 2005.45 2009.15 2014.95 2015.97	core	Son, Den, GR, SGR	XRD, Rock-Eval, Mac
7120/6-3S			GR, SGR	
7121/9-1			GR, SGR	
7123/4-1A			GR, SGR	
7125/1-1	1366	core	Son, Den, GR, TOC	XRD, Rock-Eval, Mac
	1380 1398	cuttings		
7219/8-1S	4271.10 4272.45 4275.27 4275.74	core	Son, Den, GR, TOC	XRD, Rock-Eval, Mac
7219/9-1*	1901.5* 1917*		Son, Den, GR, TOC	Rock-Eval
7220/5-2	1408 1465	cuttings	Son, Den, GR, SGR	XRD, Rock-Eval, Mac
7220/10-1			GR, SGR	
7224/7-1	836 848	cuttings	Son, Den, GR, TOC	XRD, Rock-Eval
7226/11-1*	1167* 1176* 1180*		Son, Den, GR, TOC	Rock-Eval
7228/9-1S*	1045* 1055* 1065*		Son, Den, GR, TOC	Rock-Eval
7321/7-1	1924 1933 1939 1951 1963	cuttings	Son, Den, GR, TOC	XRD, Rock-Eval, Mac
7321/9-1	1350 1360	cuttings	Den, GR, TOC	XRD, Rock-Eval, Mac
7324/8-1	600 610 620	cuttings	Son, Den, GR, TOC	XRD, Rock-Eval, Mac

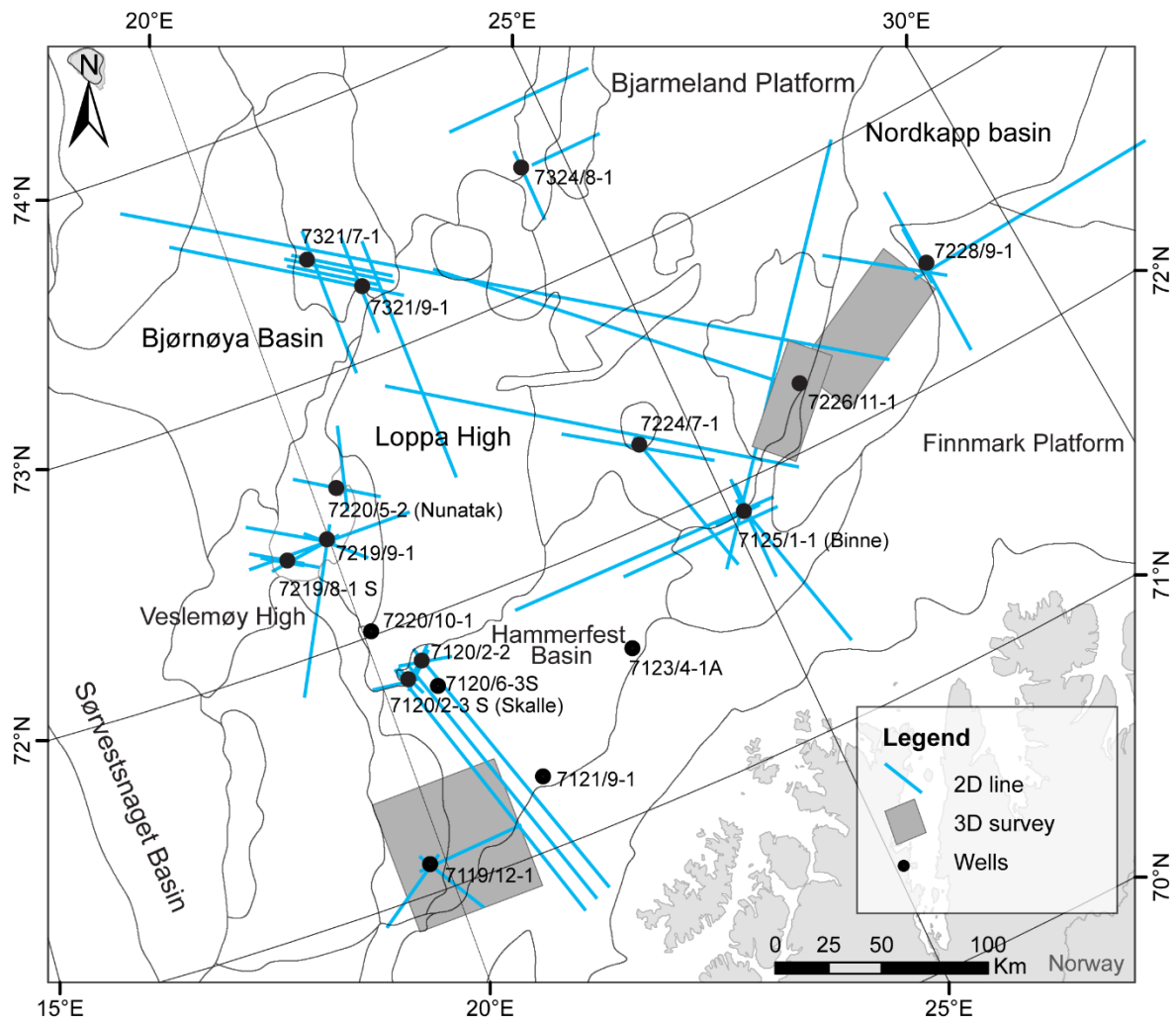


**Fig. 11** Overview of the utilized seismic lines and surveys in the study. The blue lines represent 2D-lines and the grey squares represent 3D surveys.

## 3.2 Methodology

### 3.2.1 X-RAY DIFFRACTION

All 31 samples were analysed using X-ray Diffraction (XRD). Sample preparation, measurements and data evaluation were performed at Friedrich-Schiller Universität Jena, Germany.

#### Sample preparation

The samples were gently crushed in a mortar, as grinding the sample would destroy the clay mineral structures. For hard samples, distilled water was added to the mortar and the sample was gently grinded. The water will cause the clay minerals to float and therefore avoid damage. Room-tempered de-ionized water was added to the crushed sample and the mix was stirred for 15 minutes. The clay mixture was then placed in an Atterberg cylinder, and 10-15 mg of  $\text{Na}_4\text{P}_2\text{O}_7$  solution was added to prevent the sample from clogging. The large surface-to-volume

ratio of the flaky minerals will cause them (and other phyllosilicates, e.g. mica minerals) to be held longer in suspension, thus making it possible to extract them from the sample solution. When the denser minerals have sunken below the tap, the liquid containing the clay minerals were separated from the rest of the sample. The samples were stirred and left for another ~20 hours before the clay fraction was extracted again. The extraction was done three times as a qualitative approach to extract the clay minerals.

The liquid left in the clay-fraction was removed by centrifuging the samples. A pipette was used to extract some of the sample, which was dried in a heating cabinet (>40 °C) and weighted in order to determine the density of each sample solution. Then, the sample solution was placed on a corundum ceramic tile, and a water vacuum pump removed the remaining liquid through the porous sample holder. In this case, 62 mg of sample was used to cover the 4.15 cm<sup>2</sup> ceramic tile. As the pump rapidly removed the liquid, the clay minerals will orient themselves parallel to the ceramic tile. The prepared sample was air dried at room temperature.

After the XRD-analysis of the air-dried samples, the samples spent 24 hours in a desiccator with ethylene glycol at room temperature for the clay minerals to be saturated. After XRD analysis of the saturated samples, the samples were heated to 600 °C for 1 hour. In addition, the furnace used 20 minutes to reach this temperature and 45 minutes to cool down.

## **Analysis**

The prepared samples were analysed in a BRUKER D8 Advance X-ray diffractor, with copper radiation. The data were processed using the software DIFFRAC.EVA version 5, with access to the database PDF-4+ 2019 RDB. The clay minerals, and the other minerals still present in the clay fraction, were identified by their characteristic reflection patterns, and the three different patterns (air-dried, glycol-saturated and heated) increases the chances of correct mineral identification. The samples were scanned with a step speed of 0.020354842 °2θ/s.

### ***Air-dried***

Air-dried samples were analysed for a range of 2–70 °2θ.

### ***Glycol-saturated***

Ethylene glycol-saturated samples were analysed for 2–30 °2θ. Each sample was analysed individually in the machine, as the ethylene glycol begins to evaporate from the sample when

removed from the desiccator. The glycol will saturate the sample and expand the basal spacing in the clay minerals, allowing a more reliable identification of minerals e.g. when overlapping peaks occur.

### ***Heated***

The heating of the samples will collapse the crystal structure of smectite to a lower value peak. The high temperature will also destroy kaolinite and certain chlorites. This will help to distinguish the individual clay minerals. The samples were analysed for 2–30 °2θ.

### **Identification**

Several peaks in the resulting graphs represent each clay mineral; the clay minerals are layered and when the X-ray hits them, they will give a response (peak) for each layer. In order to refer to a peak, 001 represent the first peak (or layer) of a mineral, 002 the second etc. The clay minerals are identified by the location of the peaks after each analysis (Hardy & Tucker, 1988).

## **3.2.2 GEOCHEMICAL ANALYSES**

Applied Geochemical Technology (APT) in Oslo handled the sample preparation and performed Rock-Eval pyrolysis and TOC measurements on samples from 13 of the wells (Table 1). The workflow at APT follows the guidelines suggested by Weiss et al. (2000). A standard test is analysed for every tenth sample in order to quality-check the results.

### **Rock-Eval pyrolysis**

#### ***Sample preparation***

The samples were crushed to powder in a mortar. The samples were weighted in metal containers, along with two samples of the standard test. For samples that were expected to be organic-rich, 10 mg material was enough, whereas 80 mg was used for less organic-rich material.

#### ***Analysis***

A Rock-Eval 6 instrument was used for the analysis, and the samples were placed onto a rotational wheel in the instrument. Each sample was placed in an oxygen-free chamber. The chambers were then heated rapidly in order to fracture the hydrocarbon chain structures and create bitumen. The increase in temperature started at 300 °C for 3 minutes before the temperature was further increased with 25 °C per minute until the chamber temperature was 650 °C. During the heating of the sample, a flame ionization detector records the volume of

hydrocarbons the potential source rock generated. In addition, a second detector recorded the amount of CO<sub>2</sub> and CO generated during the process. The temperature of maximum hydrocarbon production (Tmax) was also registered.

## **TOC**

### ***Sample preparation***

The samples were crushed to powder in a mortar, and diluted HCl was added to remove carbonate from the samples.

### ***Analysis***

The samples were heated to 1350 °C in a Leco SC-623 combustion oven. The amount of carbon in the sample was measured as carbon dioxide by an infrared detector.

The additional TOC measurements from NPD (2019), were collected for the entire Hekkingen Formation from the geochemical rapports for each well accessed on the webpage of NPD (Table 1, NPD 2019). The TOC data collected on NPD's webpage were sometimes stated for a specific depth and some time given for an interval. To better display the variation in the TOC and compare to the well logs, the shallowest depths were consequently chosen to plot interval values.

### **3.2.3 MACERAL ANALYSIS**

Thomas Demchuk, RPS Group Inc., USA, performed the sample preparation and the maceral and mineral analysis.

### ***Sample preparation***

The samples were crushed until the material could pass through a 1.2 mm. The material was then embedded in thermoplastic epoxy, put in 3.2 cm moulds and left overnight to harden. The resulting pellets were then grinded and polished according to the ASTM standards (ASTM D7708 - 11, 2011).

### ***Analysis***

The samples were analysed using a Zeiss Axio-Scope A1 at 500x magnification (50x objective combined with a 10x ocular) in immersion oil. White- and ultraviolet-light was used to point count and identify a total of 300 grains of organic matter and minerals for each sample. The organic matter in the samples, the macerals, were further identified based on the origin of the organic matter.

### 3.2.4 SEISMIC DATA & WELL LOGS

The seismic interpretation (and generation of synthetic seismogram) was performed in DecisionSpace software provided by Landmark Halliburton. Synthetic seismograms were generated for wells 7219/8-1S and 7220/5-2 (Fig. 12). Check-shots were available for both wells and were used to establish the time-depth relationship between the seismic data and the wells. The synthetic seismograms were generated from the sonic and density logs, and a Butterworth-wavelet was applied (Fig. 12). The best fit was accomplished with manual adjustments of the wavelet; the wavelets were time-shifted (-28.4 ms) and phase rotated (-157°) for the best fit. The seismic data used in this study had normal polarity. The focus for the seismic interpretation was the identification and comparison of seismic facies around the studied wells to identify possible differences in depositional systems for the source rock.

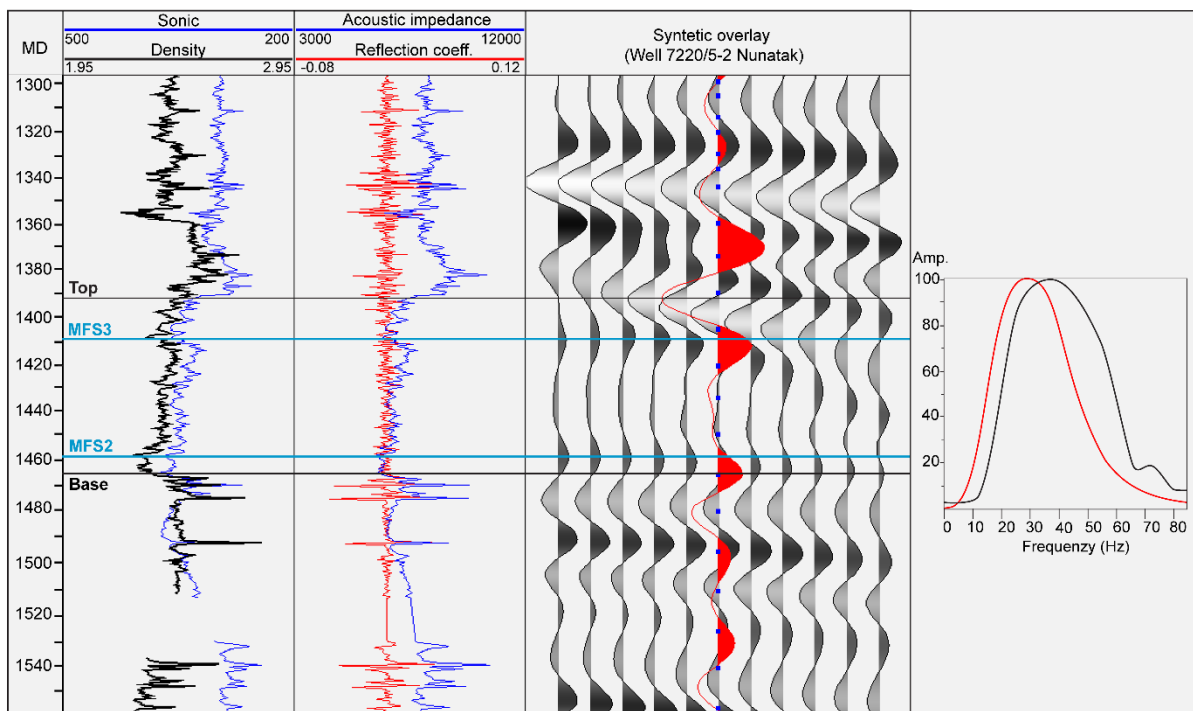


**Fig. 12** Synthetic seismogram of well 7220/5-2 (Nunatak). Top and base of the Hekkingen Formation and the two MFS's of interest are marked. The wavelets are the Butterworth wavelet used for the synthetic seismogram (red), and an extracted wavelet from the Hekkingen Formation (black). The extracted wavelet peak at 37 Hz, but show a frequency-range of 25-45Hz.

Sonic, density, gamma-ray and spectral gamma-ray logs were viewed and compared to the seismic and TOC measurements to better understand the variation within the Hekkingen Formation, particular the Alge Member. In addition, the thickness and age of the Alge Member were used to calculate the sedimentation rate. The calculations are only based on these to variables and do therefore not account for neither erosion of the member, nor compaction due to burial. The sedimentation rate was also used to calculate the approximate time it would take a prominent high-value gamma-ray spike to be deposited.

### 3.2.5 CORE LOGS

#### Core viewing

Cores were described with focus on textural and compositional features, sedimentary structures and bioturbation in order to interpret the lateral and vertical variation in the depositional environment. Five cores of the Hekkingen Formation were viewed and described, total length adding up to 40 m (Table 2). Braut (2018) formerly viewed cores of wells 7120/2-2 and 7120/2-3S, and her description was merged with additional observations as the viewed material represents different cuts of the cores. The core data logged of the Hekkingen Formation represent only parts of the formation and in some cases, intervals were missing in the core. This provides uncertainty to the interpretation of the facies observed in the cores.

**Table 2** Depth of the logged core intervals and the length of the intervals in each well.

<i>Well</i>	<i>Depth (m)</i>	<i>Length (m)</i>
7120/2-2	2636–2646	9.6
7120/2-3 S	2002–2018.5	18.5
7125/1-1	1360–1371	10.7
7219/8-1	4270–4277	7.5
7228/9-1S	1042–1050	7.8

#### Core sampling

In order to select the samples, the gamma-ray patterns for each well were analysed, and the MFS's were targeted (Table 3). In addition, areas with low gamma-ray readings were sampled in order to compare and find the potential compositional variations causing low or prominently high gamma-ray values. As few of the wells in the dataset had cores in the Alge Member, cuttings were sampled in order to determine the composition. The drilling operators have collected the cuttings at varying intervals, ranging from 3–10 m, and they may be contaminated by other formations through caving in the borehole. Therefore, a higher uncertainty is assumed for the results for these samples.

**Table 3** Overview of the sampled depths and depth of the MFSs in the Alge Member. The listed prominence of the spike is relative to the overall gamma-ray signature in the Alge Member. The stated depth for the MFS represents the depth where the peak displays the highest value in the gamma-ray log. The sampled depths marked in bold text represent a sampled depth that belongs to a MFS spike, although the centre of the spike is not always collected. All core samples are marked with a \*.

<i>Wells</i>	<i>Sampled depths (m)</i>	<i>Depths of MFSs</i>	<i>Spike prominence relative to the overall gamma-ray signature.</i>
7119/12-1	2586	MFS3: 2575.43	Low-value spike
	2595	MFS2: 2603.41	Prominent spike
	2608		
7120/2-2	2635	MFS3: 2640	Prominent spike
	<b>2640*</b>	MFS2: 2654	Prominent spike
7120/2-3S	<b>2003.75*</b>		
	2005.45*	MFS3: 2003	Prominent spike
	2009.15*	MFS2: 2015	Medium value spike
	<b>2014.95*</b>		
	2015.97*		
7125/1-1	<b>1366*</b>	MFS3: 1366.19	Prominent spike
	1380	MFS2: 1397.38	Prominent spike
	<b>1398</b>		
7219/8-1S	4271.10*		
	4272.45*	MFS3: 4144	Low-value spike
	4275.27*	MFS2: 4210	Low-value spike
	4275.74*		
7219/9-1	<b>1901.5</b>	MFS3: 1901.45	Low-value spike
	1917	MFS2: 1916.64	Low-value spike
7220/5-2	<b>1408</b>	MFS3: 1408.70	Low-value spike
	1465	MFS2: 1457.90	Low-value spike
7224/7-1	<b>836</b>	MFS3: 836.95	Prominent spike
	848	MFS2: 850.12	Medium- to high-value spike
7226/11-1	1167	MFS3: 1161.11	Prominent spike
	1176	MFS2: 1182.10	Medium- to high-value spike
	1180		
7228/9-1S	1045		
	<b>1055</b>	MFS2: 1054.6	Prominent spike
	1065		
7321/7-1	1924		
	<b>1933</b>	MFS3: 1932.96	Low-value spike
	1939	MFS2: 1958.24	Low-value spike
	1951		
	1963		
7321/9-1	1350	MFS3: 1347.5	Low-value spike
	1360	MFS2: 1365	Low-value spike
7324/8-1	600	MFS3:592	Low-value spike
	610	MFS2: 619	Low-value spike
	<b>620</b>		

### **3.2.6 PRINCIPAL COMPONENT ANALYSIS**

Principal component analysis (PCA) is a multivariate statistical method that can be applied to high-dimensional datasets (dataset consisting of  $n$  objects and  $p$  variables) to reduce the datasets to a lower dimensional space (2D or 3D) and still preserve most of the information (Johnson & Wichern, 2003; Abdi & Williams, 2010). The objectives of the analysis were to reduce the dataset and simplify the interpretation of the data. The PCA will create a few new variables, principal components, for the dataset by defining linear combinations of the original ones. The principal components (PC) are linearly uncorrelated and defines the variance in the dataset, whereas PC 1 describes most of the variance, PC 2 describes the second most etc. (Johnson & Wichern, 2003). The software Sirius version 11.0 was applied for the analysis, courtesy of Pattern Recognition Systems AS.

## 4. OBSERVATIONS & INTERPRETATION

### 4.1 X-ray Diffraction

#### Observations

XRD-analysis of the clay fraction (<2 µm) of the shale made it possible to identify the clay minerals illite (used as a collective term for illite and moscovite in the clay fraction), interlayered illite-smectite, chlorite and kaolinite in the Alge Member. All clay fractions contain quartz. Corundum from the ceramic sample holder was detected in some measurements. In addition, the clay fraction shows relatively high pyrite measurements in samples from two wells (Table 4).

**Table 4** Results from the XRD. The distribution of the clay minerals and pyrite. Samples in green are from the Krill Member, the samples in blue is from the Fuglen Formation.

Well	Depth (m)	Chlorite	Illite	Illite-smectite	Kaolinite	Pyrite
7119/12-1	2586	X		X	X	
7119/12-1	2595			X	X	
7119/12-1	2608	X		X	X	
7120/2-2	2635	X		X	X	
7120/2-2	2640			X	X	X
7120/2-3S	2003			X	X	X
7120/2-3S	2005			X	X	X
7120/2-3S	2009			X	X	X
7120/2-3S	2014			X	X	X
7120/2-3S	2016			X	X	
7125/1-1	1366			X	X	
7125/1-1	1380	X		X	X	
7125/1-1	1398			X	X	
7219/8-1S	4174.1		X			
7219/8-1S	4274.7		X			
7219/8-1S	4175.2		X			
7219/8-1S	4175.7		X			
7220/5-2	1408	X		X	X	
7220/5-2	1465	X		X	X	
7224/7-1	836	X		X	X	
7224/7-1	848			X	X	
7321/7-1	1924	X		X	X	
7321/7-1	1933	X		X	X	
7321/7-1	1939			X	X	
7321/7-1	1951	X		X	X	
7321/7-1	1963			X	X	
7321/9-1	1350	X		X	X	
7321/9-1	1360	X		X	X	
7324/8-1	600	X		X	X	
7324/8-1	610	X		X	X	
7324/8-1	620	X		X	X	

The saturation of samples with glycol ethylene caused the smectite in the interlayered illite-smectite to swell; therefore, one can observe a slight shift of the peak toward the left in the graph (Fig. 13). The structures of both smectite and kaolinite collapsed during the heating (Fig. 13). Some degree of interlayered illite-smectite was present in all samples except in the samples from well 7219/8-1S, which only contained illite (Table 4). In well 7120/2-3S, the interlayered illite-smectite display a transformation toward illite as the sampled depth turns shallower (Fig. 14). Chlorite is present throughout the study area, only being absent from the Alge Formation in the wells in the Hammerfest Basin and from 7219/8-1S (Table 4).

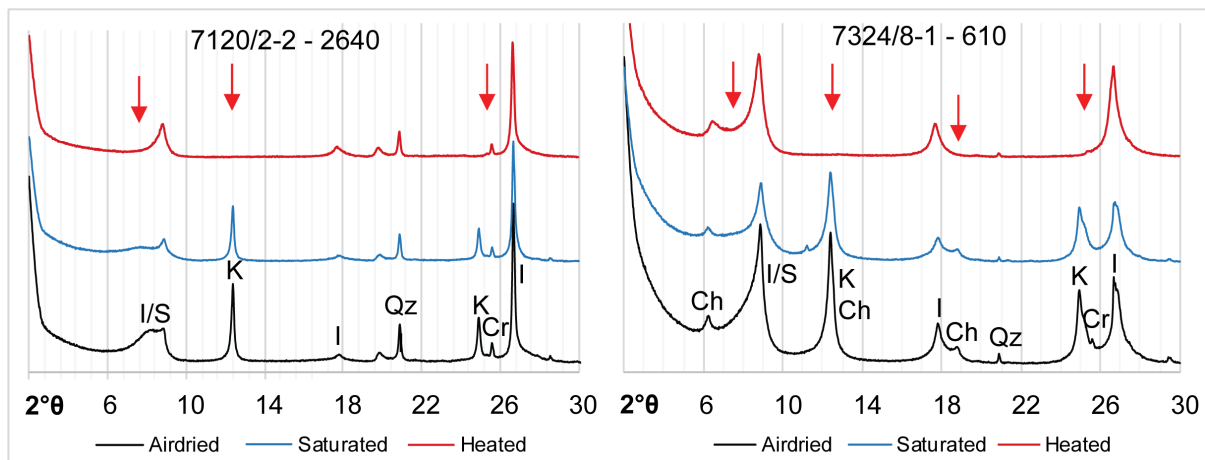


**Fig. 13** XRD-measurements to illustrate the position of the clay-mineral peaks and the changes due to saturation and heat treatment, marked with red arrows. Abbreviations: I/S=interlayered smectite-illite, K=kaolinite, I=illite, Qz=quartz, Cr=corundum.

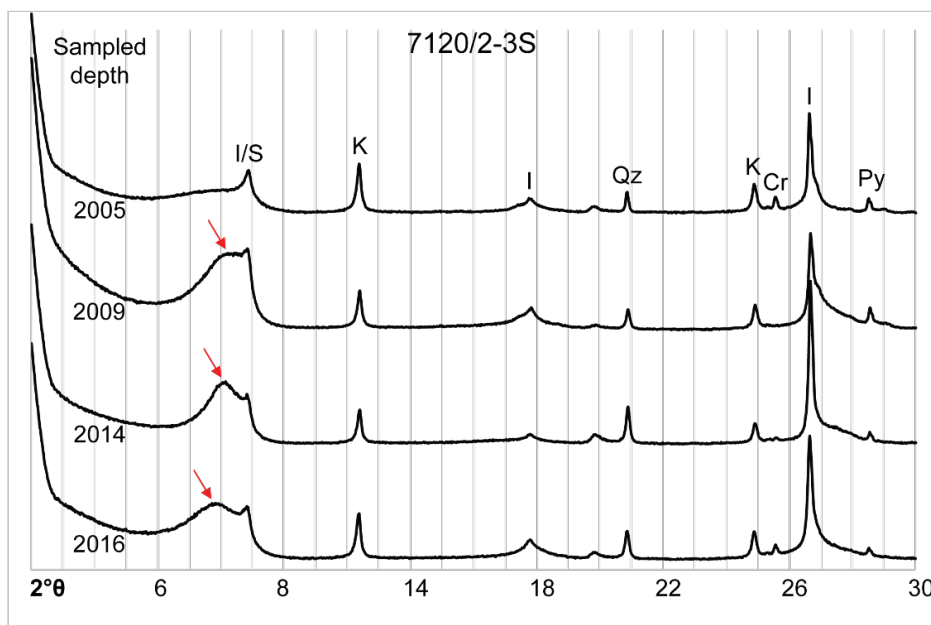


**Fig. 14** Transformation of interlayered illite-smectite to illite as the depths get shallower. The sampled depth in meters is marked to the left of each graph. All displayed measurements are from the airdried sample. Abbreviations: I/S=interlayered smectite-illite, K=kaolinite, I=illite, Qz=quartz, Cr=corundum, Py=pyrite.

Kaolinite and smectite were observed in all samples except in well 7219/8-1S. This well penetrates the deepest buried Hekkingen Formation in this study at almost 3500 m, the Alge Member below 4000 m in an uplifted area (Fig. 7). Thus, it has been buried deeper than its current position.

The PCA of the XRD-measurements identifies the 001 and 002 peaks of illite and kaolinite as the variables causing the greatest deviation in the dataset (Table 5). The PCA analysis divided the clay minerals in the Alge Member into three main groups; 1) illite, 2) chlorite, illite-smectite and kaolinite and 3) illite-smectite and kaolinite (Table 6; Fig. 15). Further division of group 2 and 3 into subgroups was based on the amount of counts of the different mineral, and the maturity of the smectite-illite transformation. The variation in the kaolinite count was used to separate the groups into subgroups. However, the samples with a high smectite count are separated from the others (subgroup 3c) regardless of the kaolinite (001) count (Table 6; Fig. 15). No correlation between the clay minerals and the gamma-ray values was observed when adding the gamma-ray values to the PCA.

**Table 5** The variables that correspond with the PCs, causing the greatest deviation in the data set. The variables with positive or negative value the furthest from zero correlate the strongest to the principal component.

Variable	PC 1 (39.88 %)	PC 2 (25.64 %)	PC 3 (14.01 %)
Illite (001) (8.7 2°θ)	-0.142	-0.0026	0.0348
Kaolinite (001) (12.4 2°θ)	0.132	-0.127	-0.107
Chlorite (002) (12.5 2°θ)	0.0495	-0.0988	-0.101
Kaolinite (002) (24.6 2°θ)	0.0876	-0.0263	0.0771
Illite (003) (26.6 2°θ)	0.105	0.224	0.158

**Table 6** Division of the samples into groups and subgroups based on mineral composition after the PCA.

Groups	Clay minerals	Subgroups	Distinction
1	Illite		
2	Chlorite Smectite-illite Kaolinite	2a	» High kaolinite count
		2b	» Low kaolinite count
3	Smectite-illite Kaolinite	3a	» Mature smectite-illite transformation » Low kaolinite count
		3b	» Immature smectite-illite transformation » High kaolinite count
		3c	» High smectite count

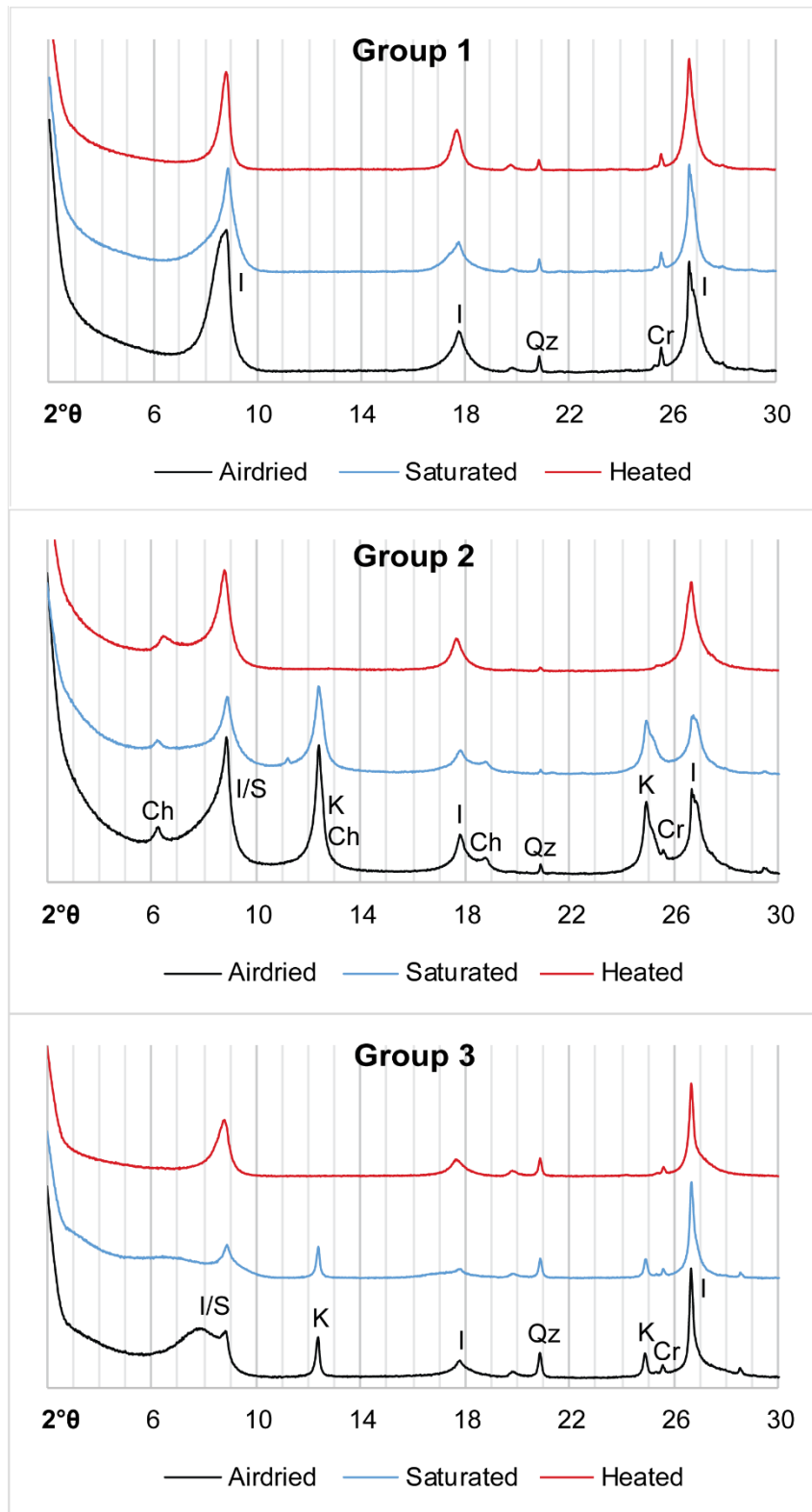


**Fig. 15** A representative graph for each of the main clay-composition groups. The graph for group 1 (7219/8-1-4275.27) only has the peaks representing illite (I). Group 2 (7324/8-1-600) displays the peaks for chlorite (Ch), interlayered illite-smectite (I/S) and kaolinite (K). Moreover, the graph for group 3 (7120/2-3S-2016) displays the peaks for interlayered illite-smectite and kaolinite. In this case, group 2 displays a high kaolinite count and belong in subgroup 2b, while group 3 displays a low kaolinite count and should be placed in 3a, but the high smectite peak (001) places the sample in 3c. Other abbreviations: Qz=quartz, Cr=corundum.

Group 1 only is represented by the samples from well 7219/8-1S, west of the Loppa High (Fig. 16). Group 2, containing chlorite, is present in the entire study area and occurs most frequently west–northwest of the Loppa High (Fig. 16). In the samples south and eastward in the study area, chlorite occurs more rarely, and the majority of the samples belongs to group 3. Within group 3, the interlayered smectite-illite could be separated by the maturity of the smectite-illite transformation (Table 6). In some samples, the smectite has nearly transformed to illite, but a minor reaction could still be observed to the glycol ethylene saturation and heating. The immature smectite-illite transformation was defined for samples where the peaks for smectite and illite were located further apart, whereas the last subgroup, 3c, is represented by the samples that had a clear smectite peak that is higher than the illite-peak (Fig. 14). For the wells where it was possible to sample the depth of the MFSs, the prominent high-value spike only occurs in group 3. However, lower-value spikes were also recorded within the same group as well as within group 2, and MFSs with low-value gamma-ray spikes could be found in group 2 (Fig. 16).

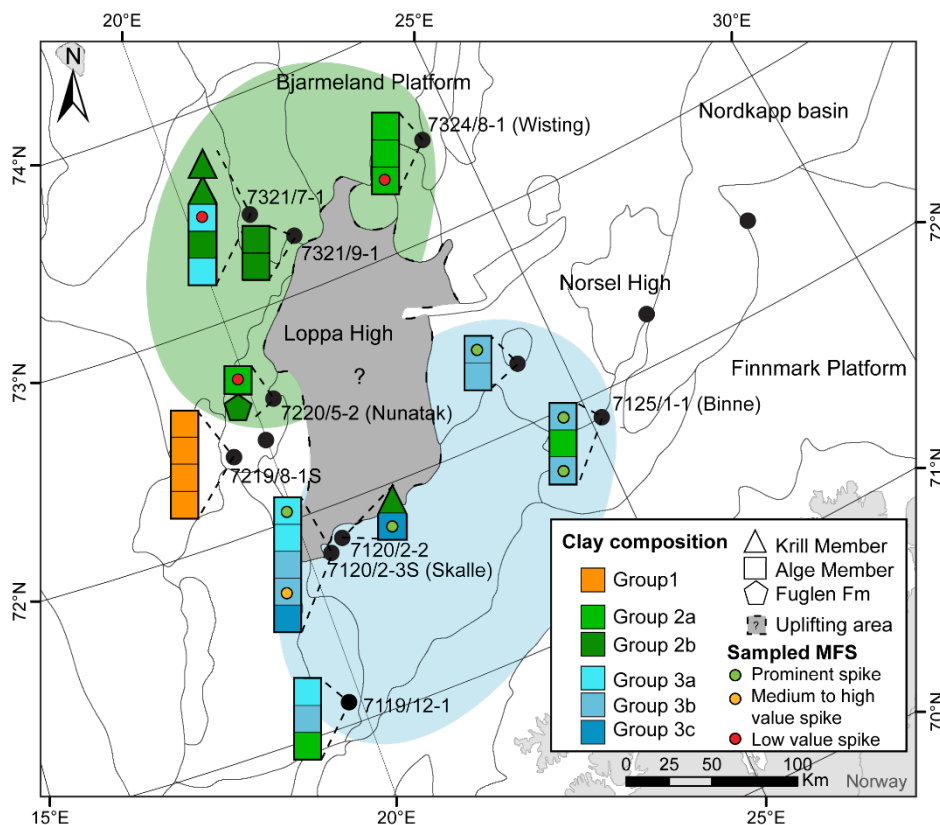


**Fig. 16** Distribution of the clay minerals by the groups defined in Table 6. The distribution showed that group 1, consisting of illite as the only clay mineral, was only occurring in one well (7219/8-1S). Group 2, containing chlorite, interlayered smectite-illite and kaolinite, was mainly concentrated on the west-northwestern side of the Loppa High. Group 3, containing smectite-illite and kaolinite, was mainly present southeast of the Loppa High and eastward. The sampled MFSs with prominent spike all belong to group 3. However, a low gamma-ray value spike was also encountered in this group. The samples belonging to group 2 had low value spikes in the sampled MFS. The current configuration of the Loppa High was marked in grey to illustrate that the area was uplifted and still uplifting at the time, but with an uncertain extent.

## **Interpretation**

Illite, kaolinite and chlorite all reflect continental weathering and fluvial transport into the Barents Sea (Weaver, 1958; Leckie et al., 1998; Haldar & Tišljarić, 2014b). Illite clay minerals favour high potassium and low silica concentration in the sediments and are a result of the weathering of feldspars and micas (Langmuir, 1997). Smectite is a weathering product from iron (Fe) -, magnesium (Mg) - and calcium (Ca) rich minerals, and is favoured at alkaline pH, high silica and low potassium concentration. Smectite is often associated with the weathering of bentonites, beds of volcanic ash (Nadeau & Reynolds, 1981; Pevear et al., 1982). Smectite or interlayered illite-smectite will gradually transform to illite during burial diagenesis (Velde & Vasseur, 1992; Cuadros & Linares, 1996). Smaller smectite particles (<0.1 µm) have proven to be more unstable, thus the particle size controls the transformation time (Huang et al., 1993), this may explain the shallow transformation observed in well 7120/2-3S (Fig. 14). Kaolinite is a weathering product of potassium feldspar and muscovite in metamorphic rocks. The mineral is stable at acid-weathering conditions and is commonly found in humid soil and in river sediments (Weaver, 1958; Langmuir, 1997). Chlorite might be formed during low-grade metamorphism, or detrital from the weathering of sodium (Na)-, Ca-, Mg- and Fe-rich basement or igneous rocks (Langmuir, 1997; Haldar & Tišljarić, 2014a).

The southwestern Barents Sea was surrounded by igneous provinces and exposed basement as a result of the Cambrian and the Uralian orogenies, making it difficult to distinguish possible source areas for the clay minerals (Ritzmann & Faleide, 2007). The distribution of the clay minerals does however suggest that the area west of the Loppa High could have closer proximity to a mafic source of chlorite. On the other hand, chlorite functions as an alternative source for iron (Fe) during pyritization if there is iron depletion in the bottom water (Grossman et al., 1979). Thus, the lack of chlorite in the Alge Member in the areas located south of the Loppa High and eastward toward the Nordkapp Basin suggests that this area experienced highly reducing conditions during deposition.

Illite is formed as a replacement for both smectite and kaolinite in late diagenesis, thus a deep burial of the Alge Member could explain the lack of kaolinite and smectite in well 7219/8-1S. The well is drilled in subsiding basin between the Loppa High and the Veslemøy High (Line A-A'; Fig. 3), indicating that burial and the accompanying diagenetic processes can explain the lack of kaolinite and smectite in this well.

## 4.2 Geochemical composition

### Observations

The Rock-Eval analysis shows that the amount of free hydrocarbons present in the samples before the analysis was low (the S1 value; Table 7). A greater variation is observed in the S2 value (the amount of hydrocarbons produced during the thermal pyrolysis), which displays values above 30 mg/g in samples from wells 7120/2-3S, 7125/1-1, 7224/7-1, 7226/11-1 and 7228/9-1S. The lowest generating potential in the Alge Member is in well 7219/8-1S, where the S2 value in all samples are less than 0.7 mg/g. The CO<sub>2</sub> yield of the thermal breakdown of the kerogen (S3) is low in all samples (Table 7).

High Tmax values (>460 °C) are seen in 2 wells, 7219/8-1S and 7321/7-1 (Table 7). In addition, well 7119/12- displays high values, with measurements above 450 in two out of three samples. The lowest measurements of Tmax can be observed in wells 7125/1-1, 7224/7-1, 7226/11-1 and 7228/9-1S where all samples have a Tmax below 430 °C.

The maturity assessment derived from the production index (PI) shows immature values below or around 0.1 in wells 7125/1-1, 7224/7-1, 7226/11-1 and 7228/9-1S, while the highest values (>0.3, oil cracking) are present in wells 7120/2-2, 7219/8-1S and 7321/7-1. The majority of the samples have a PI at around 0.2 (oil generation).

Wells 7120/2-2, 7219/9-1, 7220/5-2, 7321/9-1 and 7324/8-1 all contain samples with low TOC values, which in this dataset is values below 4 % (Table 7). The highest TOC values can be observed in wells 7120/2-3S, 7125/1-1, 7224/7-1, 7321/7-1, 7226/11-1 and 7228/9-1S, which all contain one or more samples with more than 10 % TOC (Table 7).

The highest hydrogen index (HI) is seen in the wells 7120/2-3S, 7125/1-1, 7219/9-1, 7224/7-1, 7321/9-1, 7324/8-1, 7226/11-1 and 7228/9-1S, all containing samples with more than 200 mg hydrogen/carbon (H/C)/g TOC. HI values below 65 mg (H/C)/g TOC are observed in the Alge Member in well 7321/7-1, while the samples from well 7219/8-1S contain the lowest measured HI in the dataset with values below 10 mg (H/C)/g TOC. The HI in combination with the oxygen index (OI) shows that the dominating kerogen types in the dataset are kerogen types II–III, followed by type I and a mixture of II and III (Fig. 17). Fig. 17 also display a correlation between high Tmax values and kerogen type III and IV.

**Table 7** Results from the Rock-Eval pyrolysis and TOC measurements. Well and depth marked with green are from the Krill Member, while blue is from the Fuglen Formation.

Well	Depth (m)	S1 (mg/g)	S2 (mg/g)	S3 (mg/g)	Tmax (°C)	PI (wt ratio)	HI (mg HC/g TOC)	OI (mg CO2/g TOC)	TOC (%) *
7119/12-1	2586	1.87	4.55	4.25	449	0.29	58	54	7.82
7119/12-1	2595	2.37	7.43	2.33	451	0.24	106	33	7.03
7119/12-1	2608	3.76	11.23	1.55	457	0.25	137	19	8.22
7120/2-2	2635	4.26	7.26	1.09	450	0.37	170	26	4.26
7120/2-2	2640	3.95	12.51	2.07	449	0.30	187		3.93
7120/2-3S	2003	4.11	15.55	2.05	429	0.21	144	19	10.80
7120/2-3S	2005	4.58	29.32	0.57	434	0.14	262	5	11.20
7120/2-3S	2009	4.05	17.84	1.46	431	0.19	189	15	9.44
7120/2-3S	2014	5.96	39.46	0.67	438	0.13	301	5	13.10
7120/2-3S	2016	4.70	33.28	1.01	438	0.12	260	8	12.80
7125/1-1	1366	3.47	51.92	0.81	425	0.06	371	6	14.00
7125/1-1	1380	3.29	35.91	0.96	424	0.08	336	9	10.70
7125/1-1	1398	5.94	54.80	2.30	422	0.10	356	15	15.40
7219/8-1S	4174.1	0.35	0.62	1.64	599	0.36	8	21	7.84
7219/8-1S	4274.7	0.26	0.48	1.17	601	0.35	7	17	6.80
7219/8-1S	4175.2	0.20	0.40	0.45	599	0.33	6	6	7.01
7219/8-1S	4175.7	0.20	0.48	0.98	601	0.29	6	11	8.64
7219/9-1	1905.5	2.5	28.9	0.4	441	0.08	318	4.4	9.1
7219/9-1	1917	2.04	8.00		438	0.2	277		2.89
7220/5-2	1408	2.37	5.59	1.83	432	0.30	170	56	3.29
7220/5-2	1465	3.95	12.51	2.07	429	0.24	53	318	3.93
7224/7-1	836	2.28	35.14	0.68	418	0.06	308	6	11.40
7224/7-1	848	1.97	24.96	2.45	415	0.07	223	22	11.20
7321/7-1	1924	2.63	4.79	0.87	472	0.35	75	14	6.42
7321/7-1	1933	2.60	4.93	0.95	477	0.35	58	11	8.56
7321/7-1	1939	2.43	4.80	1.25	475	0.34	63	16	7.64
7321/7-1	1951	2.53	4.69	2.53	474	0.35	60	32	7.82
7321/7-1	1963	2.65	6.57	0.78	482	0.29	61	7	10.70
7321/9-1	1350	2.69	8.91	1.41	442	0.23	296	47	3.01
7321/9-1	1360	1.70	7.68	0.49	448	0.18	208	13	3.69
7324/8-1	600	1.07	4.05	1.53		0.21	375	142	1.08
7324/8-1	620	0.09	8.28	0.56	430	0.01	209	14	3.97
7226/11-1	1167	2.80	38.70		425	0.07	328		11.80
7226/11-1	1176	4.14	31.51		427	0.12	337		9.35
7226/11-1	1180	2.40	29.00		421	0.08	377		7.70
7228/9-1S	1045	0.70	17.90		428	0.04	229		7.80
7228/9-1S	1055	1.40	32.60		415	0.04	379		8.60
7228/9-1S	1065	3.90	61.70		410	0.06	414		14.90

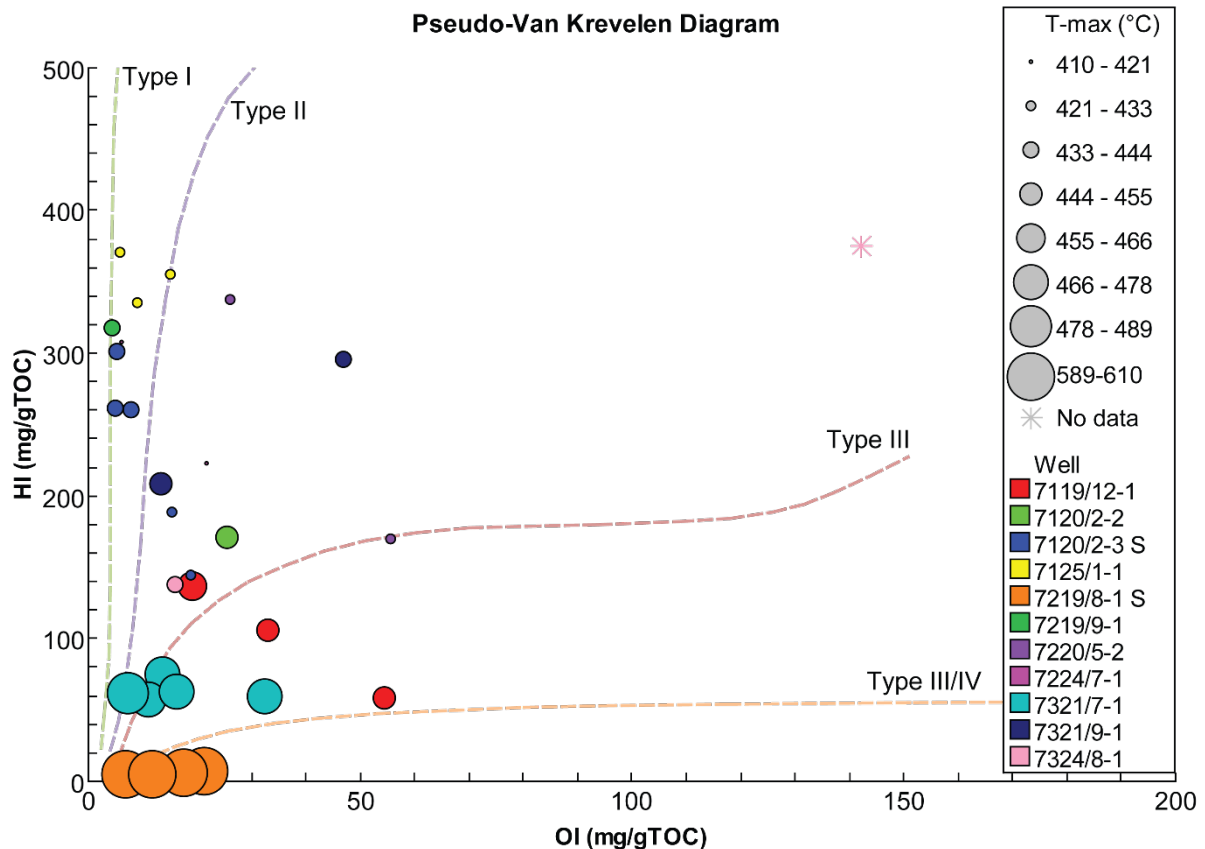


**Fig. 17** Pseudo van Krevelen diagram illustrating the kerogen types for the different samples from the Alge Member. The samples missing OI in the dataset (Table 7) are not represented in the plot. The T<sub>max</sub> value in the samples show that have the lowest HI, plotting as kerogen type III and IV, also have the highest T<sub>max</sub> measurements

In general, the highest TOC values (~10 wt. %) are concentrated in the easternmost part of the study area, surrounding the Nordkapp Basin, on the Bjarmeland Platform and in the Hammerfest Basin (Fig. 18). In the same wells, 7120/2-3S, 7125/1-1, 7224/7-1, 7226/11-1 and 7228/9-1S, the Alge Member has a high generation potential (S<sub>2</sub>), and contain kerogen type I–II. The samples from wells located west and northwest of Loppa High display lower TOC content, lower S<sub>2</sub> and kerogen type II–III (Fig. 18). Kerogen type IV is concentrated in the basinward areas west of the Loppa High (Fig. 18).

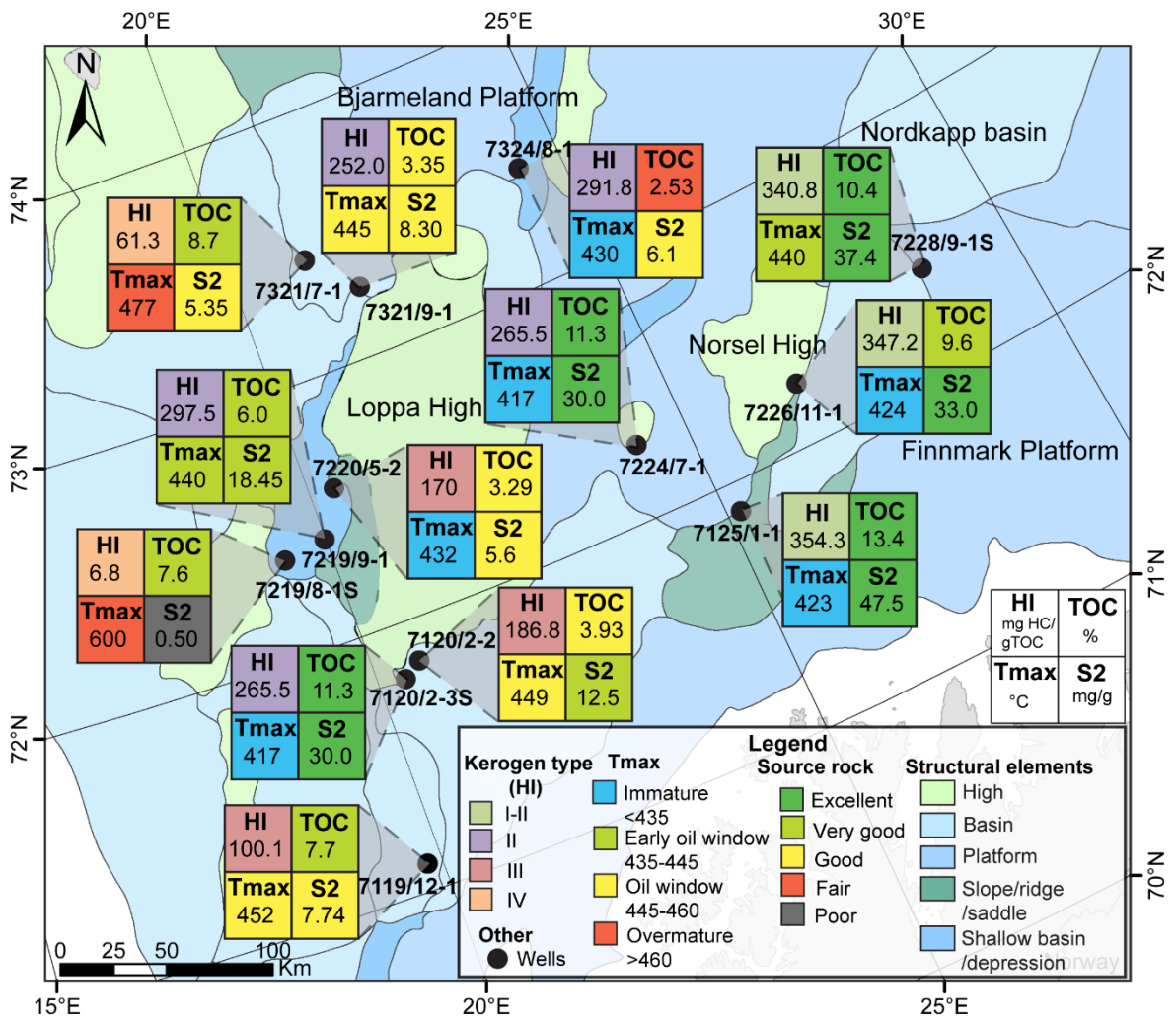


**Fig. 18** Map illustrating the variation in petroleum generating potential in the samples from the study area. The majority of the wells contain kerogen type I and II and are immature to early oil window based on the Tmax. The high S2 and low Tmax in several of the wells reflects great hydrocarbon production potential, but the burial of the source rock was not deep enough to start production. Please note that the values stated in this figure are the average-value of all the samples from the Alge Member collected in each well

PCA of the Rock-Eval and TOC data exhibit that the variation in the dataset is controlled by the S2, Tmax, HI, oxygen index (OI) and the TOC values (Table 8). When plotting the principal components against each other, two samples stand out from the dataset, one with a prominent spike (7120/2-3S-2003) and one with no spike in the MFS (7220/5-2-1408) plots opposite of each other (Fig. 19). 7120/2-3S-2003 display a high TOC and high S2, combined with a relatively low HI. 7220/5-2-1408 display low S2, low TOC, low HI and a low Tmax. The rest of the sampled spikes (Table 3) show a random distribution in the plot (Fig. 19).

**Table 8** The variables in the geochemical composition that have the strongest correlation with the principal components, and thus causing the greatest variation in the dataset. The variables with positive or negative value the furthest from zero correlate the strongest to the principal component.

Variable	Comp. 1 (52.5 %)	Comp. 2 (46.79 %)	Comp. 3 (0.6 %)
S2	0.121	0.0664	-0.069
Tmax	-0.401	0.915	-0.0302
HI	0.907	0.396	0.0416
OI	-0.0417	0.0155	0.994
TOC	0.0132	0.0337	-0.0043

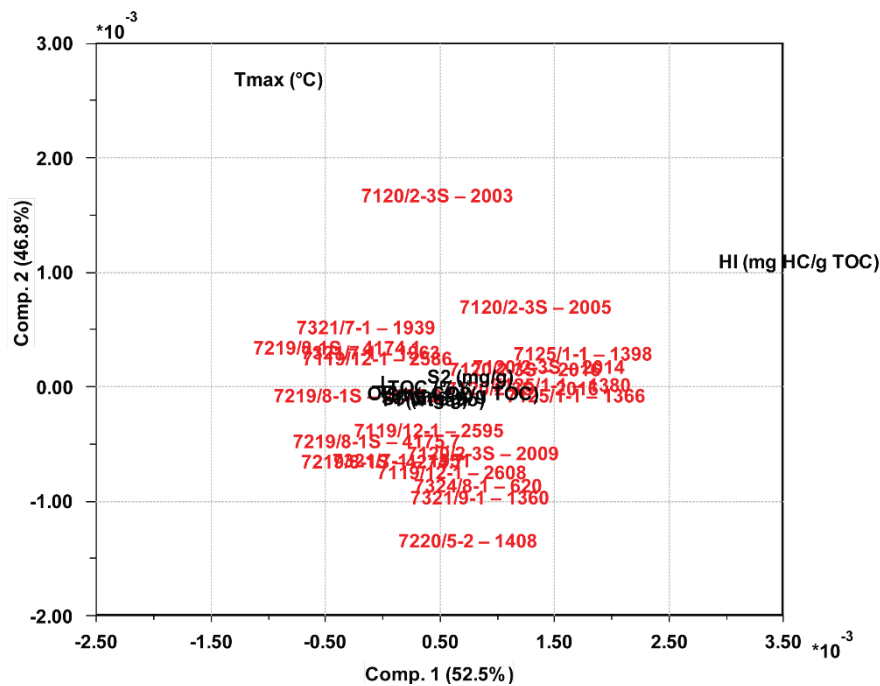


**Fig. 19** Sample 7120/2-3-2003 and 7220/5-2-1408 positioned themselves on opposite sides of the dataset when plotting PC1 and PC2 for the organic geochemistry against each other. The rest of the sampled spikes seem to be randomly distributed.

## Interpretation

The geochemical analyses showed that the organic geochemical composition and source rock potential within the Alge Member varies throughout the study area (Table 7; Fig. 18). The greatest generating potential (S2) in combination with high TOC and kerogen type I and II in the wells located around the Nordkapp Basin, on the Bjarmeland Platform and in the Hammerfest Basin gives these wells the best source rock potential in the area (Fig. 18). However, the low Tmax and PI values of the wells indicate that the source rock is immature in these wells (Table 7).

Toward the west of the study area, the HI and the generation potential decreases as the Tmax increases, indicating that the source rock located in these areas has an increased maturity. The

Tmax value can be used as an indirect indicator of the burial depth the sample have experienced. When a source rock is buried, the generation of hydrocarbons will start when the activation energy to crack kerogen is high enough, and the energy need increases as the hydrocarbons get more complex (Hunt, 1996). High Tmax values suggests that the hydrocarbons with the lowest activation energy have been produced, and the maximum production of hydrocarbons during pyrolysis will occur at a higher temperature. The samples from wells 7219/8-1S and 7321/7-1 display high Tmax values, in combination with a high PI, low S2 and kerogen type IV, indicating that the kerogen that is left in the source rock has little to no generation potential. The wells are located basinward west of the Loppa High, and the Alge Member deposited in this area can be assumed to have experienced deeper burial than the rest of the study area.

The geographical distribution of the kerogen types suggests a more lacustrine input in the area surrounding the Nordkapp Basin where kerogen types I and II is the most common (Fig. 17; Fig. 18). The lacustrine input might have been transported from land, or it could be related to the halokinetic activity in the Nordkapp Basin during the Middle-Upper Jurassic where areas might have been isolated due to the salt movement allowing lacustrine deposition (Gabrielsen et al., 1990, Rojo & Escalona, 2018). The wells closer to the Loppa High consist of kerogen type II and III, representing marine and terrestrial depositional environment receptivity. The terrestrial kerogen could be transported into the Barents Sea from land, or it might be sourced from the already uplifted parts of the Loppa High in the northernmost areas.

Some wells display a lower TOC content in the samples (e.g. 7120/2-2, 7220/5-2, 7321/7-1, 7321/9-1) than the 6–16 wt. % usually observed in the Alge Member (Fig. 18; Smelror et al., 2001). This might be an indication of variation in preservation potential of organic matter in the study area or less input of organic material to the location of these wells. Another possibility is that the organic matter is preserved, but a higher sediment input in these areas causes a decrease in the TOC values. The wells with low TOC values are located close to the active fault complexes at the time and the uplifting Loppa High (Gabrielsen et al., 1990), which could support that there is a higher sediment input at the location of the wells.

The PCA of the geochemical data implies that the source rock properties of the Alge Member may be relevant for the spike prominence. However, the random distribution of the rest of the sampled MFS indicates that the geochemical data and source rock quality are not the main controls on the high-value prominent gamma-ray spikes.

### 4.3 Mineral & maceral composition

The results from the maceral analysis were divided into mineral matter and the maceral groups including solid bitumen (Table 9).

**Table 9** The counted grains for the maceral analysis, here divided into minerals and maceral groups. The wells and depths marked with green are from the Krill Member, whereas the blue belongs to the Fuglen Formation. The grouping named others comprise the minerals with overall few counts, and include calcite, chitin and sulfides.

Sample Well	Depth (m)	Mineral matter				Solid bitumen			
		Clay minerals	Quartz	Pyrite	Other	Total	Vitrinite Total	Liptinite Total	Inertinite Total
7119/12-1	2586	126	90	24	9	9	9	30	3
7119/12-1	2595	142	52	30	19	22	3	26	6
7119/12-1	2608	79	136	22	25	20	4	10	4
7120/2-2	2640	123	37	25	2	62	3	45	3
7120/2-3S	2003	121	14	114	4	26	0	21	0
7120/2-3S	2005	138	25	55	0	34	1	43	4
7120/2-3S	2009	120	19	83	7	28	1	40	2
7120/2-3S	2014	111	44	26	4	45	0	67	3
7120/2-3S	2016	91	50	45	5	46	3	55	5
7125/1-1	1366	134	22	27	6	52	3	52	4
7125/1-1	1380	104	106	18	6	32	3	30	1
7125/1-1	1398	124	54	3	25	69	5	18	2
7219/8-1S	4174.1	139	45	13	22	63	2	16	0
7219/8-1S	4274.7	128	48	18	19	73	0	10	4
7219/8-1S	4175.2	125	42	15	14	90	1	11	2
7219/8-1S	4175.7	133	50	19	18	61	0	18	1
7220/5-2	1408	35	224	15	5	8	1	12	0
7220/5-2	1465	103	142	1	15	13	8	17	0
7321/7-1	1924	103	116	20	4	47	0	10	0
7321/7-1	1933	127	65	21	1	69	0	15	2
7321/7-1	1939	111	100	12	5	54	2	14	2
7321/7-1	1951	145	71	24	10	33	0	17	0
7321/7-1	1963	154	72	17	3	41	0	13	0
7321/9-1	1350	58	194	24	6	8	0	10	0
7321/9-1	1360	40	190	31	7	14	4	14	0
7324/8-1	600	17	265	7	6	5	0	0	0
7324/8-1	610	51	201	23	1	12	3	9	0
7324/8-1	620	47	218	10	1	9	8	7	0

### 4.3.1 MINERAL COMPOSITION

#### Observations

Quartz and clay minerals are the most abundant and their presence are inversely proportional to one another. Samples from wells 7220/5-2 (Nunatak), 7321/9-1 and 7324/8-1 (Wisting) contain the most quartz, while well 7120/2-3S (Skalle) displays a relatively high amount of pyrite in all the collected samples (Fig. 20). The wells with a prominent spike in the sampled MFS contain a higher percentage of clay and pyrite, except in well 7125/1-1 where the sampled prominent spike display a relatively low amount of pyrite (Fig. 20). In well 7220/5-2 (Nunatak) and in 7324/8-1, the sampled MFS had a low-value peak and the samples showed a higher quartz content. This was not the case for the Alge Member in well 7321/9-1 where the clay content is dominant, but there is no prominent peak (Fig. 20). There seems to be a correlation between high clay content and, in some cases, high pyrite content and the high-value gamma-ray spike in the MFS, whereas the more quartz-rich MFS-samples did not display a high gamma-ray value (Fig. 20).

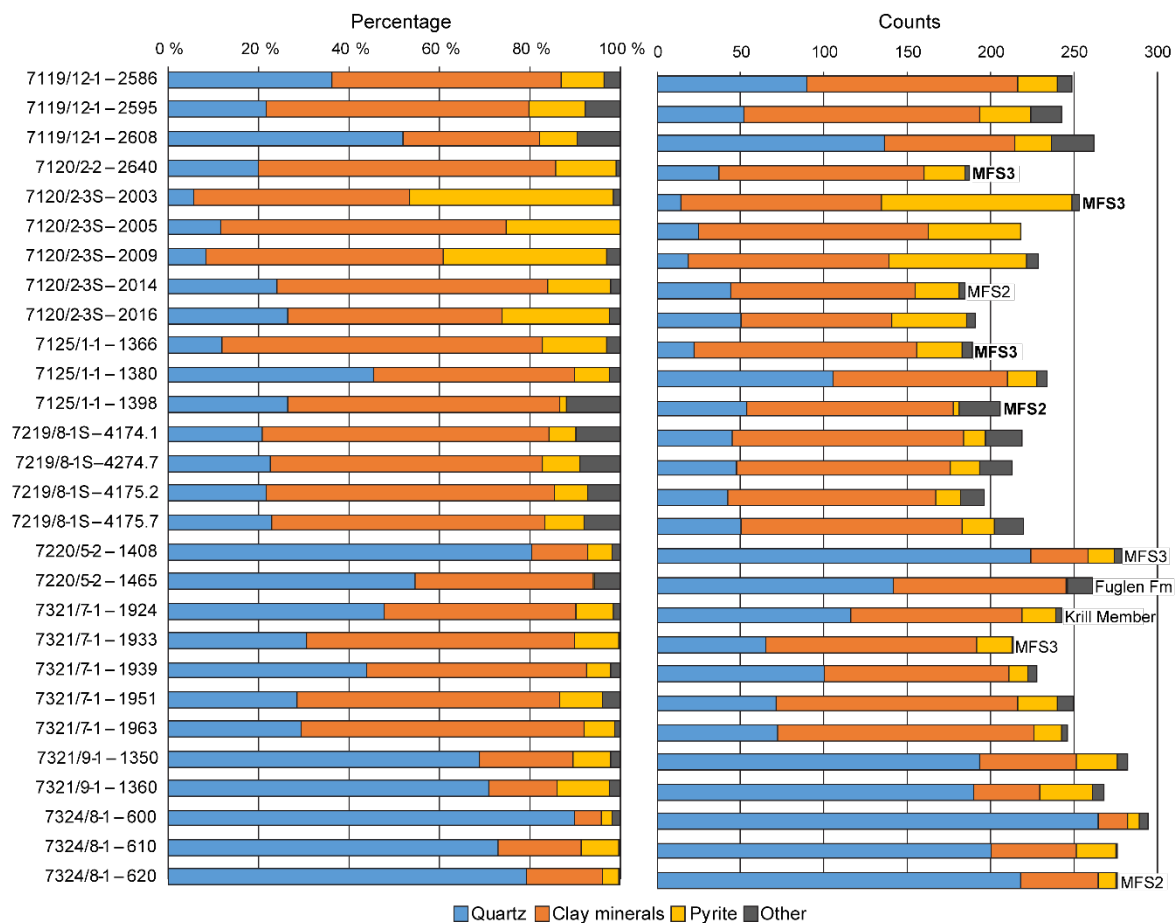


**Fig. 20** The mineral percentage and count for each sample. The amount of quartz and clay in the samples are inversely proportional. Note the high quartz content in 7220/5-2, 7321/9-1 and 7324/8-1, and the high pyrite content in 7120/2-3S. The samples that do not belong to the Alge Member is marked on the chart as well as sampled depths that correlate with a MFS. The MFSs in bold text have a prominent spike at the sampled depth. The grouping named others comprise the minerals with overall few counts, and include calcite, chitin and sulphides. Abbreviation: Fm=Formation.

Moreover, there seems to be a correlation between the sampled depths with a high gamma-ray value and a low percentage of quartz in the mineral composition (Fig. 21). Even though the highest gamma-ray values can be found in samples with low quartz content, there is also low-value gamma-ray measurements in samples with the same clay and quartz composition as high-value spikes are observed (Fig. 21).

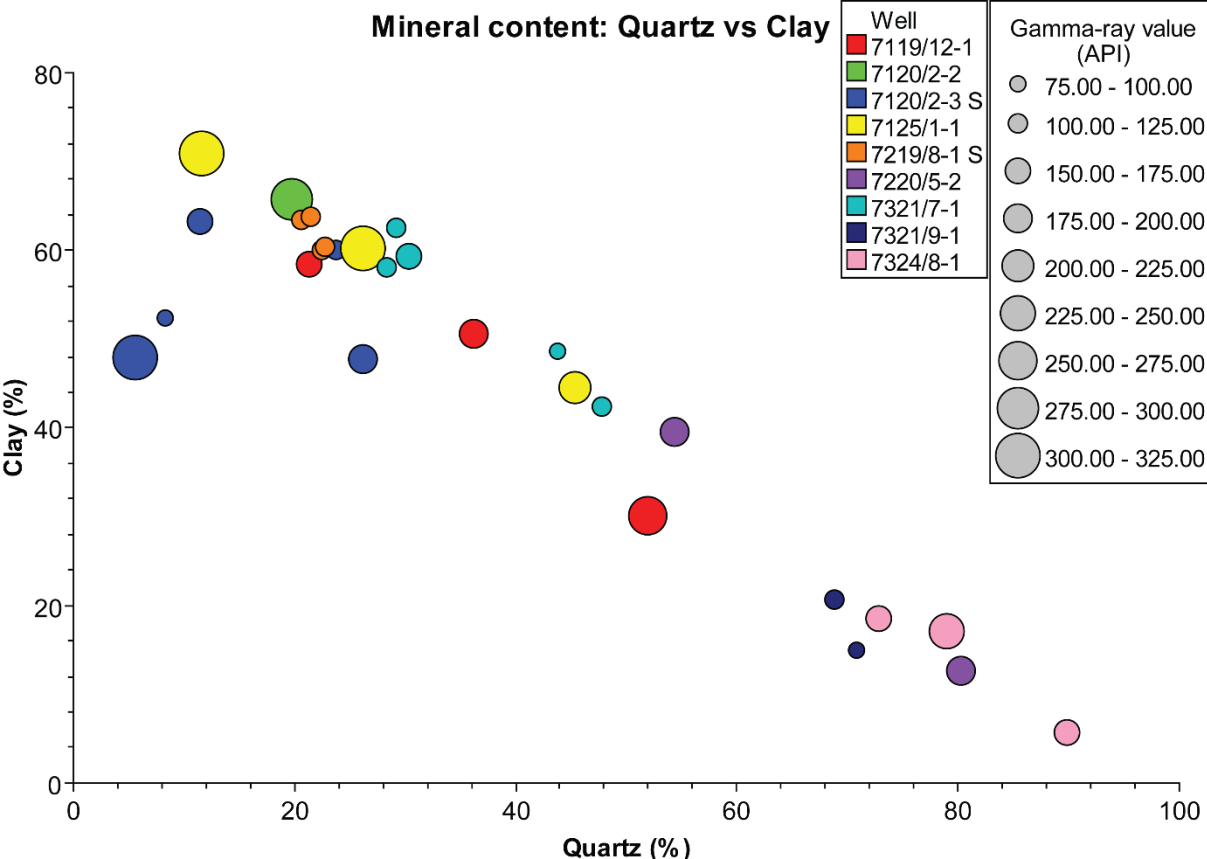


**Fig. 21** The relationship between the clay and quartz to the gamma-ray value in API measured at the sampled depth display the relationship between quartz and clay in the samples, and display that the largest values are found in the clay-rich samples. However, low gamma-ray values can also be observed in the clay rich samples.

The samples with the highest quartz content have low gamma-ray values, and are all positioned relatively close to one another west of the Loppa High (Fig. 21; Fig. 22). The Alge Member sampled in the wells closest to the Loppa High have a higher quartz content than in the more basinward located wells (e.g. well 7321/9-1, 7220/5-2 and 7324/8-1 all display a quartz content of 70 % and more, while the basinward located wells, 7219/8-1S and 7321/7-1, contain less than 35 %). This is not the case in the southern part of the Loppa High, where samples from the Alge Member display a high clay and pyrite content (Fig. 22). The highest mineral content in samples occurred in 7324/8-1 (Wisting), 7321/9-1, 7321/7-1, 722075-2 (Nunatak) and 7119/12-1.

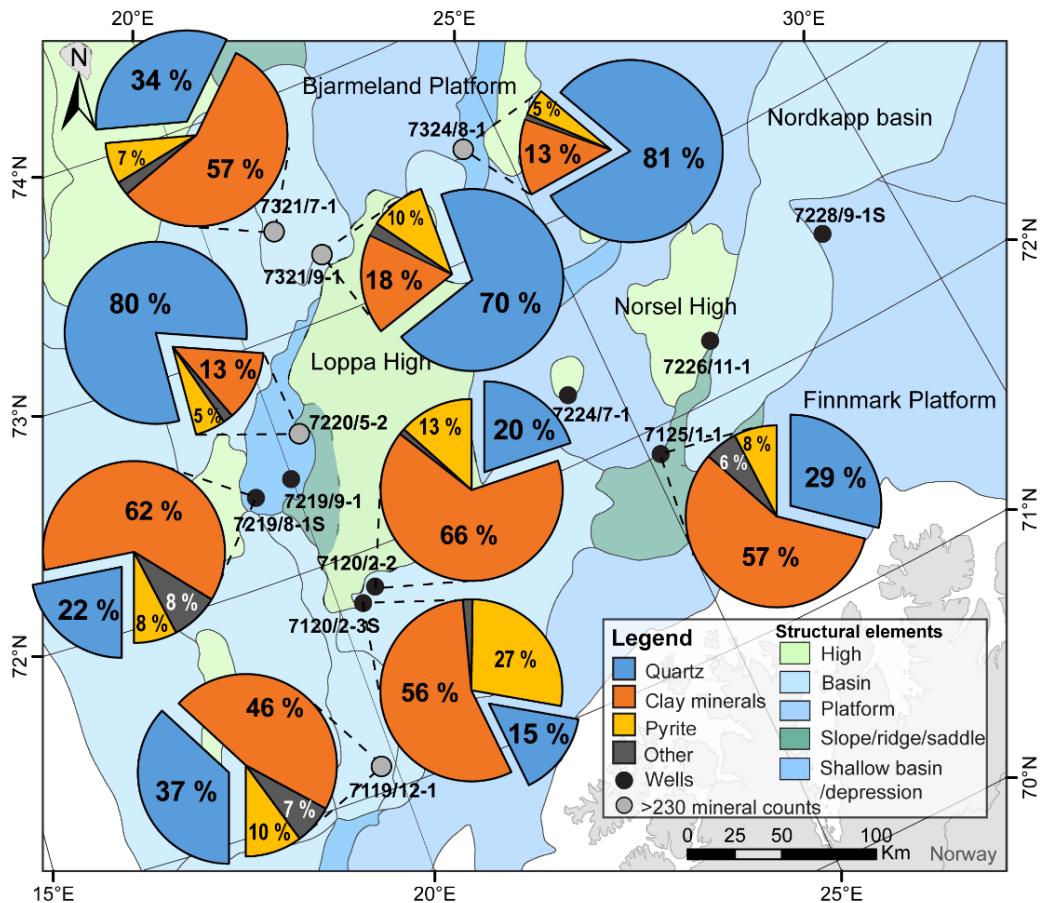


**Fig. 22** Map with pie charts illustrating the mineral distribution in the study area. The quartz-content might be used as indicator of areas with tectonic activity. The percentage calculation is based on the mean of all the samples representing the Alge Member for each well. Values below 2 % were not display with numbers. The grouping named others comprise the minerals with overall few counts, and include calcite, chitin and sulphides.

### Interpretation

The occurrence of the prominent spikes in clay-rich samples indicates that either clay minerals or the depositional environment of the clay minerals could cause or influence the presence of the high-value spikes in the gamma-ray log. However, the low-value gamma-ray readings also present in the clay-rich samples suggest that these factors do not control the high-value gamma-ray spikes alone.

The high amount of quartz present in the samples from wells to the west and northwest of the Loppa High could reflect tectonic activity in the Bjørnøyrenna Fault Complex and the Hoop Fault Complex. Uplift of the Loppa High would function as a new sediment source to the adjacent basins, thus causing the high quartz count in the wells close to the high. The quartz content in the wells west and northwest of the Loppa High, show that the area closest to the Loppa High experienced a higher quartz input than more basinward. The mineral composition in the Hammerfest Basin, on the other hand, indicate that there was little or no activity in the

Asterias Fault Complex at the time the Alge Member was deposited. The relatively high pyrite content in the Hammerfest Basin implies good conditions for pyrite formation; available iron and sulfur and a redoxcline in the proximity to the sediment-water interface (Wilkin et al., 1996; Gallego-Torres et al., 2015). The high content of clay and pyrite in the samples may, therefore, suggest anoxic deposition. The higher mineral content relative to the maceral content is concentrated around the active fault zones (i.e. the Hoop Fault Complex, the Bjørnøyrenna Fault Complex and the Ringvassøy-Loppa Fault Complex). This indicates that the active faulting decreased the preservation potential of the organic matter in the source rock.

The high quartz content observed in the western and northwestern samples will increase the brittleness of the shale, and thus influence the sealing qualities of the Alge Member in these areas (Jarvie et al., 2007). A brittle source rock is more likely to fracture when experiencing pressure, which will allow primary migration of hydrocarbons, but also decrease the sealing qualities of the rock (Jarvie et al., 2007). Higher clay-mineral content gives the source rock ductile qualities, thus there will be a decrease in the efficiency of the primary migration of hydrocarbons, but improved sealing qualities (Jarvie et al., 2007). The wells where the Alge Member has the highest quartz content (i.e. 7220/5-2, 7321/9-1 and 7324/8-1; Fig. 22) also display some of the lowest TOC values in the dataset (Fig. 18), thus indicating that the high quartz content may affect the preservation potential of organic matter.

### 4.3.2 MACERAL COMPOSITION

#### Observations

The maceral group composition of the samples (Fig. 23) revealed that solid bitumen and liptinite were the most abundant macerals, followed by vitrinite. Internitine was absent in several of the samples and was only present in small amounts in wells located in the southernmost part of the study area (Fig. 24). Wells 7219/8-1S and 7321/7-1 contained relatively high amounts of solid bitumen, whereas 7119/12-1 and 7220/5-2 (Nunatak) contain slightly less. There is no clear correlation between the maceral content and the prominent spike in the MFS. Samples from wells 7219/8-1S, 7120/2-2, 7120/2-3S and 7125/1-1 display an overall higher maceral count than the samples from the other wells (Fig. 23; Fig. 24).

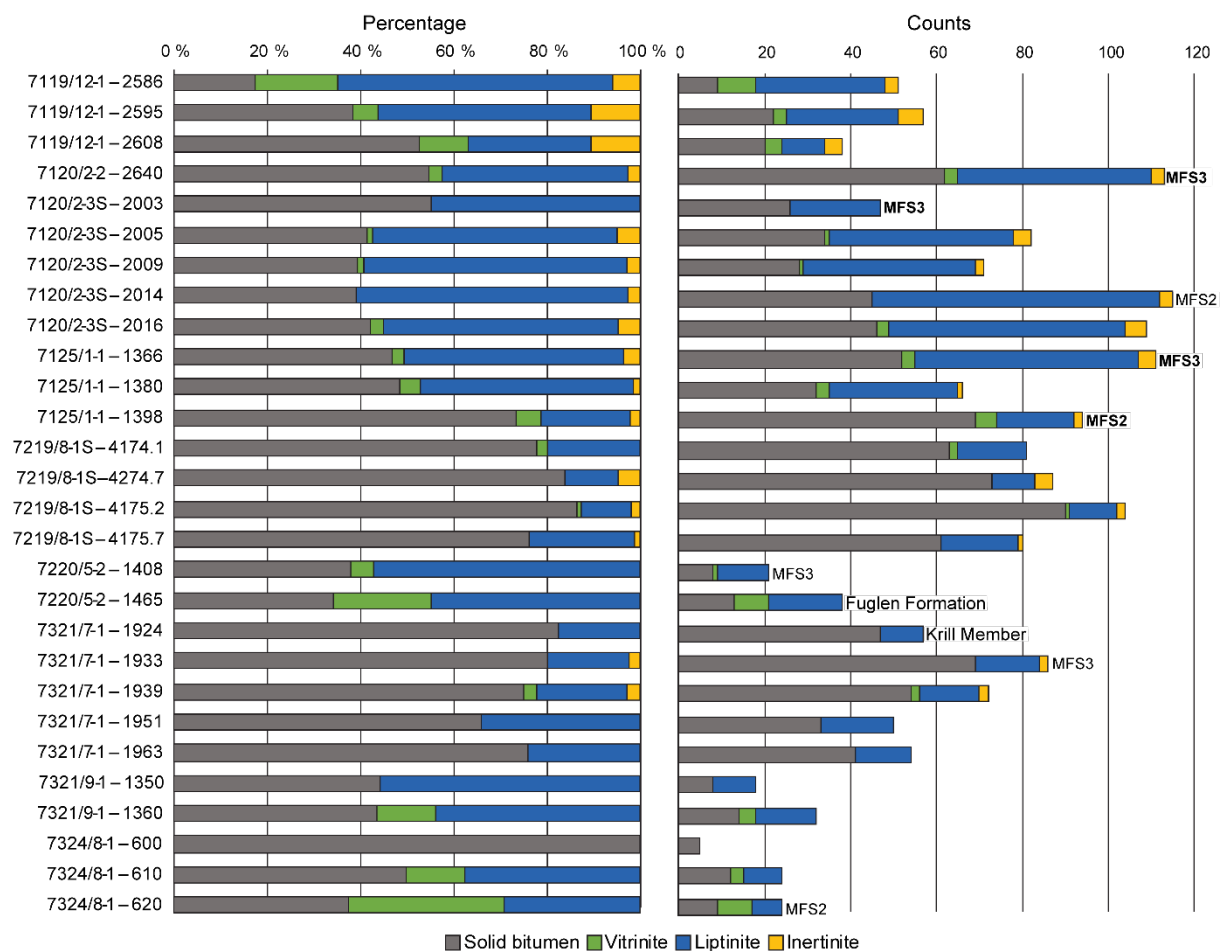


**Fig. 23** The maceral-count for each of the samples. Solid bitumen and liptinite is the main component. The samples that do not belong to the Alge Member are marked on the chart as well as sampled depths that correlate with a MFS. The MFS's in bold text have a prominent spike at the sampled depth.

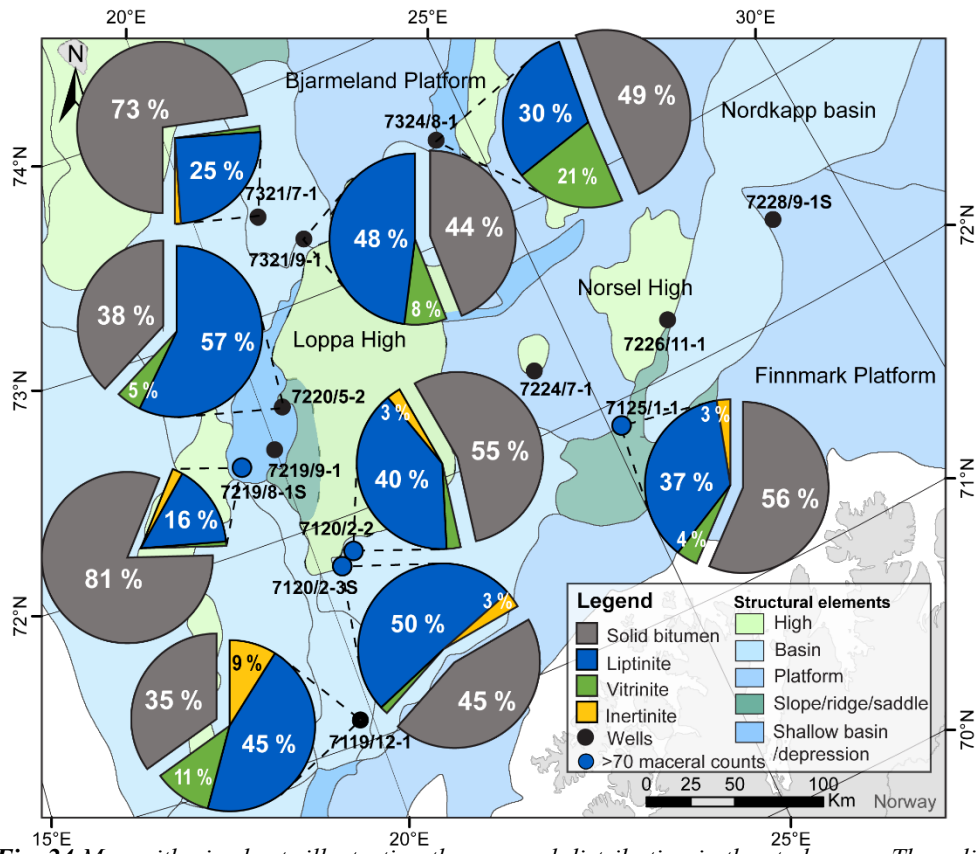


**Fig. 24** Map with pie charts illustrating the maceral distribution in the study area. The solid bitumen dominated the maceral count in most of the samples and is highlighted in the figure. The percentage calculation is based on the mean of all the samples representing the Alge Member for each well. Values below 2 % were not displayed with numbers. The wells marked in blue represent the wells with the highest maceral content.

The three maceral groups were further identified by their origin (Table 10) and this allowed further division of the macerals. The liptinite with marine origin includes sporinite, dinoflagellates and acritarchs, lamalginite, degraded lamalginite and amorphinite, all derived from marine plankton and algae. Terrestrial liptinite includes terrestrial sporinite and resinite, derived from spores/pollen and waxy plant parts, respectively. All vitrinite is derived from the woody plant material and represent terrestrial input, whereas the terrestrial liptinite implies near coast deposition and the marine liptinite display true marine conditions (Demchuck, personal communication, March 1, 2019). The distribution of the terrestrial and marine macerals in the samples (Fig. 25) display vertical variation within each well. The highest amount of terrestrial material is observed in the northernmost well 7324/8-1 (Wisting). However, there is relatively high terrestrial input also in the southernmost and easternmost wells, 7119/12-1 and 7125/1-1 (Binne) and well 7220/5-2 (Nunatak) located west of the Loppa High.

**Table 10** The types of counted macerals present in the samples. The wells and depths marked with green are from the Krill Member, while the blue belongs to the Fuglen Formation.

Well	Depth (m)	Solid Bitumen			Vitrinite		Liptinite										Inertinite			
		Wurtzilite	Imposonite	Gilsonite	Primary	Detrovitrinite	Sporinite dinoflagellate & Acritarch	Sporinite terrestrial	Resinite	Lamalginite	Colonial Alginite	Liptodetrinite	Exsudatinite	Degraded Lamalginite	Amorphinite	Live Hydrocarbons	Fusinite	Semifusinite	Macrinite	Inertodetrinite
7119/12-1	2586	5	4	0	7	2	4	1	0	1	2	12	0	0	10	0	1	2	0	0
7119/12-1	2595	12	9	1	0	3	2	0	0	0	1	16	6	0	1	0	1	3	0	2
7119/12-1	2608	14	6	0	2	2	1	0	0	0	0	8	0	0	1	0	1	3	0	0
7120/2-2	2640	32	30	0	1	2	0	0	0	1	16	21	1	0	6	0	0	0	2	1
7120/2-3S	2003	14	10	2	0	0	7	1	0	0	0	13	0	0	0	0	0	0	0	0
7120/2-3S	2005	13	19	2	0	1	3	3	0	1	4	25	2	2	3	0	1	0	3	0
7120/2-3S	2009	17	10	1	1	0	6	3	0	2	8	18	1	1	1	0	1	1	0	0
7120/2-3S	2014	29	16	0	0	0	2	2	0	2	21	37	1	0	2	0	2	0	1	0
7120/2-3S	2016	30	16	0	0	3	1	1	1	3	22	24	0	0	3	0	3	0	1	1
7125/1-1	1366	29	23	0	1	2	3	2	0	2	10	34	0	0	1	0	3	0	0	1
7125/1-1	1380	18	14	0	0	3	3	2	0	0	5	17	0	2	1	0	1	0	0	0
7125/1-1	1398	54	15	0	1	4	0	4	1	0	1	11	0	0	1	0	1	0	1	0
7219/8-1S	4174.1	0	63	0	1	1	3	0	0	0	1	11	0	1	0	0	0	0	0	0
7219/8-1S	4274.7	73	0	0	0	0	0	0	0	0	0	4	0	3	3	0	2	2	0	0
7219/8-1S	4175.2	1	89	0	0	1	0	0	0	0	0	10	0	0	1	0	1	0	0	1
7219/8-1S	4175.7	8	53	0	0	0	0	0	0	1	0	16	0	1	0	0	1	0	0	0
7220/5-2	1408	5	3	0	1	0	4	2	0	0	0	6	0	0	0	0	0	0	0	0
7220/5-2	1465	11	2	0	1	7	1	2	0	0	0	11	1	0	0	2	0	0	0	0
7321/7-1	1924	3	44	0	0	0	0	0	0	0	0	7	0	1	2	0	0	0	0	0
7321/7-1	1933	12	57	0	0	0	0	0	0	0	0	13	1	0	1	0	2	0	0	0
7321/7-1	1939	8	45	1	1	1	0	0	0	0	0	8	4	0	2	0	2	0	0	0
7321/7-1	1951	9	24	0	0	0	0	0	0	1	0	14	2	0	0	0	0	0	0	0
7321/7-1	1963	9	32	0	0	0	0	0	0	0	0	12	1	0	0	0	0	0	0	0
7321/9-1	1350	5	3	0	0	0	1	0	0	0	0	9	0	0	0	0	0	0	0	0
7321/9-1	1360	9	4	1	0	4	5	0	0	0	0	9	0	0	0	0	0	0	0	0
7324/8-1	600	4	1	0	0	0	0	0	0	0	0	0	0	0	0	0	0	0	0	0
7324/8-1	610	12	0	0	1	2	3	1	0	0	0	5	0	0	0	0	0	0	0	0
7324/8-1	620	9	0	0	2	6	0	2	0	0	1	4	0	0	0	0	0	0	0	0

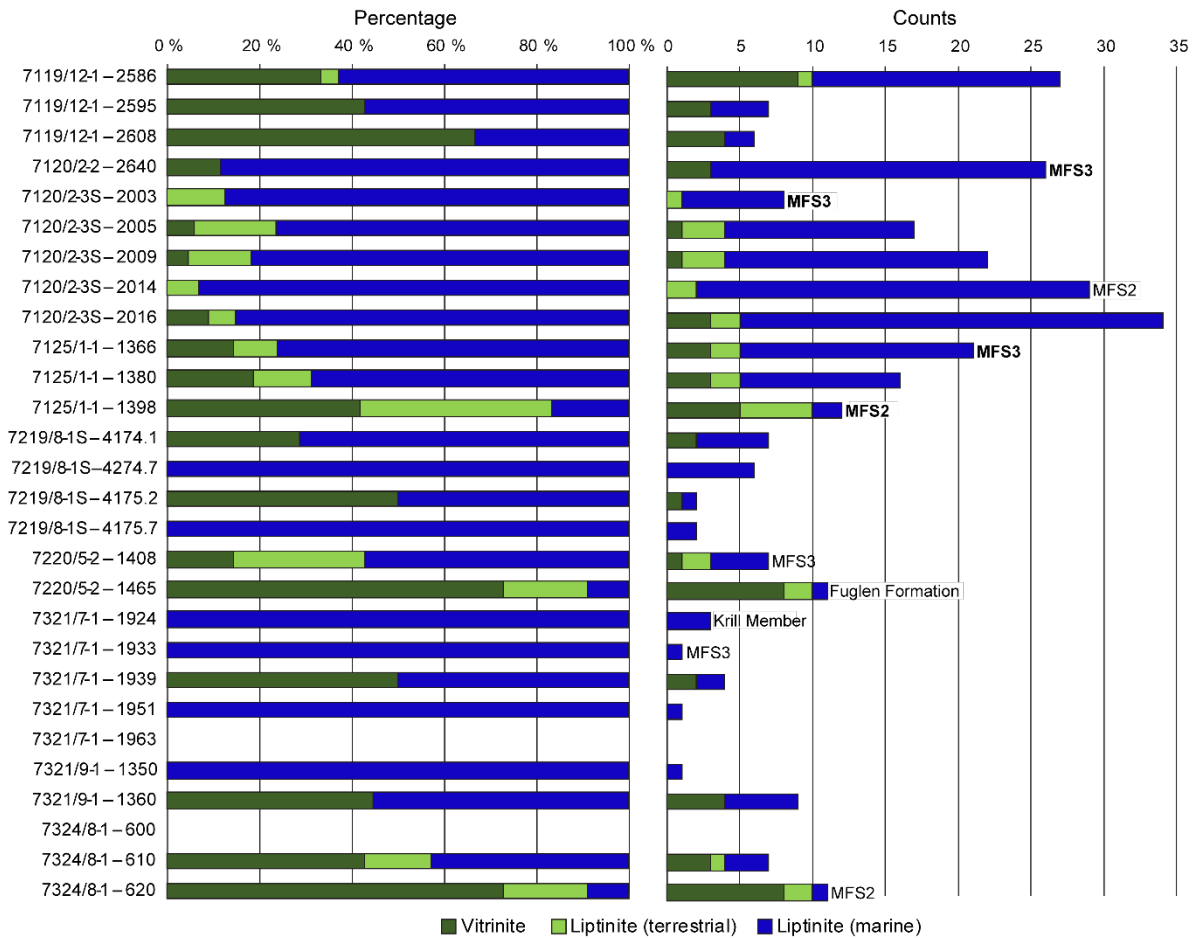


**Fig. 25.** The amount of marine liptinite, terrestrial liptinite and vitrinite (terrestrial) in the samples. The percentage display the vertical variation in the well. The MFS's in bold text have a prominent spike at the sampled depth.

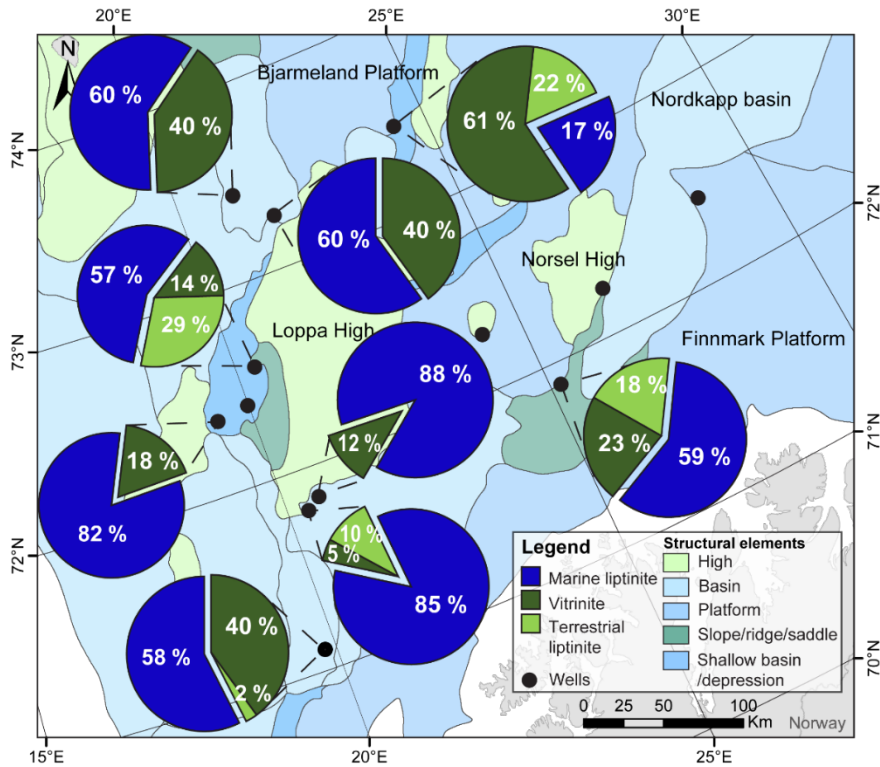


**Fig. 26** Map with pie charts illustrating the distribution of macerals grouped into marine liptinite, vitrine and terrestrial liptinite. The percentage calculation is based on the mean of all the samples representing the Alge Member for each well.

PCA for the combination of mineral and maceral data displays that the quartz and impsomite (solid bitumen) content causes the greatest variation in the dataset followed by pyrite and clay minerals (Table 11). The gamma-ray value showed poor correlation to the other variables.

**Table 11** The variables causing the most variation in the mineral and maceral data according to a PCA. The variables with positive or negative value the farthest from zero correlate the strongest to the principal component.

Variable	PC 1 (59.08 %)	PC 2 (25.25 %)	PC 3 (7.15 %)
Mineral; Quartz	-0.796	0.32	-0.0117
Solid Bitumen: Impsonite	0.158	0.339	-0.638
Pyrite	0.122	0.0161	0.635
Mineral; Clay	0.53	0.597	0.0654
Gamma-ray value	0.176	-0.648	-0.292
Solid Bitumen: Wurtzilite	0.0767	-0.0572	0.281
Liptinite: Liptodetrinite	0.075	0.0144	0.0971
Liptinite: Colonial Alginite	0.0312	-0.0324	0.0797

## Interpretation

The high content of solid bitumen in the basinward wells west of the Loppa High indicates that the source rock has generated hydrocarbons, which partly has been trapped in the source rock. Solid bitumen is a result of thermal maturation of organic material (e.g. oil cracking), and can be found as organic material in fractures and pores in sedimentary rocks (Curiale, 1986; Jacob, 1989). Ohm et al., (in review) suggests that the thickness of clay-rich intervals in the source rock might influence the primary migration of hydrocarbons. Thick clay intervals will inhibit the migration of generated hydrocarbons, and with burial and thermal maturation, create solid bitumen. The Alge Member in the westward basins (well 7219/8-1S and 7321/7-1) is thicker than at other locations with the same clay content (Fig. 22), and display a higher solid bitumen content than areas with thinner clay-rich successions. The maturity (overmature) of the Alge Member in the westward basins may also highly influence the amount of solid bitumen in this area has a higher thermal maturity.

Terrestrial liptinite and vitrinite in the wells imply coastal proximity and terrestrial input of organic matter. The abundance of terrestrial material on the western side of the Loppa High may imply that the high was partially uplifted and hosting terrestrial plants. Other possible sources of the terrestrial material in the region could include the proximity to Greenland (Grundvåg et al., 2017), whereas the Stappen High (and Bjørnøya) was not uplifted during the Late Jurassic (Worsley et al., 2001; Blaich et al., 2017). Well 7324/8-1 (Wisting) was drilled

on an uplifted fault block in the Hoop Fault Complex; hence the terrestrial material might be locally sourced from the Hoop Fault Complex. However, the maceral count in wells closely located to an active fault complex is lower than in basinward wells (e.g. 7219/8-1S) and form the eastern side of the Loppa High. This indicates that the preservation of organic material in these areas was poor. The mean values for the Alge Membe show that there is input of terrestrial material to the Alge Member throughout the study area (Fig. 26). The terrestrial input can be used as an indicator of proximity to a shoreline and hence, tentatively to relative water depth. It would seem that the Polhem Subplatform, the Ringvassøy-Loppa Fault Complex and the wells close to the Nordkapp Basin experienced a shallower water depth during deposition, relative to e.g. Hammerfest Basin, which show a higher content of true marine material. However, both hyperpycnal and hypopycnal flows can transport material far from the shoreline, adding uncertainty to that interpretation.

The PCA confirmed that the quartz and solid bitumen content are the main deviations in the dataset, but also displayed that neither of these variables controls the gamma-ray spike.

## 4.4 Well logs & seismic data

### 4.4.1 AGE & SEDIMENTATION RATE

#### Observations

The chronostratigraphy from the well reports on NPDs webpage (NPD, 2019) revealed that the Alge Member and the MFSs were mostly deposited during the Kimmeridgian (Fig. 27; Fig. 28). The most obvious exception is 7220/5-2 (Nunatak), where MFS2 and most of the Alge Member was deposited during the Callovian–Oxfordian. Deposition of top Alge Member and the MFS3, in wells 7120/2-2 and 7219/9-1, took place during Tithonian.

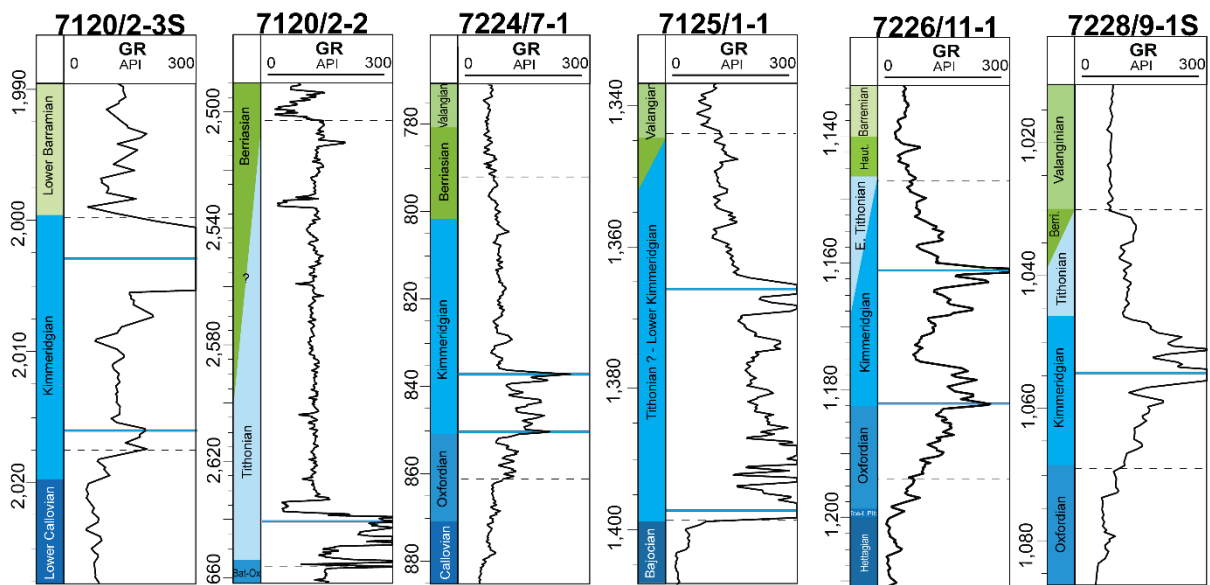


**Fig. 27** The age of the Hekkingen Formation and the MFSs (NPD, 2019). From left to right, the wells are located in the Hammerfest Basin and eastward. The black dashed lines represent the top and base of the Alge Member and the blue lines show the depth of the MFSs. Vertical scale is in m.

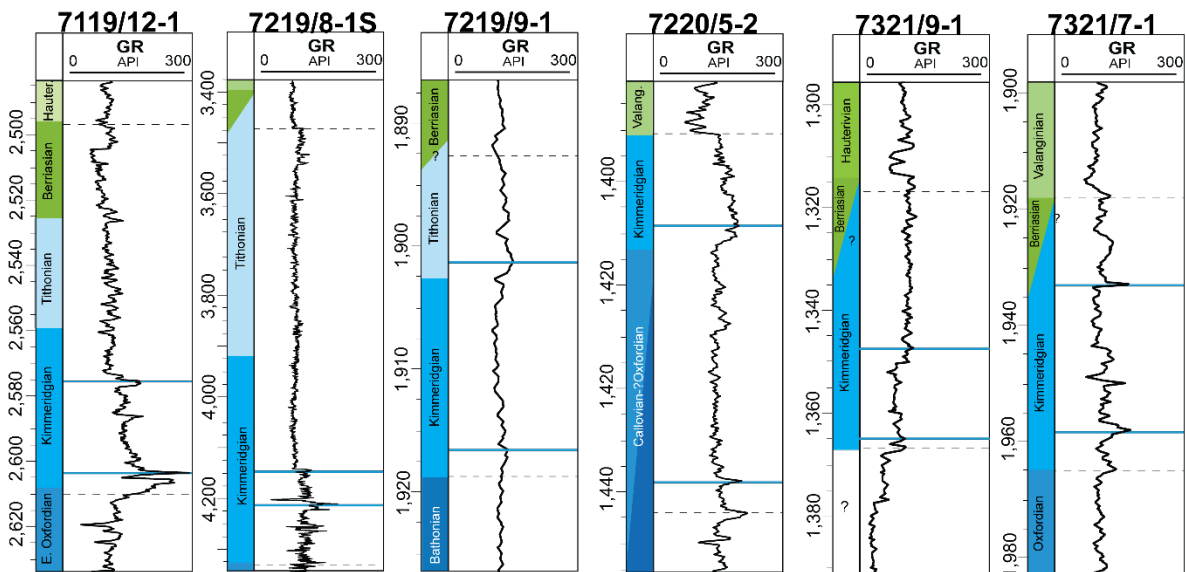


**Fig. 28** The age of the Hekkingen Formation and the MFSs (NPD, 2019). From left to right, the wells are located in the Ringvassøy-Loppa Fault Complex and northward on the western side of the Loppa High. The black dashed lines represent the top and base of the Alge Member and the blue lines show the depth of the MFSs. Vertical scale is in m.

Some of the wells have the MFS3 located close to the top of the Hekkingen Formation, and there is no increase in the gamma-ray values to mark the top of the Alge Member (e.g. 7219/9-1, 7220/5-1 and 7321/9-1; Fig. 28). For these wells, the thickness of the entire Hekkingen Formation was applied in the calculation of the sedimentation rate. The sedimentation rate in the Alge Member displays great variation, varying from 2 m/million years (my) to 56.9 m/my. In most of the wells, the sedimentation rate of the Alge Member is in the range of 4– 9 m/my (Table 12). However, these calculations do not consider erosion and compaction of the succession.

The highest sedimentation rates for the Alge Member are observed in the wells located west and northwest of the Loppa High (i.e. 7219/8-1S, 7321/7-1 and 7321/9-1) and in the Ringvassøy-Loppa Fault Complex (7119/12-1; Table 12). The lowest rates are observed in the Hammerfest Basin (wells 7120/2-2 and 7120/2-3S) and in well 7219/9-1. The latter well is drilled on the tip of one of the rotated fault blocks in the Polhem Subplatform (Fig. 3).

**Table 12** The ages and depths used to calculate the sedimentation rate for the Alge Member (NPD, 2019).

Well	Top Alge (depth (m))	Base Alge (depth (m))	Age base (Ma)	Age top (Ma)	Thickness (m)	Time (my)	Sedimentation rate (m/my)
7119/12-1	2547	2610	157.3	154	36	3.3	10.9
7120/2-2	2638	2656	152.1	148	18	4.1	4.3
7120/2-3S	2000	2018	157.3	153	18	4.3	4.1
7125/1-1	1364	1399	153	148	35	5	7.0
7219/8-1S	4140	4328	157.3	155	188	3.3	56.9
7219/9-1	1893	1919	157.3	145	26	12.7	2.0
7220/5-2	1391	1464	163.5	152.1	73	11.4	6.4
7224/7-1	1364	1399	153	148	35	5	7.0
7226/11-1	1155	1194	160	153	39	7	5.6
7228/9-1S	1046.5	1069	157.3	152	22.5	5	4.5
7321/7-1	1918	1965	157.3	152.1	47	5.6	8.3
7321/9-1	1317	1367	157.3	152.1	50	5.6	8.9

The sedimentation rate makes it possible to calculate the timespan needed to deposit the sediments causing the gamma-ray peak. The vertical thickness of the spikes is used to calculate the timespan (Table 13). In general, the deposition of a prominent spike would take from 100 000 to 500 000 years.

**Table 13** Calculation of the timespan needed to deposit a prominent high-value gamma-ray spike from the thickness of the spike and the sedimentation rate from Table 12. The thicknesses written in brackets represent lower value spikes at the MFSs.

Well	Thickness of MFS2-spike (m)	Deposition time (My)	Thickness of MFS3-spike (m)	Deposition time (My)
7119/12-1	1	0.09	(1.5)	0.14
7120/2-2	-	-	1.5	0.35
7120/2-3S	(1.8)	0.44	5.4	1.3
7125/1-1	2.3	0.32	1.3	0.18
7219/8-1S	-	-	-	-
7219/9-1	-	-	-	-
7220/5-2	0.5	0.08	0.5	0.08
7224/7-1	0.8	0.11	0.9	0.13
7226/11-1	0.9	0.16	1	0.18
7228/9-1S	2.3	0.51	-	-
7321/7-1	0.6	0.07	0.7	0.08
7321/9-1	-	-	-	-

### Interpretation

There is great uncertainty connected to the ages used to calculate the sedimentation rate as the ages are recorded in stages, and as the Hekkingen Formation is marked by an unconformity at the base and additional erosion and compaction is not considered. The calculated sedimentation rates, although being hampered with large uncertainties, suggest relative geographical variation. The highest sedimentation rate is observed in well 7219/8-1S, which also contain the thickest succession of the Alge Member (188 m) suggesting the high sediment input caused subsidence and accumulation space creation in the basin. The wells where the Alge Member is recorded to have the highest sedimentation rates are located in proximity to the Bjørnøyrenna Fault Complex and the Ringvassøy-Loppa Fault Complex, suggesting activity in these fault complexes. The lowest calculated sedimentation rate for the Alge Member in well 7219/9-1, but the well is positioned in the distal part of a wedge and is not representative for the thickness of the Alge Member in that area. The wells in the Hammerfest Basin have the lowest rates, which could reflect that the southernmost part of Loppa High had experienced little or no uplift compared to the western part, and that the Hammerfest Basin was not subsiding during the deposition of the Alge Member.

Table 12 shows the time needed for the formation of the prominent gamma-ray spikes. The time needed range from 100.000 to 500.000 years, suggesting that the high-value spikes can be tied to depositional environments and/or conditions that are homogenous over long periods of time. However, as the compaction of sediments during burial not is considered for the calculations,

it can be assumed that the time needed to deposit the material showing as a high-value spike in the gamma-ray log is less than the calculated time. Regardless, the calculations show that the conditions

## 4.4.2 SEISMIC REFLECTORS & WELL LOGS

### Observations

#### 7119/12-1

In well 7119/12-1, a prominent gamma-ray spike represents the MFS2, while a minor spike represents the MFS3 (Fig. 29). The MFS2 is visible in the density log as a rapid increase followed by a decrease of the density, and the opposite reaction in the sonic log. The MFS2 mark an increase in the seismic amplitude within the formation, shown in the reflector at the base of the Alge Member. The amplitude of the seismic reflectors is higher at the top and base of the Hekkingen Formation. The highest measured TOC-value for the formation is located between the two flooding surfaces and does not seem to affect the well logs. MFS3 does not affect the sonic log but does provoke a slight increase in the sonic log. Both MFSs seem to occur at the same TOC wt. %, at a value around 5.

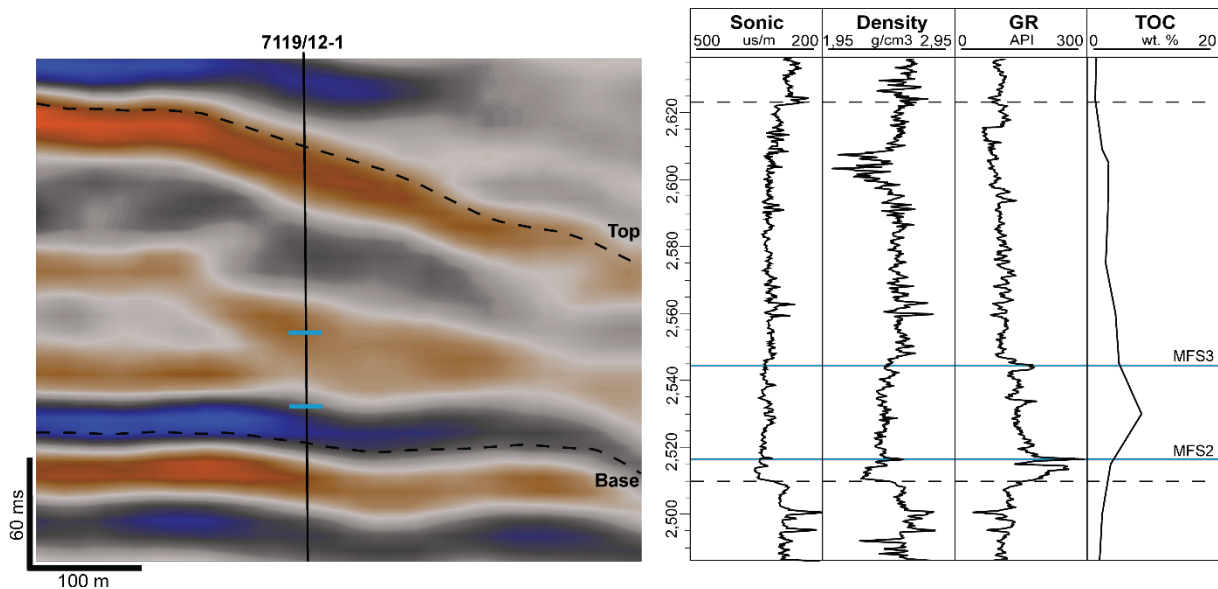


**Fig. 29** Seismic reflectors of the Hekkingen Formation at well 7119/12-1 (top and base are marked with dashed lines) and the MFS's (blue marks and lines) compared to the sonic-, density- and gamma-ray logs together with the measured TOC-data for the entire succession from NPD (2019). Abbreviation GR is used for gamma-ray in the figure.

### 7120/2-2

The well shows prominent gamma-ray values almost throughout the Alge Member and both MFSs are present in the well (Fig. 30). The prominent gamma-ray values in this well correlate to the measured TOC values in the well. The increase in gamma-ray values occurs alongside a decrease in the density-log, while the sonic log is not affected until the base of the Alge Member where also this log decreases rapidly.

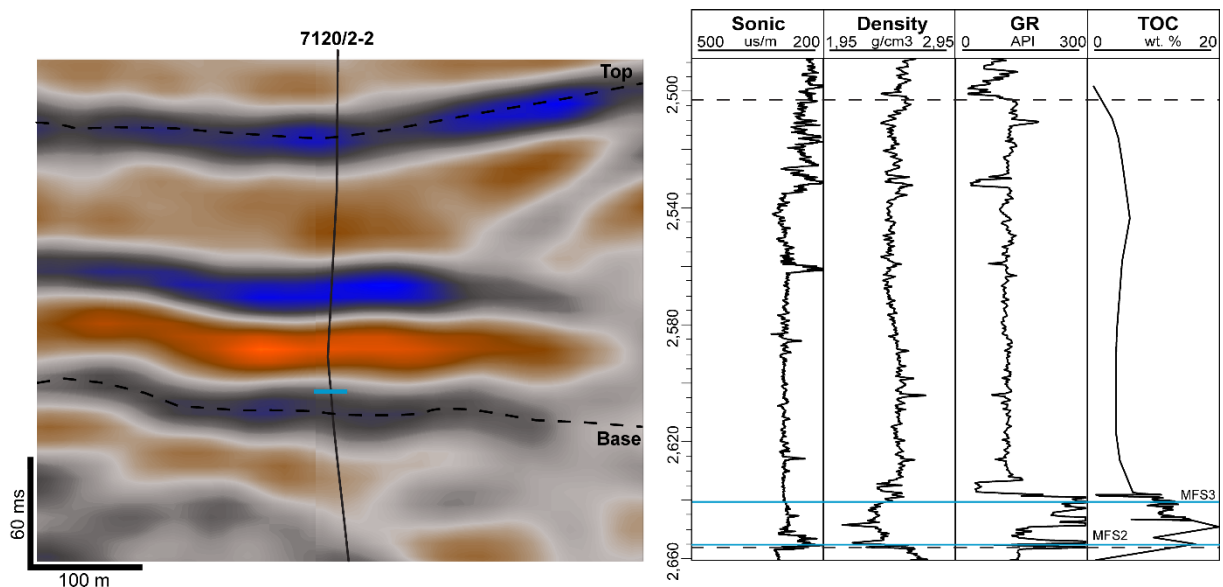


**Fig. 30** Seismic reflectors of the Hekkingen Formation at well 7120/2-2 (top and base are marked with dashed lines) and the MFS's (blue lines) compared to the sonic-, density- and gamma-ray logs together with the measured TOC-data for the entire succession from NPD (2019). Abbreviation: GR= gamma-ray.

### 7120/2-3S (Skalle)

From the Hekkingen Formation in well 7120/2-3S (Fig. 31). The top of the formation is a strong amplitude reflector, while the rest of the succession show an overall low amplitude in the seismic data. The well has an extremely prominent spike in MFS3, whereas the MFS2 shows a minor spike. The increase in gamma-ray values is reflected by an increase in the sonic log and a minor decrease in the density log. The spectral gamma-ray log obtained for this well shows that the uranium is the most dominant radioactive element in the formation, and that the measured uranium is controlling the gamma-ray spikes.

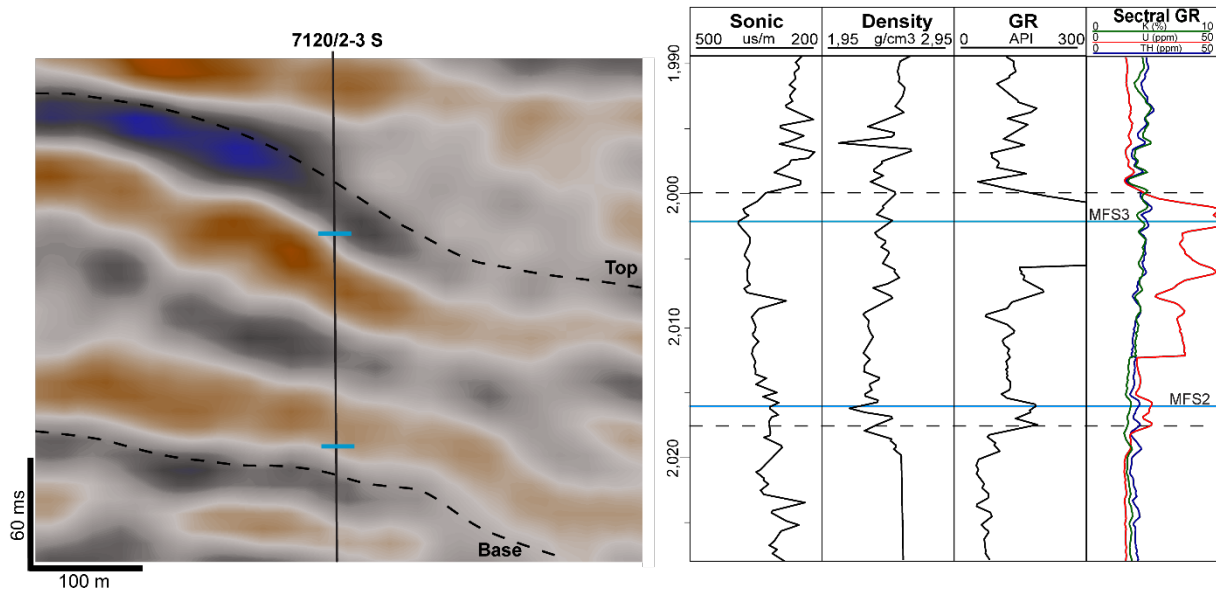


**Fig. 31** Seismic reflectors of the Hekkingen Formation at well 7120/2-3S (top and base are marked with dashed lines) and the MFS's (blue lines) compared to the sonic-, density- and gamma-ray logs together with the measured TOC-data for the entire succession from NPD (2019). Abbreviation: GR= gamma-ray.

### 7125/1-1 (Binne)

In well 7125/1-1 the gamma-ray shows an overall high-value signature, and there is a prominent spike in both MFSs (Fig. 32). TOC and gamma-ray show a good correlation in this well, and the sonic log and the density log increase and decrease respectively in response to gamma-ray signature. The seismic reflectors seem to have the highest amplitude at the top of the formation and for MFS3. The amplitude strength decreases toward the base, not corresponding to the high gamma-ray signature of the high TOC values toward the base of the Alge Member.

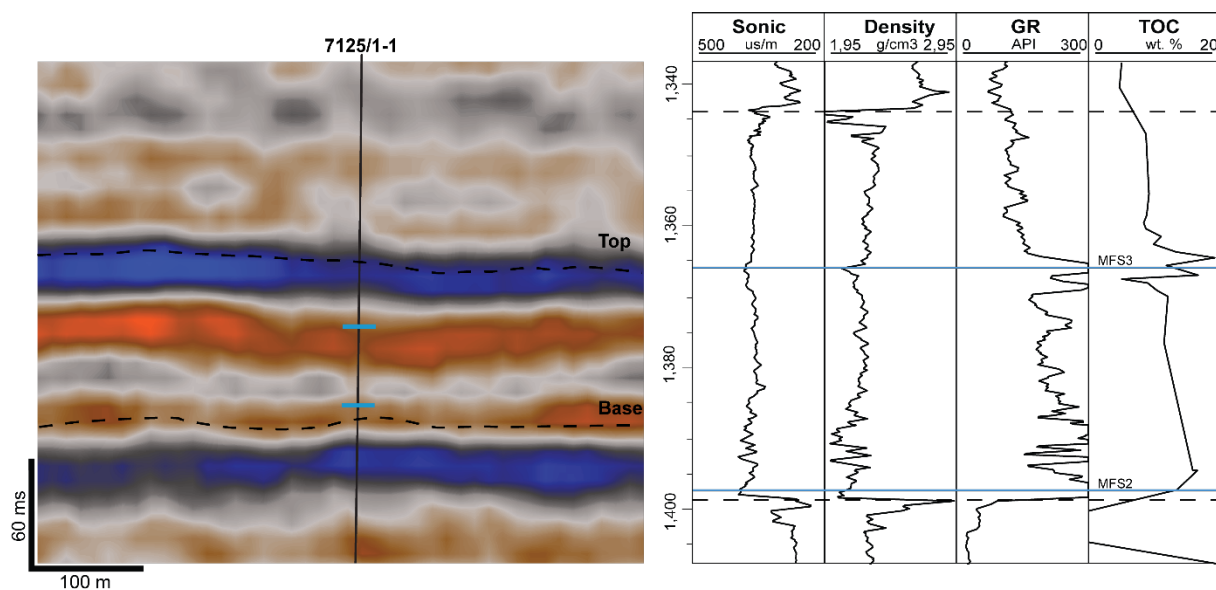


**Fig. 32** Seismic reflectors of the Hekkingen Formation at well 7125/1-1 (top and base are marked with dashed lines) and the MFS's (blue lines) compared to the sonic-, density- and gamma-ray logs together with the measured TOC-data for the entire succession from NPD (2019) Abbreviation: GR= gamma-ray.

### 7219/8-1S

A thick succession representing the Hekkingen FM is present in well 7219/8-1S (Fig. 33). The seismic data shows that there is an increase in the seismic amplitude at the base of the formation, in the Alge Member. At the base, the reflections are parallel and have strong amplitudes, but the strength fades toward the Krill Member consisting of chaotic reflectors with medium to weak amplitude. Well logs and TOC-data correlate the observed changes in the reflectors and amplitude. The Alge Member has a high TOC and a minor increase in the gamma-ray log. The sonic- and density logs, density in particular, mirrors the increase in TOC toward the base.

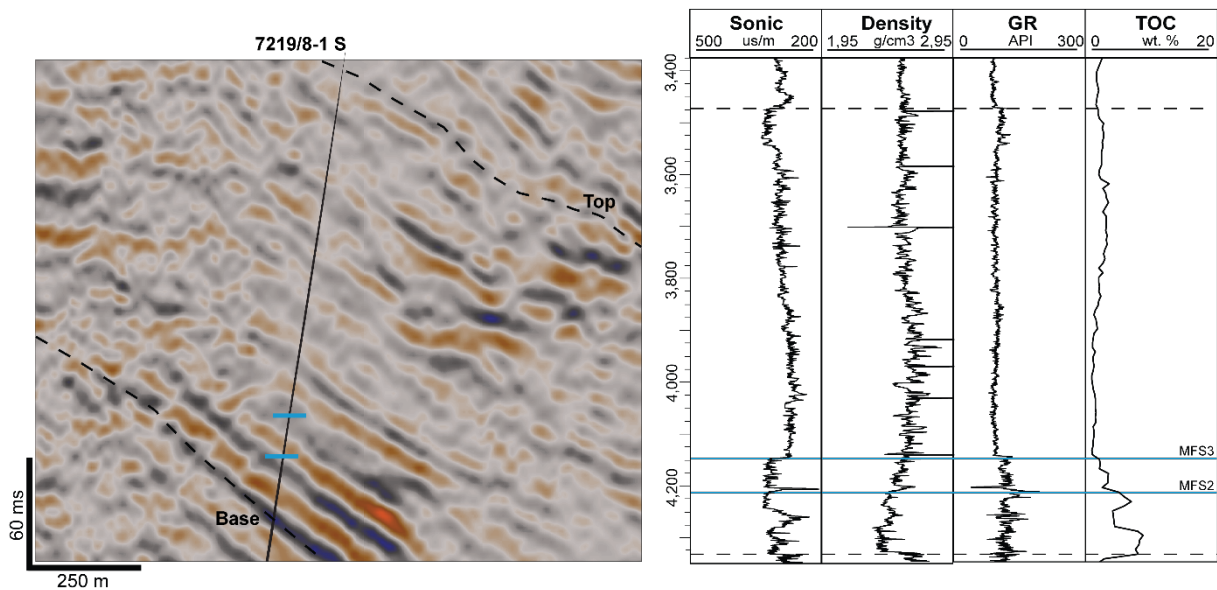


**Fig. 33** Seismic reflectors of the Hekkingen Formation at well 7219/8-1S (top and base are marked with dashed lines) and the MFS's (blue lines) compared to the sonic-, density- and gamma-ray logs together with the measured TOC-data for the entire succession from NPD (2019). Abbreviation: GR= gamma-ray.

### 7220/5-2 (Nunatak)

Nunatak is one of the wells with the overall lowest and uniform gamma-ray signature, and the density- and sonic logs follow the same uniform trend (Fig. 34). MFS2 is marked by a minor spike, while the MFS2 is marked by an overall minor increase in the gamma-ray. The seismic amplitude follows the wells and is low in the entire formation. The spectral gamma-ray display low uranium values, and slightly higher thorium and potassium content. The MFSs are marked by a minor increase in the uranium content.

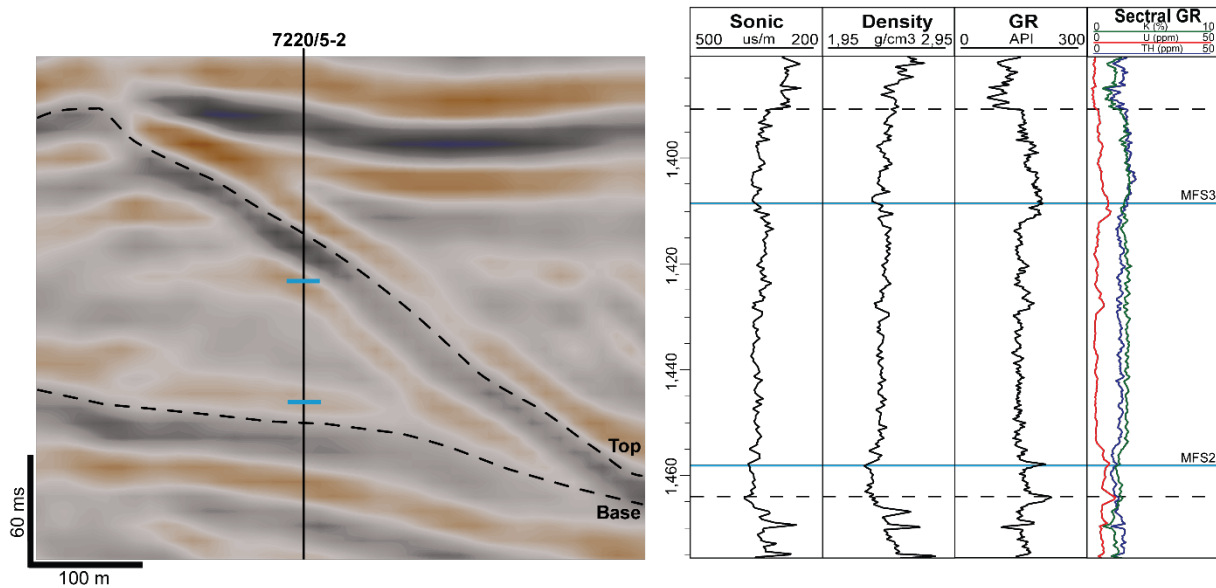


**Fig. 34** Seismic reflectors of the Hekkingen Formation at well 7220/5-2 (top and base are marked with dashed lines) and the MFS's (blue lines) compared to the sonic-, density- and gamma-ray logs together with the measured TOC-data for the entire succession from NPD (2019). Abbreviation: GR= gamma-ray.

### 7324/8-1 (Wisting)

At well 7324/8-1 the formation show a uniform strength in the amplitude in the reflectors representing the formation (Fig. 35). The gamma-ray signature is uniform, with some spikes representing the MFSs. The MFSs can be observed to affect the sonic and density with a minor decrease and increase respectively. The TOC measurements in the well are relatively low for the Hekkingen Formation.

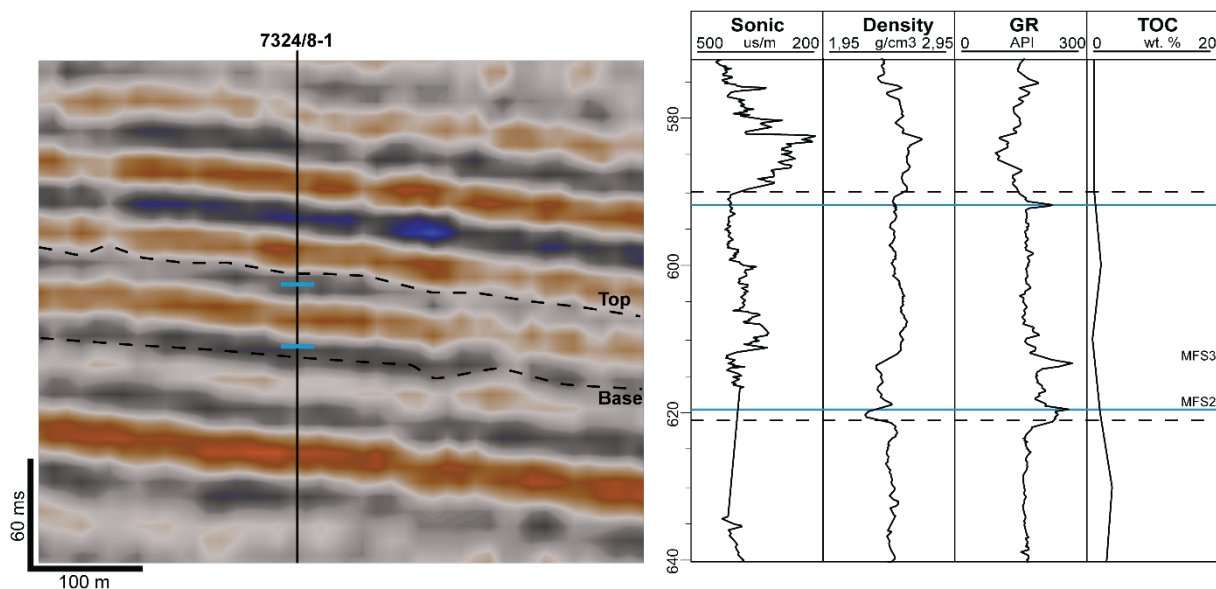


**Fig. 35** Seismic reflectors of the Hekkingen Formation at well 7324/8-1 (top and base are marked with dashed lines) and the MFS's (blue lines) compared to the sonic-, density- and gamma-ray logs together with the measured TOC-data for the entire succession from NPD (2019). Abbreviation: GR= gamma-ray.

## Interpretation

The correlation between the amplitude in the seismic reflection data and the measured TOC in the wells (e.g. 7120/2-2 (Fig. 30), 7125/1-1 (Fig. 32), 7219/8-1S (Fig. 33) and 7324/8-1 (Fig. 35)) indicate that organic-rich layers causes higher amplitude and might be observed on the seismic data. Løseth et al. (2011b) demonstrated that it was possible to observe source rocks, including the Hekkingen Formation, in seismic reflection data. He observed that stronger amplitude in the seismic reflectors implied high content of organic matter, and hence source rocks can be identified. In this study, the highest observed amplitude should be at the base of the Hekkingen Formation, in the Alge Member. This seems to be valid, as generally the Alge Member displays a higher amplitude. The resolution in the seismic data restricts the amount of information possible to extract from the Hekkingen Formation, and the Alge Member is often limited to a few reflectors. In the wells where the amplitude does not match the organic content, the thickness of the organic-rich layer may be below tuning thickness; Løseth et al. (2011b) expected organic-rich source rock intervals below ~20 m to experience amplitude dimming. Moreover, the amplitudes were not scaled or aligned in phase and frequency for the seismic lines displayed in Fig. 29, Fig. 30, Fig. 31, Fig. 32, Fig. 33, Fig. 34 and Fig. 35. For this reason, the strength of the amplitude between the lines cannot be compared. However, the amplitude variations can be used to observe trends within each line.

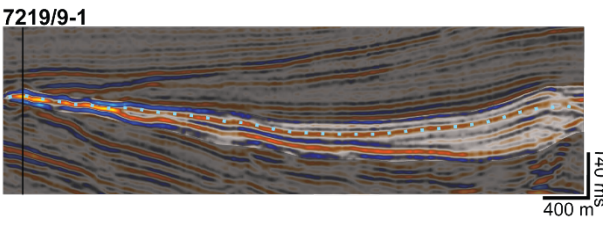
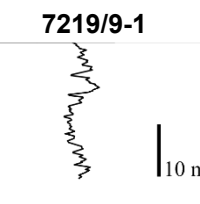
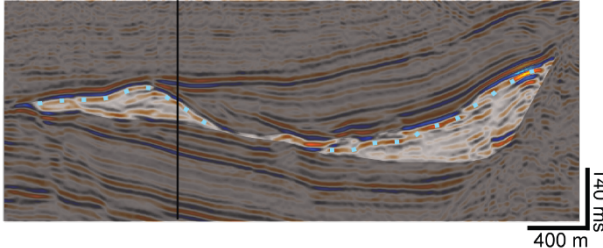
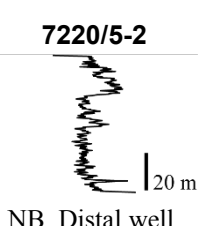
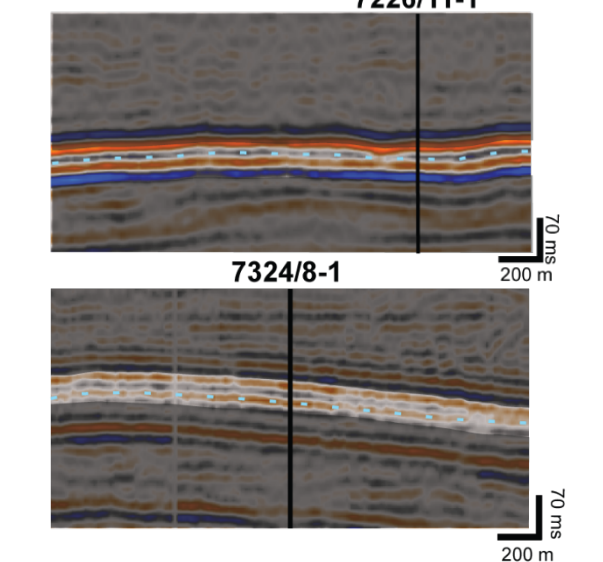
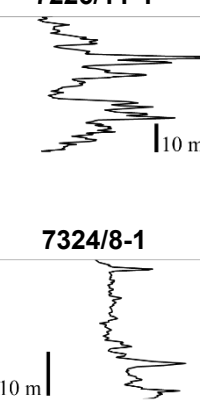
The MFSs seem to have some linkage to the TOC measurements in Alge Member except for well 7324/8-1, but few data points hamper this well. Overall, the TOC has less sampling points than the well logs, meaning that there could be a better correlation of the organic content and well logs than what the TOC log suggests. There are a clear correlation between gamma-ray response and TOC content in the following wells: (e.g. 7120/2-2 (Fig. 30), 7125/1-1 (Binne) (Fig. 32) and 7219/8-1S (Fig. 33)). The MFSs are usually reflected in the sonic and density logs, whereas more obvious in the density log. The increase in TOC at the MFS could cause density changes in the formation. Low TOC measurements in wells with low gamma-ray signature and low amplitude (e.g. Fig. 34) may suggest that the Alge Member consists of a facies variation with less preservation of organic material in this area.

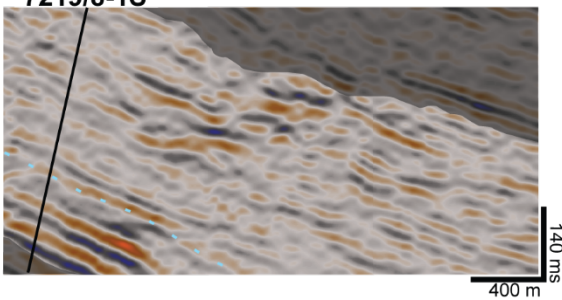
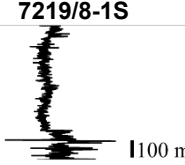
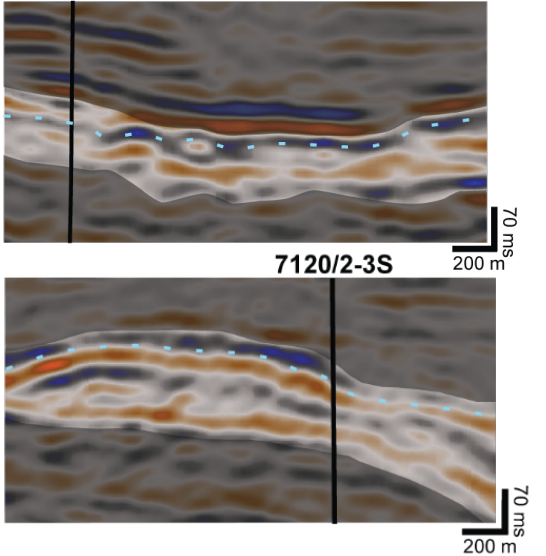
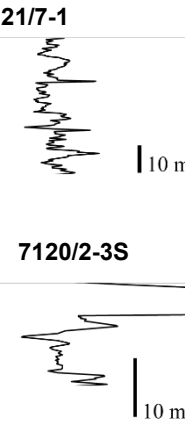
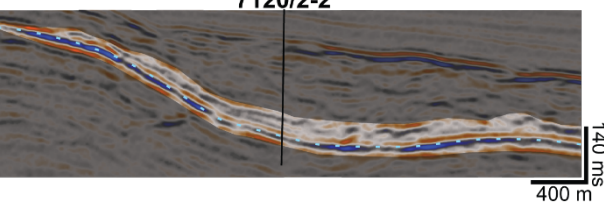
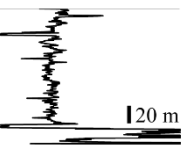
However, there seems to be a correlation between the TOC measurements, the amplitude in the seismic data and higher-value spikes in the gamma-ray log. This suggests there is a connection between the organic content in the Alge Member and the gamma-ray spikes.

### 4.4.3 SEISMIC FACIES

Six seismic facies were identified in the Hekkingen Formation around the wells in the study and are summarized in Table 14.

**Table 14** Summary of the seismic facies identified around the studies wells. The highlighted areas represent the entire Hekkingen Formation, the dashed blue line represent top Alge Member.

Facies description	Interpretation	Example	GR pattern 0 150 300
<p><b>A1</b> Wedge, internal high amplitude reflectors, continuous. Aggrading, downlapping reflectors.</p> <p><b>Well:</b> 7219/9-1</p>	<p>Syn-rift deposited wedge in rotated fault block. The increase in prograding reflectors toward the top of the formation indicate less fault activity at the base than toward the top.</p>		 <p>NB. Distal well.</p>
<p><b>A2</b> Wedge, internal weak amplitude, chaotic to subparallel, aggrading reflectors</p> <p><b>Well:</b> 7220/5-2</p>	<p>Syn-rift deposited wedge in rotated fault block. The chaotic and prograding reflectors indicate high fault activity throughout the deposition of the formation.</p>		 <p>NB. Distal well.</p>
<p><b>B</b> Uniform parallel reflectors with high continuity, high to medium amplitude</p> <p><b>Wells:</b> 7125/1-1 7226/11-1 7321/9-1 7324/8-1 7224/7-1 7228/9-1S</p>	<p>A depositional regime with low sediment input and low energy.</p>		

Facies description	Interpretation	Example	GR pattern 0 150 300
<p><b>C</b> Internal clinoforms with weak amplitude in the Krill Member. Parallel reflectors, strong amplitude at base in Alge Member.</p> <p><b>Wells:</b> 7219/8-1S</p>	<p>High sediment input to basin due to syn-rift deposition. The continuous reflectors at the base indicate that the Alge Member experienced a lower energy environment than the Krill Member.</p>		
<p><b>D</b> Deformation structures in the form of breaks in the reflectors. Medium amplitude.</p> <p><b>Wells:</b> 7119/12-1 7321/7-1 7321/7-1 7120/2-3S</p>	<p>Thin-skinned gravitational gliding structures. Listric faults in the fine-grained and organic-rich strata. Alternatively, the breaks in the reflectors could represent sand injectities.</p>		
<p><b>E</b> The Alge Member displays parallel reflectors, high amplitude and onlap. Subparallel, medium amplitude, bidirectional onlap on the Krill Member</p> <p><b>Well:</b> 7120/2-2</p>	<p>Reflectors onlap toward the anticline formed in the hanging wall of the Asterias Fault Complex, indicate activity in Asterias Fault Complex during deposition of the Alge Member. The Krill Member seems to represent the distal parts of a lobe or fan.</p>		

## **Facies A**

### ***Description***

Wedges were only observed in rotated fault blocks of the Bjørnøyrenna Fault Complex in the Polhem Subplatform and are subdivided into A1 and A2 based on internal configuration. A1 has internal strong and continuous reflectors. Aggradational reflectors are present in the wedge. A2 was characterized by internal chaotic and aggrading reflectors (Table 14). The gamma-ray shows low values in the wedges.

### ***Interpretation***

The location of the wedges indicates that the Bjørnøyrenna Fault Complex was active during the time of deposition of the Alge Member (Fig. 6). A1 was interpreted as a syn-rift deposited wedge in rotated fault block. The increase in the aggradational character of the reflectors toward the top of the Hekkingen Formation indicates that the fault activity has increased during deposition of the Alge Member. A2 was interpreted as syn-rift deposition as well; however, the chaotic and prograding reflectors indicate an overall higher fault activity throughout the deposition of the Alge Member. The wells drilled in the wedges display the distal parts of the wedge; therefore, the well log is not representative for the entire succession (Table 14).

## **Facies B**

### ***Description***

Uniform and parallel reflectors with high continuity around the wells where the facies was observed. The reflectors display a high to medium amplitude. The well logs display high gamma-ray values and an erratic signature when the seismic data displays a high amplitude, while it displays low to medium-value spikes when the seismic reflectors display a low amplitude.

### ***Interpretation***

Continuous parallel reflectors over large areas indicate a uniform low energy on the shelf at the time of deposition of pelagic sediments. High amplitude reflections suggest a high content of organic matter, further implying anoxic conditions during deposition (Løseth et al., 2011b). Medium amplitude suggests less organic matter, or layers of organic matter below tuning thickness causing dimming of the amplitude strength (Løseth et al., 2011b).

## **Facies C**

### ***Description***

Facies C is characterized by internal clinofolds in the Krill Member, while being continuous and parallel toward the base, within the Alge Member. The reflectors display a higher amplitude

at the base. The gamma-ray log display an increase in value toward the base of the Hekking Formation, in the Alge Member (Table 14, C).

### ***Interpretation***

The clinoforms observed in Facies C indicate high sediment supply, into the basin. This is supported by the thick succession of the Hekkingen Formation deposited at this location (Fig. 9). The parallel and continuous reflectors in the Alge Member indicate low energy deposition, and the high amplitude may imply organic content (Løseth et al., 2011b). The thickness of the Krill Member and the clinoforms within this member indicate that the tectonic activity initiated during, or prior to the deposition of the Alge Member, and continuously increased during the deposition of Hekkingen Formation. The location of the well and direction of the clinoforms suggest tectonic activity the Bjørnøyrenna Fault Complex.

## **Facies D**

### ***Description***

Deformation structures where reflectors with medium amplitude show minor breaks and irregularity. The reflectors above appear parallel and continuous. The gamma-ray logs of the facies variate and both low-value signatures and prominent spikes can be observed within the seismic facies (Table 14).

### ***Interpretation***

Facies D was interpreted as thin-skinned gravitational gliding structures based on Løseth et al. (2011a). The irregularity observed in the reflectors is interpreted as small listric faults, which sole out at the base of an organic-rich zone, which caused the upper part to rotate. Løseth et al. (2011a) states these structures often develop in restricted locations, and form in the sediments at a few hundred meters of burial. As an alternative explanation, the breaks in the reflectors could be the occurrence of sand injectites from the underlying Stø Formation (Fig. 8). Sand injectites are triggered by fracturing of an impermeable layer where the pressure difference triggers an upward fluid flow, causing an injection of the underlying sediments into the fractures (Hurst et al., 2011). The distribution of the facies shows that the wells are located close to the active fault complexes around the Loppa High (Fig. 36). The tectonic activity could cause both gravitational gliding and sand injectites; however, the sand injectites need to be above the seismic resolution. The variation in the gamma-ray signature for the seismic facies might be explained by the lateral variation within the facies, from areas distorted by the deformation to the less affected surrounding.

## **Facies E**

### ***Description***

Facies E onlap on the Loppa High in the Alge Member. The reflector representing the Alge Member has a high amplitude and is parallel. In the Krill Member, the reflectors display directional onlap and subparallel reflectors with weaker amplitude.

### ***Interpretation***

The reflector onlapping on the Loppa High suggests that the Asterias Fault Complex was active during the deposition of the Alge Member. The continuous and parallel reflector indicates a low energy environment and the high amplitude suggests there was deposition of organic matter (Løseth et al., 2011b). This suggests that the activity in the Asterias Fault Complex was low. The reflectors of the Krill Member show bidirectional onlap and are interpreted to the distal part of a lobe or a fan, suggesting an increase in tectonic activity and sediment supply. The tectonic activity in the Asterias Fault Complex seems to increase during the deposition of the Hekkingen Formation.

### **Regional interpretation**

Wedges and clinoforms observed on the western side of the Loppa High suggest that the Bjørnøyrenna Fault Complex was active. Consequently, the uplift of parts of the Loppa High took place during the deposition of the Hekkingen Formation. The distribution of the seismic facies in the study area shows that the observed wedges, the high-energy sediment input (clinoforms) and the onlap are all concentrated around the Loppa High. Thus, the uplift of the high seems to be caused mainly by tectonic activity during deposition (Fig. 36). A low energy to restricted anoxic deposition of the Hekkingen Formation is interpreted for the remaining wells in the study area. The distribution of the deformation structures is concentrated around the Loppa High and to the Ringvassøy-Loppa Fault Complex, which suggests that the tectonic activity in this area has triggered the deformation structures, and the organic content in the formation acted as a detachment zone for the faults.

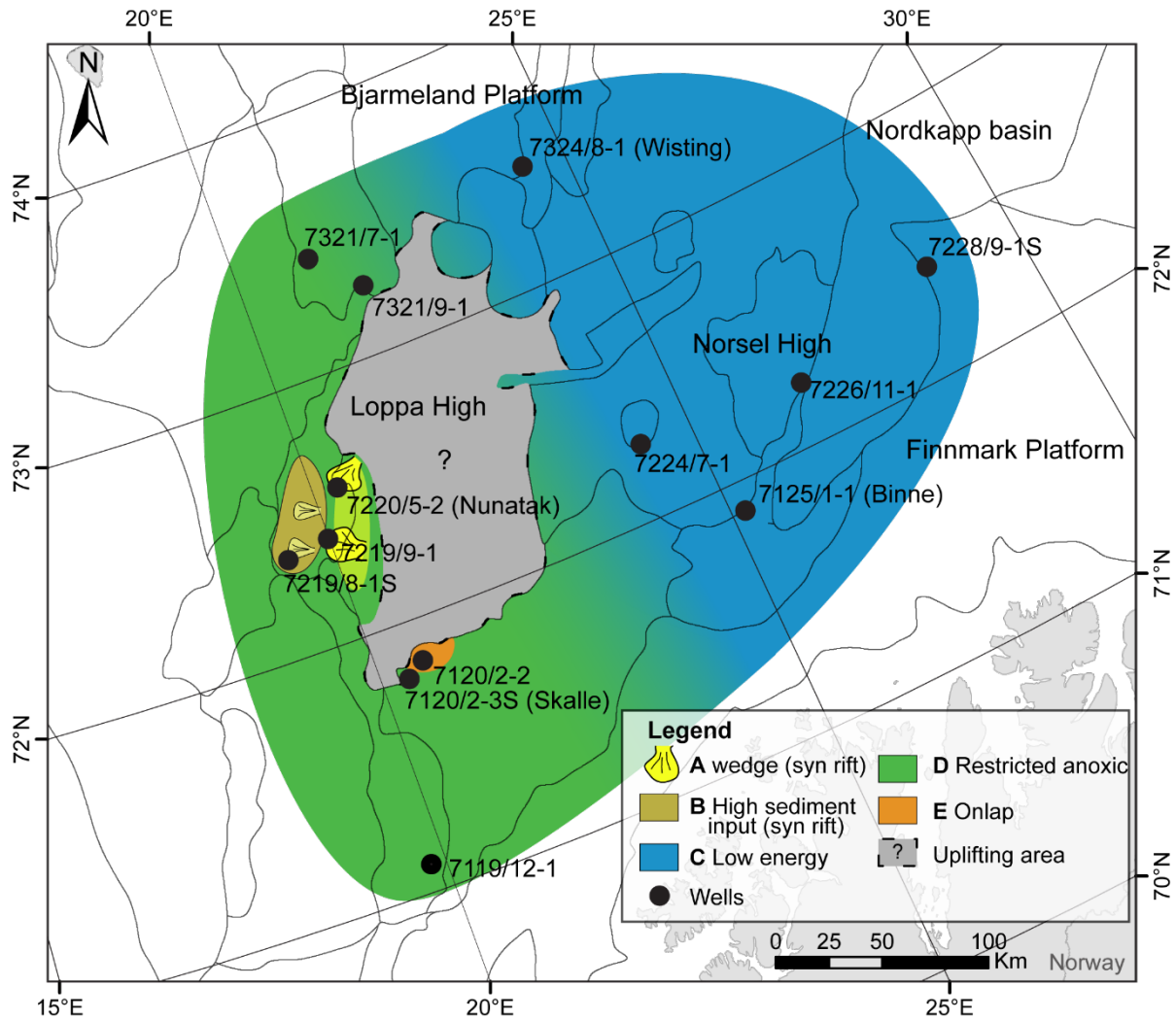


**Fig. 36** Distribution of the seismic facies in the study area. The wells surrounding the Nordkapp Basin, and northwards to well 7324/8-1 (Wisting) in the Hoop Fault Complex, all display low energy deposition. The seismic facies in the wells closest to the Loppa High, show sign of tectonic activity in the fault complexes and the high sediment input to well 7219/8-1S in the Bjørnøyrenna Fault Complex could be explained by erosion of a subaerial exposed island. The tectonic activity is likely to have caused the deformation structures observed in the Ringvassøy-Loppa Fault Complex, the Hammerfest Basin and in the Fingerdjupet Sub-basin (7321/7-1). The current configuration of the Loppa High is marked grey on the map as the amount of uplift the area had experienced during the deposition of the Hekkingen Formation is unknown.

#### 4.4.4 GAMMA-RAY SIGNATURE

##### Observations

A low gamma-ray value signature is observed in the wells west of the Loppa High, while the wells in the Ringvassøy-Loppa Fault Complex, the Hammerfest Basin and close to the Nordkapp Basin display prominent spikes and often an erratic signature (Table 15; Fig. 37). The erratic pattern was observed in the wells where there is a high-value prominent spike representing both MFSs (Fig. 37). In well 7120/2-2, the Alge Member was observed to have high-value prominent spikes in both MFSs (Fig. 37), thus changing the previous definition by Marín (personal communication, October 2018) where the Alge Member only had one prominent gamma-ray spike in MFS2 (Fig. 4). The categories almost correspond to the former division of the spikes, whereas well 7120/2-2 was redefined to have a prominent spike present in both MFS and not just MFS2 (Marín, personal communication, October 2018; Fig. 4).

**Table 15** The different gamma-ray signature observed in the wells. The signature follows the prominent spike observed in the gamma-ray log.

Well	Overall low values	High around one MFS	Erratic
7119/12-1		X	
7120/2-2			X
7120/2-3S		X	
7125/1-1			X
7219/8-1S	X		
7219/9-1	X		
7220/5-2	X		
7224/7-1			X
7226/11-1		X	
7228/9-1S		X	
7321/7-1	X		
7321/9-1	X		
7324/8-1	X		

##### Interpretation

The correlation between the high-value spikes in both MFS and the high-value erratic gamma-ray signature, indicates that the cause of the high gamma-ray values is present throughout the deposition of the Alge Member. Moreover, the location of the wells with erratic signature indicates that the area southeast of the Loppa High was favorable for the deposition of material triggering high gamma-ray readings.

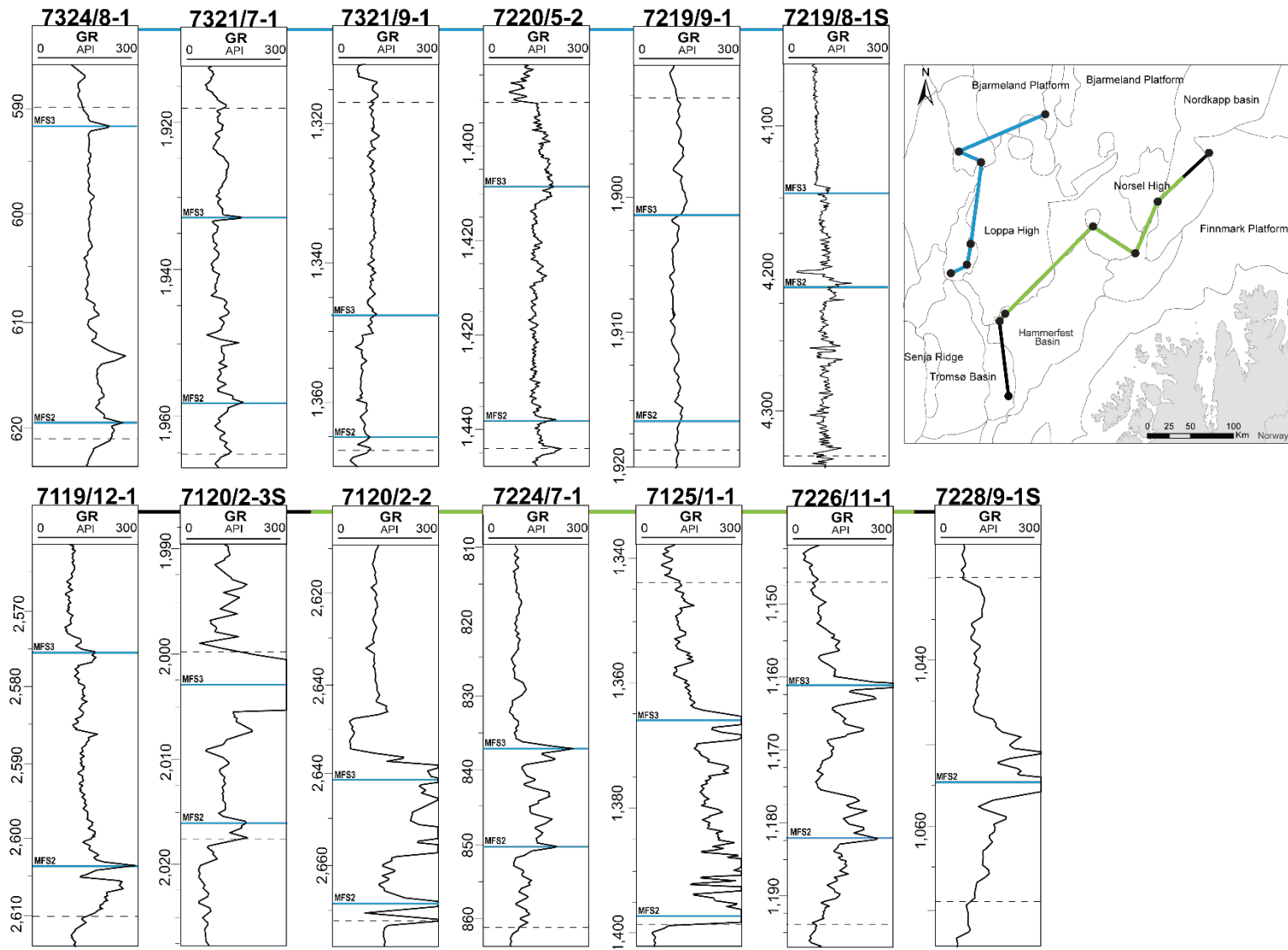


**Fig. 37** The gamma-ray signature of the wells in the study. The top row (blue line on map) exhibit an overall low gamma-ray signature, corresponding to the wells with no prominent spikes. The lowest row contains the wells with high gamma-ray values only around one MFS (black line on map) and the erratic signature between the MFSs in the middle (green line on map). The dashed lines represent top and base of the Hekkingen Formation

#### **4.4.5 SPECTRAL GAMMA-RAY LOG**

##### **Observations**

Comparison of the spectral gamma-ray log and the spikes in the gamma-ray log display a correlation between the prominent high-value gamma-ray spikes and the uranium content (Fig. 38). Well 7220/5-2 has no prominent spikes and display low-value reading in the spectral gamma-ray log for the uranium, the potassium and the thorium content (Fig. 38). Wells 7220/10-1 and 7120/6-3S both display higher-value readings of the potassium and thorium content than for the uranium content (Fig. 38), and in well 7120/6-3S the slightly higher readings of the thorium and potassium cause higher-value readings in the gamma-ray log. However, both in well 7220/10-1 and in well 7120/6-3S the higher value spikes in the gamma-ray log is only present when there is an increase in the uranium content in the succession (Fig. 38). The same pattern can be observed in wells 7120/2-3S, 7121/9-1 and 7123/4-1A, which all display high-value prominent spikes in the gamma-ray log (Fig. 38). Wells 7121/9-1 and 7123/4-1A show no readings for potassium in the spectral gamma-ray log, but both have an overall erratic high-value signature and the spikes in the gamma-ray log correspond to higher-value uranium readings in the spectral gamma-ray log (Fig. 38). Thus, it seems that the potassium and thorium content increases the value in the gamma-ray log, but these two elements do not create the same high-value spikes as an increase in the uranium content does. High values of all three will cause a higher reading in the gamma-ray log, than uranium alone (e.g. well 7220/5-2 show small changes in the gamma-ray log when the uranium content varies, whereas in well 7120/6-3S the smallest change in the uranium causes high-value spikes in the gamma-ray log (Fig. 38).

##### **Interpretation**

The correlation between the uranium content and the high-value prominent spikes and high-value erratic gamma-ray signature observed in the gamma-ray log indicate that the uranium content is a controlling factor for the development of the spikes (Fig. 38). The lack of spikes corresponding to the potassium and/or thorium content indicates that even though these elements cause overall higher readings in the gamma-ray log, they do not cause high-value spikes in the gamma-ray log.

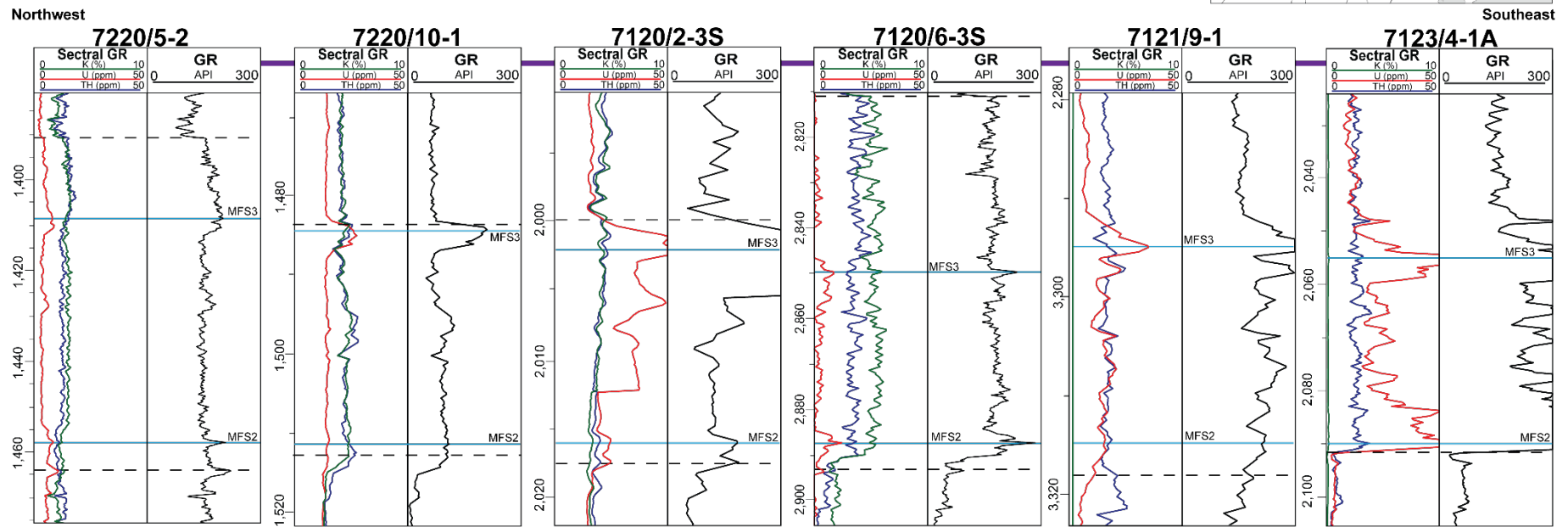
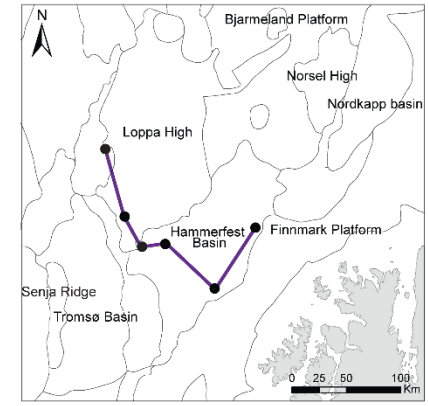


**Fig. 38** Comparison of the spectral gamma-ray log and the prominent spikes. Note the correlation between increase in the uranium content and the prominent high value gamma-ray spikes.

## 4.5 Core logs – Facies and depositional environment

The core logging focused on the Hekkingen Formation, and the described cores are all in the Alge Member or in the transition between the Alge and Krill members. The cored intervals from 7120/2-2, 7120/2-3S and 7125/1-1 contain the MFS3, while 7219/8-1S and 7228/9-1S contain neither MFS2 nor MFS3. Seven different lithofacies (F) were recognized (Fig. 39; Table 16) and divided into two facies associations (FA) (Table 17), reflecting the depositional elements and depositional environment.

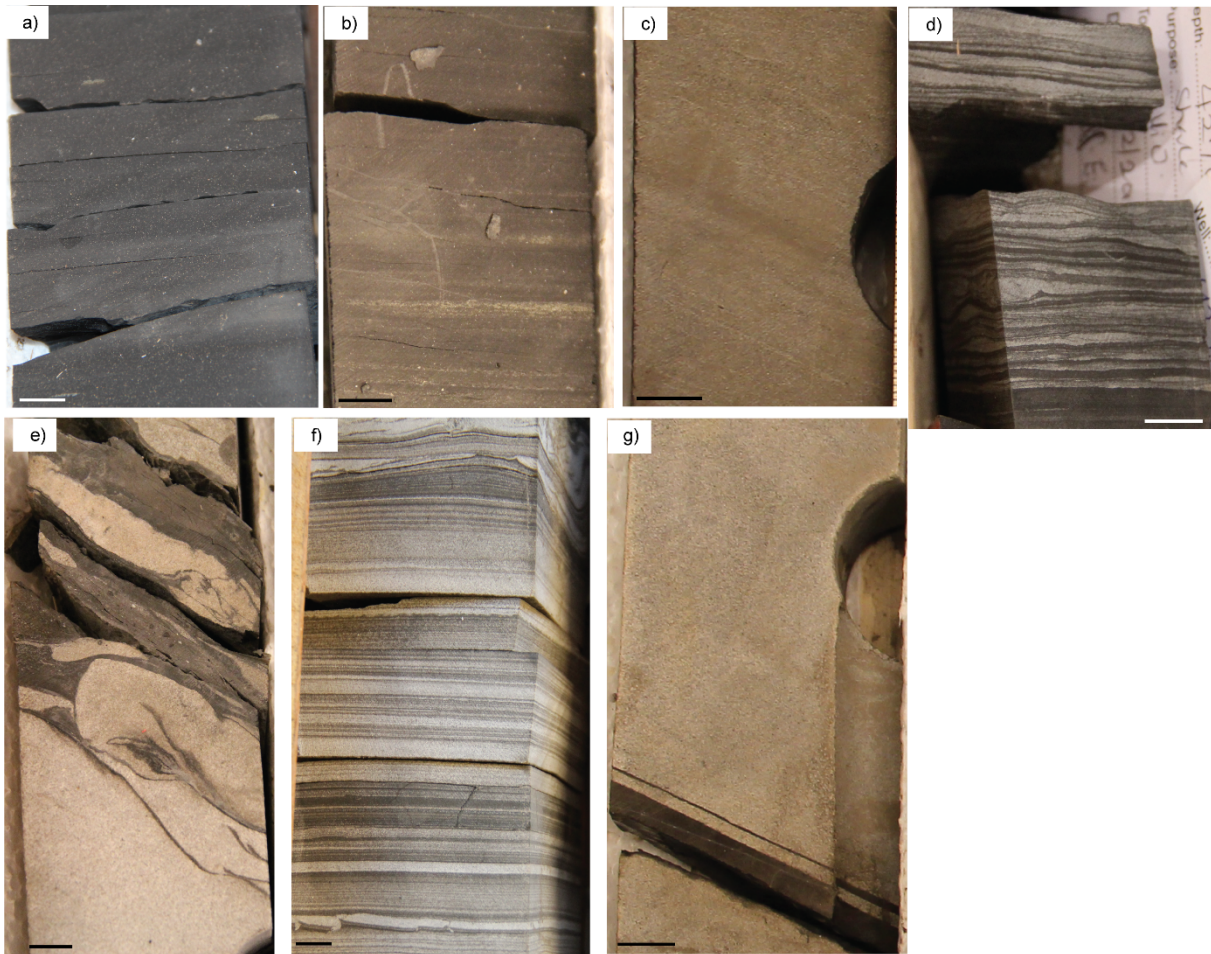


**Fig. 39** Core photos of the identified lithofacies in the wells. a) Black shale (7125/1-1 at the depth of 1362.00 m), b) parallel laminated mudstone (7120/2-2 at the depth of 2009.80 m), c) siltstone (7120/2-3S at the depth of 2017.30 m), d) interbedded sandstone and siltstone (7219/8-1S at the depth of 4270.22 m), e) soft sediment deformation (7120/2-3S at the depth of 2003.30 m), f) parallel laminated sandstone (7120/2-2 at the depth of 2637.10 m), and g) massive sandstone (7120/2-3S at the depth of 2018.30 m). All listed depths represent the depth at the top at the top of the photos. Photo e) display pygmatic folding observed in 7120/2-3S, while the neighbouring, well 7120/2-2 in photo f) display a layer of flame structures toward the base of the photo. Flame structures can also be observed in d) in the middle of the lower core piece. In photo, g) the sharp and erosive boundaries between the mudstone and the sandstone in well 7120/2-3S can be observed. The line in the left lower corner of the photos represent 1 cm on the photos.

**Table 16** The interpreted facies from the viewed core logs.

<b>Facies</b>	<b>Lithology</b>	<b>Sedimentary structures</b>	<b>Body fossils &amp; trace fossils</b>	<b>Interpretation</b>
<b>F1:</b> <i>Black shale</i>	Dark grey with a green tint to dark black mudstone. Flaky to fissile. Pyrite nodules and carbonate-filled fractures occur.	Parallel lamination	None	Fallout from suspension in low energy, anoxic environment.
<b>F2:</b> <i>Parallel laminated mudstone</i>	Dark brown to black mudstone. Blocky to sub-fissile. Pyrite nodules/lenses and carbonate filled fractures occur.	Silty- and pyrite lined lamina	Shell fragments, corals, bivalves, and minor bioturbation. Occasional coal fragments or layers. Fossilized wood is rare.	Fallout from suspension in low energy, dysoxic to anoxic environment.
<b>F3:</b> <i>Siltstone</i>	Pale grey to dark brownish grey siltstone. Blocky. Homogenous.	None	None	Fallout from suspension in low energy environment.
<b>F4:</b> <i>Interbedded sandstone and siltstone.</i>	White to pale grey, interbedded in black mudstone.	Asymmetric ripples and flaser bedding	None	Current ripples and flaser bedding indicate varying energy in depositional environment, e.g. low-density turbidity flow or distal storm deposits.
<b>F5:</b> <i>Soft sediment deformed sandstone</i>	Pale grey sandstone. Coal- and glauconite clasts occur.	Sand injectites, soft sediment deformation, flame structures, convolute bedding and rip-up clasts	None	Rapid deposition of sediments. Fluid migration from underlying sediments has caused the deformation.
<b>F6:</b> <i>Parallel laminated sandstone</i>	White to pale grey sandstone. Dark mudstone and siltstone lamina.	Siltstone lamina of <1 mm to 0.8 mm. Soft sediment deformation in the form of flame structures occur	None	Suspension settling of low-density turbidity flow-structures and lamination could indicate variation sediment supply
<b>F7:</b> <i>Massive sandstone</i>	White to pale grey sandstone. Homogenous. Upper boundary often erosive.	Erosive upper boundary	None	Reworked sediments, deposited below wave-base in low energy environment.

**Table 17** The facies association derived from the interpreted facies and the wells where the different facies and facies associations are observed.

<i>Facies Associations</i>	<i>Facies</i>	<i>Wells</i>
<i>FA1:</i> <i>Restricted anoxic</i>	F1–F3, F5, F7	7120/2-2, 7120/2-3S, 7125/1-1, 7219/8-1S, 7228/9-1S
<i>FA2:</i> <i>Turbidity current</i> <i>(gravity flow deposits)</i>	F4–F6	7120/2-2, 7219/8-1S

#### 4.5.1 FACIES ASSOCIATIONS

##### **FA1: Restricted anoxic**

The restricted anoxic FA consists of lithofacies F1–F3, F5 and F7, black shale, parallel laminated mudstone, siltstone, soft sediment deformed sandstone and massive sandstone (Table 17).

##### **Description**

The FA1 is mainly composed of F1 (Fig. 39), consisting of green tinted dark grey or black organic-rich mudstone. The mudstone is flaky and fissile to blocky but is mainly homogeneous with no sedimentary structures. Pyrite is present in the form of nodules or framboids, but euhedral crystals and lenses also occur (Fig. 41). The pyrite framboids, crystals and lenses are observed in a size range from 3 to 50 mm, where the larger crystals display zonation. Carbonate filled fractures with random orientation are common, and carbonate nodules can be observed. Within the homogeneous dark mudstone of F1, F2 is observed as areas with silty or pyrite lined lamina (Fig. 39). The mudstone in the facies has a dark brown to black colour, with a green tint. The fossil record in this FA is scarce but with relatively intact specimens of solitary corals, bivalves (found both solidary and in layers) and ammonites, as well as unidentifiable broken shell fragments occur in F2. The fossils are often replaced by pyrite (Fig. 40). Less than 10 mm large coal fragments, and 2 to 10 mm thick coal layers are common. Wells 7120/2-3S and 7120/2-2 contain fossilized pieces of terrestrial plants (Fig. 40). Dark brown siltstone beds with a thickness of 15 to 50 mm that occur within the mudstone, represent F3 (Fig. 39). A sharp and occasional erosive contact was present between the siltstone and the surrounding mudstone. In addition, the FA contains layers of sandstone throughout the interval in the Alge Member in well 7120/2-3S, defined as F4 (Fig. 39; Table 16). The sandstone appeared homogenous, with very fine to medium grain size and a white to pale grey colour. The layers, 5 to 35 cm thick, are observed with the same orientation as the occasional lamina in the mudstone, with sharp or lightly eroded contacts at top and base (F7; Fig. 41). These often display carbonate filled

fractured. The sandstone is also present as smaller bodies with random orientation within the mudstone, often displaying ptigmatic folding (F5, Fig. 41). Some of the larger bodies contain ~cm thick layers of interbedded mud with convolute bedding. The sandstone commonly contains some mud clasts (Fig. 41).

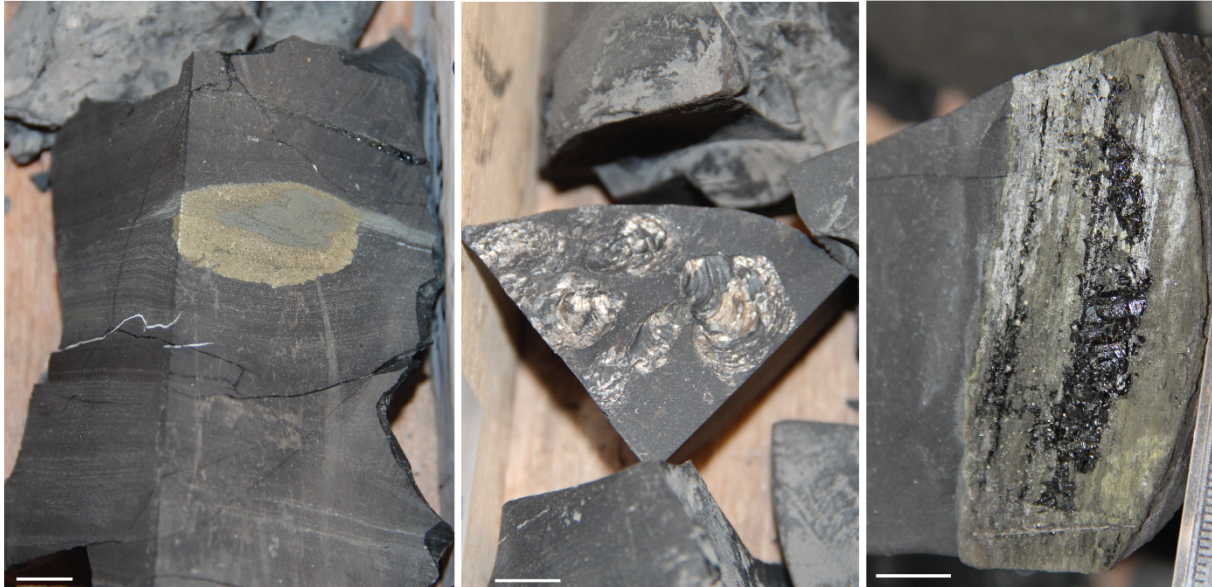


**Fig. 40** Left photo: A lense shaped pyrite nodule exhibiting zonation from well 7120/2-2, depth 2640.50. Middle photo: The bivalve fossils observed in well 7120/2-2–2642.50 show that pyrite has acted as a replacement mineral in the fossilized shell. Right photo: Woody material from well 7120/2-2, depth. The white line the left lower corner of the photos represents 1 cm.

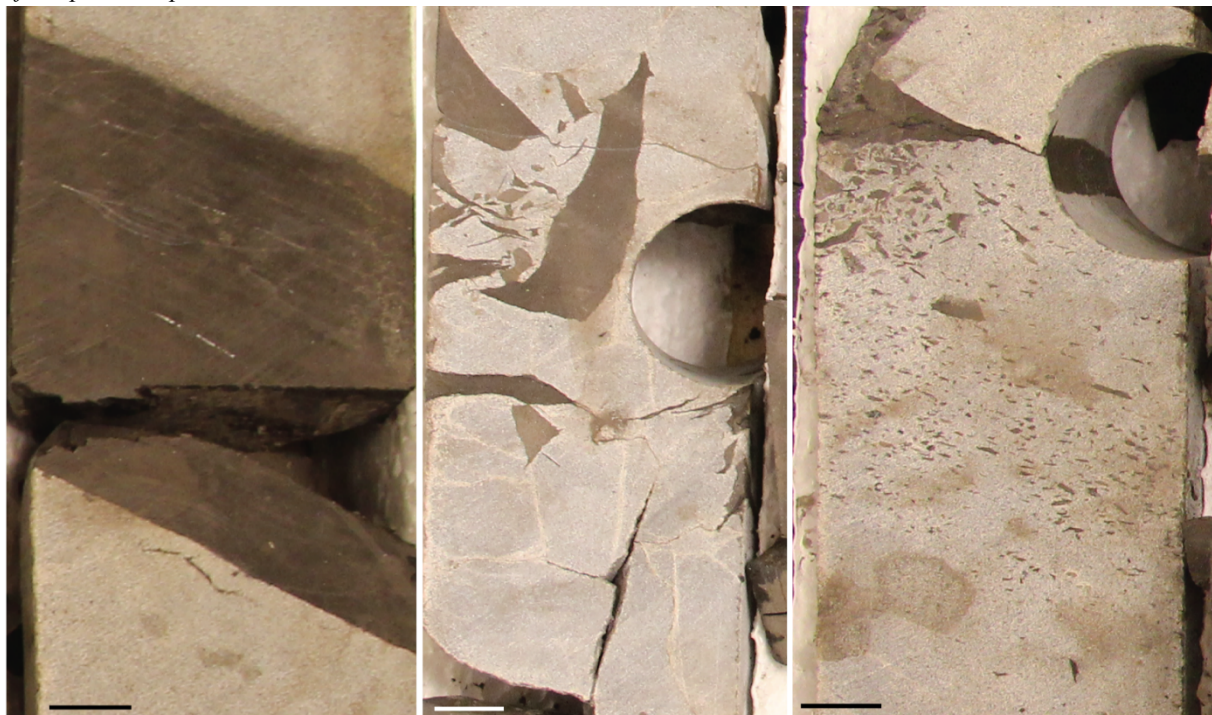


**Fig. 41** The sandstone interpreted as sand injectites observed in well 7120/2-3S. Left: the base of the upper sandstone package display a lightly eroded base, while the top of the lower sandstone package have a sharp boundary to the overlying mudstone. Middle: Random orientation of the sandstone within the mudstone, and mud clasts is also present within the sand package. Right: Several mudclasts present within the sandstone and the sandpackage displays an erosive top. The line the left lower corner of the photos represents 1 cm.

The FA1 in wells 7120/2-3S, 7125/1-1 and 7228/9-1 show some variation within in composition (Fig. 42; Fig. 43). The viewed succession of the Alge Member from wells 7120/2-3S and 7125/1-1 contain a higher abundance of pyrite and visible organic material, whereas in the core from well 7228/9-1 only a few pyrite nodules are present. However, more fossils were observed in the Alge Member in the cores from well 7125/1-1 and 7228/9-1 than in 7120/2-3S where no fossils were observed. The viewed cores from wells 7120/2-3S and 7125/1-1 both contain the depth of the MFS3. However, none of the observations from the cores correlates with the gamma-ray log (Fig. 42; Fig. 43).

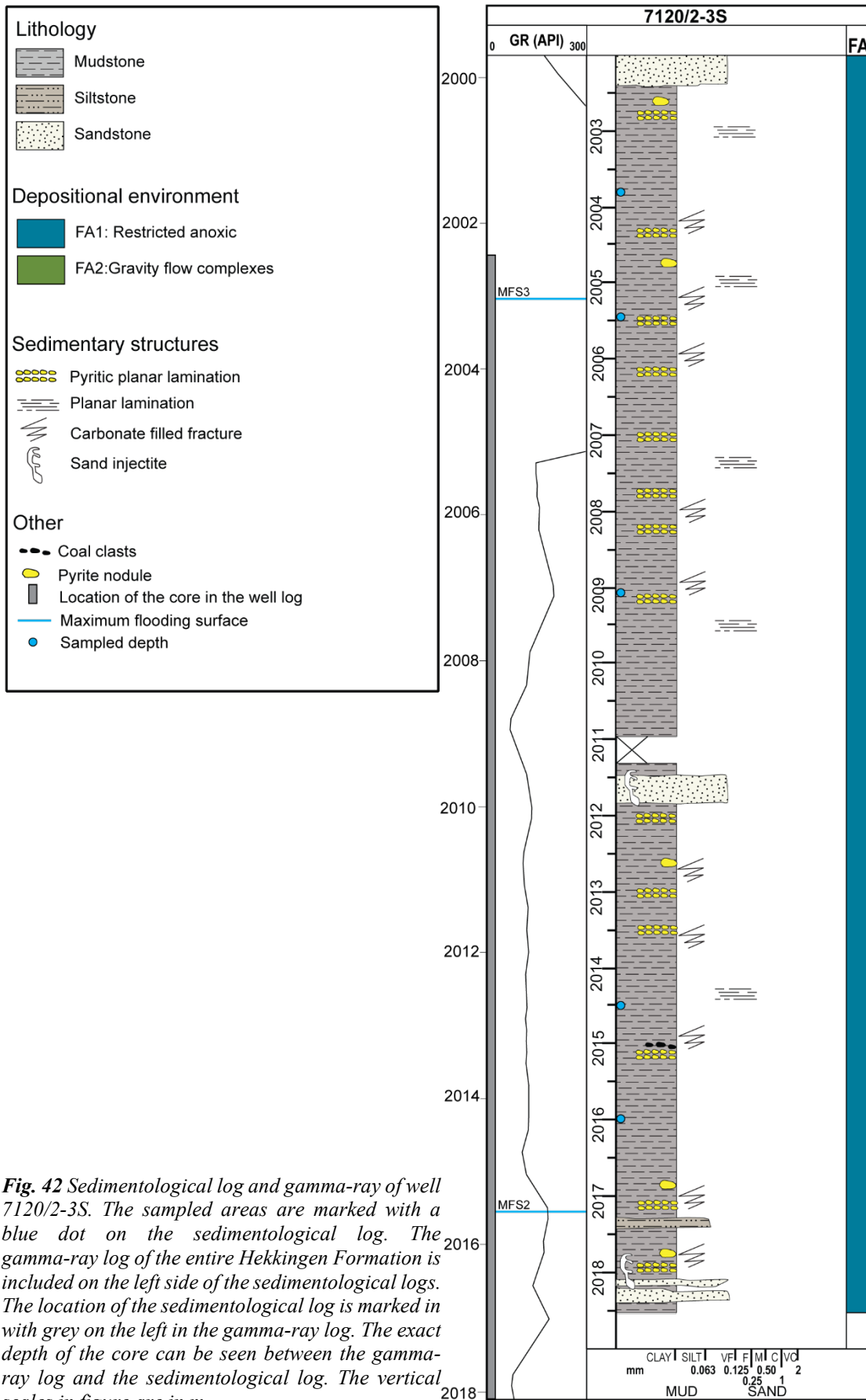


**Fig. 42** Sedimentological log and gamma-ray of well 7120/2-3S. The sampled areas are marked with a blue dot on the sedimentological log. The gamma-ray log of the entire Hekkingen Formation is included on the left side of the sedimentological logs. The location of the sedimentological log is marked in with grey on the left in the gamma-ray log. The exact depth of the core can be seen between the gamma-ray log and the sedimentological log. The vertical scales in figure are in m.

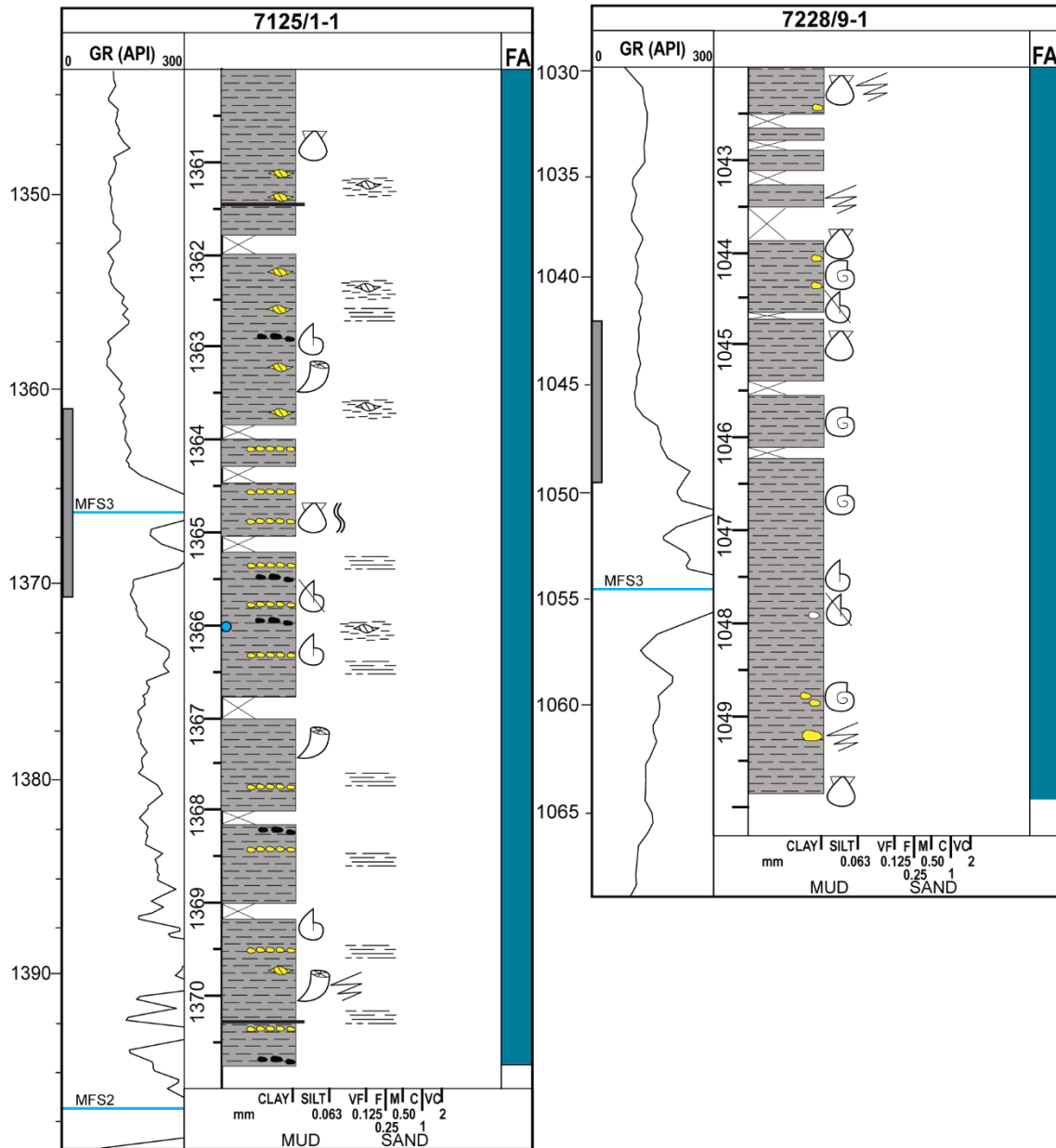


**Fig. 43** Sedimentological log and gamma-ray of well 7125/1-1 and 7228/9-1S. Both belong to FA1. The gamma-ray log of the entire Hekkingen Formation is included on the left side of the sedimentological logs. The location of the sedimentological log is marked in with grey on the left in the gamma-ray log. The exact depth of the core can be seen between the gamma-ray log and the sedimentological log. The vertical scales in figure are in m.

### ***Interpretation***

The fine grain size, dark colour and lack of sedimentary structures imply deposition in a low energy environment. The lack of trace and body fossils, and the abundance of pyrite in the FA, suggest marine anoxic deposition, with excellent preservation potential for organic matter. Anaerobic decomposition the organic matter releases sulfur, which reacts with reduced iron and creates pyrite (Leventhal, 1993; Spirakis, 1996). The precipitated calcite and absence of siderite in the mudstone is a consequence of iron depletion in the seawater, further supporting that deposition took place in a reducing environment (Potter et al., 2005). The sedimentation rate is the main limitation of the growth time of the pyrite (Wilkin et al., 1996; Gallego-Torres et al., 2015). The large size of the pyrite crystals observed in the FA indicates deposition at low sedimentation rates. The close proximity to the redoxcline may explain the presence of some body fossils, and some bivalve species are known to be adaptable to low oxygen and low pH environments (Taylor & Lewis, 1970; Duff, 1975). However, the overall absence of benthic fauna and bioturbation of the sediments imply that redoxcline was located above the sediment-water interface. The larger pieces of terrestrial organic material observed in the cores from 7120/2-2 and 7120/2-3S suggest proximity to a terrestrial source of organic matter.

In well 7120/2-3S (Fig. 42), the sand-bodies were interpreted to be sand injectites. The ptymatic folding observed in the sand-bodies is a common geometry observed in sandstone dikes, and indicates compaction from the host-strata after the formation of the dike (Surlyk & Noe-Nygaard, 2001; Hillier & Cosgrove, 2002; Hurst et al., 2011). The injection of sand is promoted by hydrofracturing of fine-grained material, creating a pressure difference and an upward fluid-flow for the sand to follow. A high energy fluid-flow will create an erosive boundary between the sand and the mud, as observed in the core (Fig. 41; Hurst et al., 2011). Causes for sand injectites include earthquakes, load-induced overpressure due to gravitational instability, and sudden loading due to storm waves (Hildebrandt & Egenhoff, 2007; Jonk et al., 2007; Hurst et al., 2011). The proximity to the Asterias Fault Complex and the Loppa High suggests tectonic activity in this area during the deposition of the Alge Member in well 7120/2-3S.

The lack of correlation between the core log and the high-value spikes in the gamma-ray log indicate that the origin of the spike is not connected to changes in lithology or compositional elements that can be observed in the rock. However, the succession of Alge Member with FA1

has high-value gamma-ray spikes indicating there is a link between the spikes and the depositional environment.

## **FA 2: Turbidity current (Gravity flow complexes)**

FA2 comprises of lithofacies F4–F6, interbedded sandstone and siltstone, soft sediment deformed sandstone and parallel laminated sandstone.

### ***Description***

FA2 is observed in the top of the core interval in 7120/2-2 as a bed of parallel laminated, very fine to fine white to pale grey sandstone with interbedded dark grey to black mudstone (F6; Table 16; Fig. 39). The lamina varies from >1 to 10 mm in thickness and displays a fining upward trend. The sandstone succession is preceded and succeeded by claystone. Soft sediment deformation, in the form of flame structures, was observed once in the package (Fig. 39). Toward the top of package, the lamination turns wavy and convoluted, followed by a layer with authigenic glauconite (Fig. 44). No fossils were observed.

In well 7219/8-1S, the FA is observed as a white to pale grey, silty to very fine sandstone interbedded/lamina in blocky dark grey to dark to black mudstone (F4). The sandstone layers range in size from less than 1 mm to 15 mm. Sedimentary structures as asymmetric ripples and flaser bedding is present, separated by intervals of planar lamination (Fig. 44). The succession in well 7219/8-1S displayed several changes in the energy during deposition, from parallel lamina to wavy and back to parallel etc. The overall succession is coarsening upward. Soft sediment deformation in the form of flame structures is present in the lamina (F5; Fig. 39). The viewed core interval displays a coarsening upward trend. No fossils were present.

The viewed succession of the Alge Member in well 7219/8-1S only consists of FA2, while well 7120/2-2 consists of both FA1 and FA2 (Fig. 45). The succession in well 7120/2-2 shows a rapid decrease in the gamma-ray log when there is a change from the mudstone in FA1 to the fine sandstone in FA2 (Fig. 45). There is finer material (silt to very fine sandstone) in the Alge Member in the core from well 7219/8-1S, but overall low gamma-ray signatures in the well log (Fig. 45).

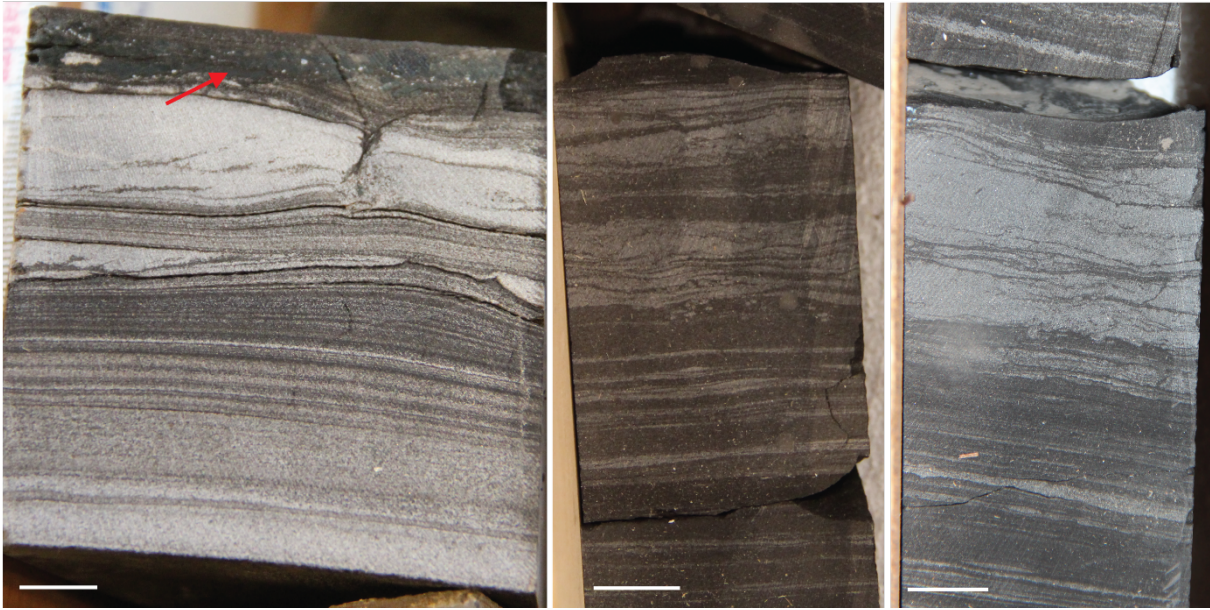


**Fig. 44** Left photo: transition from parallel lamination to wavy lamination toward the top of the FA in well 7120/2-2. A layer of authigenic glauconite is located at the top of the FA (marked with red arrow). Middle and right photo: The FA in well 7219/8-1, display asymmetric ripples and flaser bedding, here shown at depths 4270.00 and 4272.45, respectively. The line in the left lower corner of the photos represent 1 cm.

### ***Interpretation***

The very fine sandstone and interbedded mudstone indicate deposition in a low energy environment below storm-weather wave base, possible with mudstone as background sediments. The facies association displayed either parallel lamina or wavy and convolute lamina, indicating there was a change in the energy in the system while the FA was deposited. The authigenic glauconite observed in well 7120/2-2 places the deposition in a reducing environment where the seawater-sediment interface have been undisturbed for long time-periods (Triplehorn, 1965; Odin & Matter, 1981; Srodon, 1999). The authigenic glauconite is, therefore, an indication that sedimentation-hiatuses occurred during the deposition, implying that the FA have experienced periodic sedimentation. The FA is interpreted to be a low-density turbidity current, where the parallel laminated succession represents the suspension settling  $T_d$  and the wavy and convolute laminated represent  $T_c$  of a Bouma sequence (Bouma, 1962). The formation of convolute lamination occurs syn-deposition by the shear-stress on the bed from the current (Blatt et al., 1972). The flame structures in the parallel lamina is a result of sediments with higher density, in this case, the coarser sand was loaded rapidly or unevenly on the less dense mud, and the irregular pressure caused the water to escape creating the structures (Owen, 2003). The coarsening upward suggests that the overall energy is increasing toward the top of the Alge Member. The increases in energy may be the

result of storms triggering an increased transport of sediments into the basin or reflect the timing of fault activity feeding sediments to the system.

The low gamma-ray values observed in the FA2 indicate that deposition where sediments with a grain size coarser than mud are present or there is deposition with a slight increase in energy and sediment input will not contain the compositional element causing the spike.

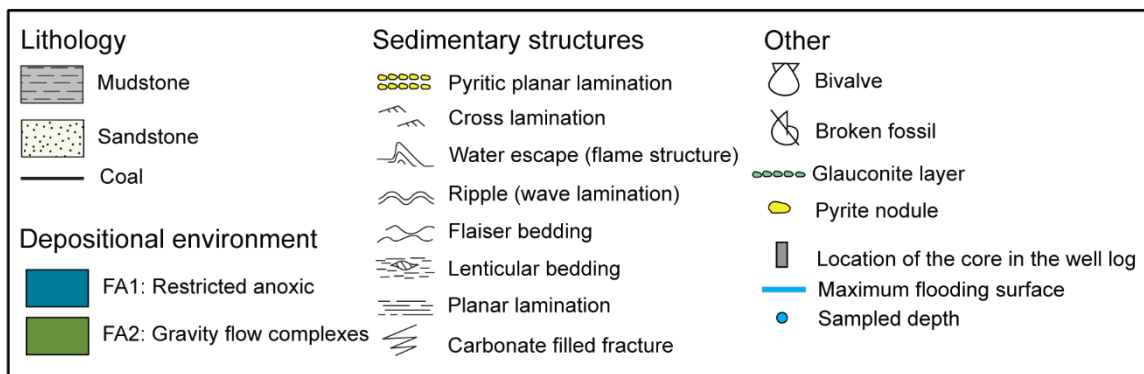
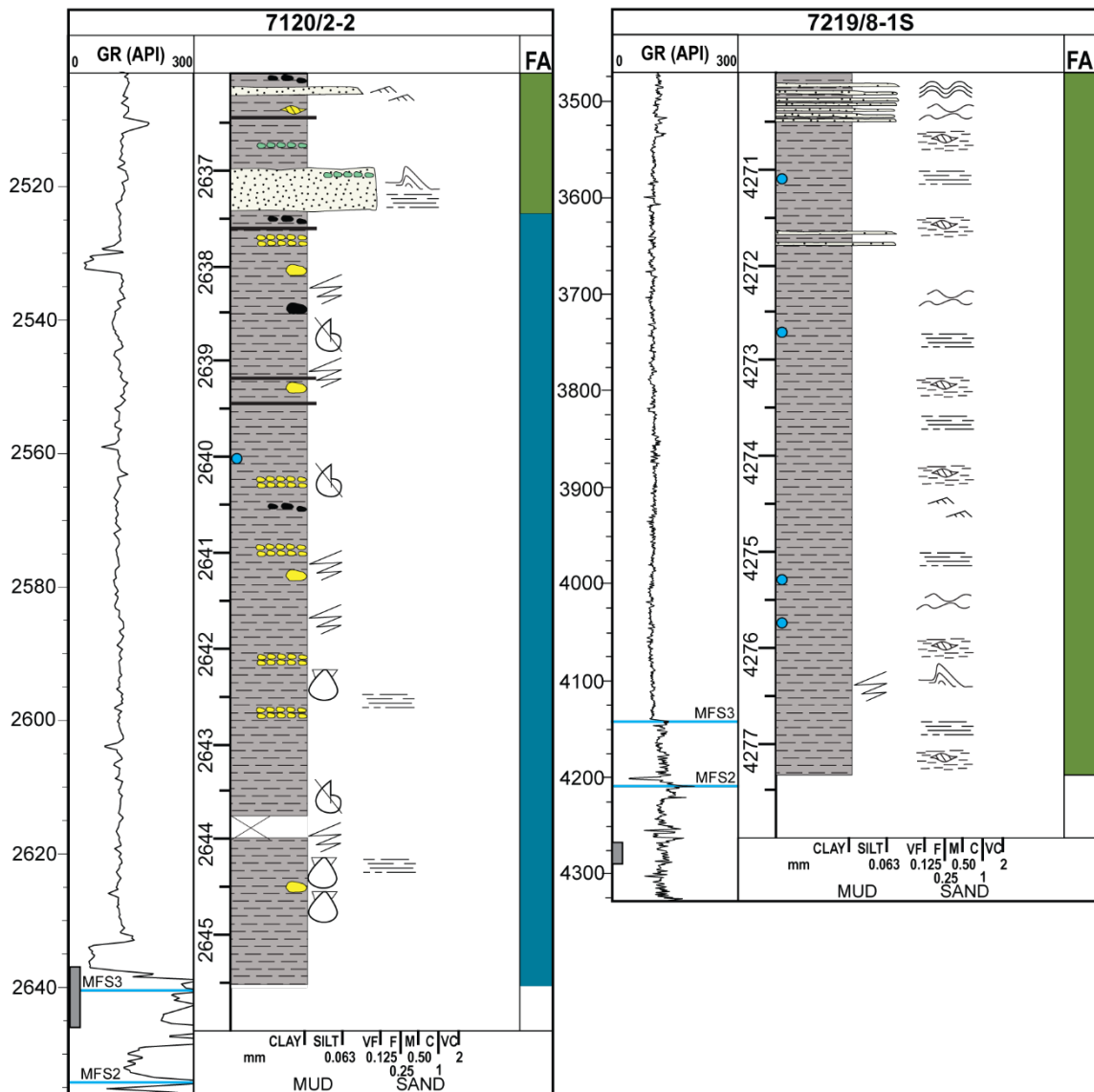


**Fig. 45** Sedimentological log and gamma-ray of well 7120/2-2 and 7219/8-1S. The gamma-ray log of the entire Hekkingen Formation is included on the left side of the sedimentological logs. The location of the sedimentological log is marked in with grey on the left in the gamma-ray log. The exact depth of the core can be seen between the gamma-ray log and the sedimentological log. The vertical scales in figure are in m.

## Summarized interpretation

Restricted anoxic deposition of the Alge Member took place in the Hammerfest Basin and northward toward the Nordkapp Basin, whereas the uplifting Loppa High caused the Alge Member to be deposited as gravity flow complexes westward (Fig. 46). However, the great distance between the wells and only five cores were view in the study, so there is great uncertainty in interpreting the entire area based on these. West of the Loppa High and in the Hammerfest Basin, the gravity flows are likely triggered by tectonic activity in the fault complexes (i.e. the Bjørnøyrenna Fault Complex, the Ringvassøy-Loppa Fault Complex and the Asterias Fault Complex; Fig. 6). Thus, there is deposition of coarser sediments (silt and very fine sand), and the change in deposition might be connected to the lack of high-value spikes and high-value gamma-ray signatures in the Alge Member in this area. The prominent high-value spike in the gamma-ray log and the high-value gamma-ray signature seem to be connected to the area where restricted anoxic deposition is observed in the cores of the Alge Member (Fig. 4; Fig. 37; Fig. 46).

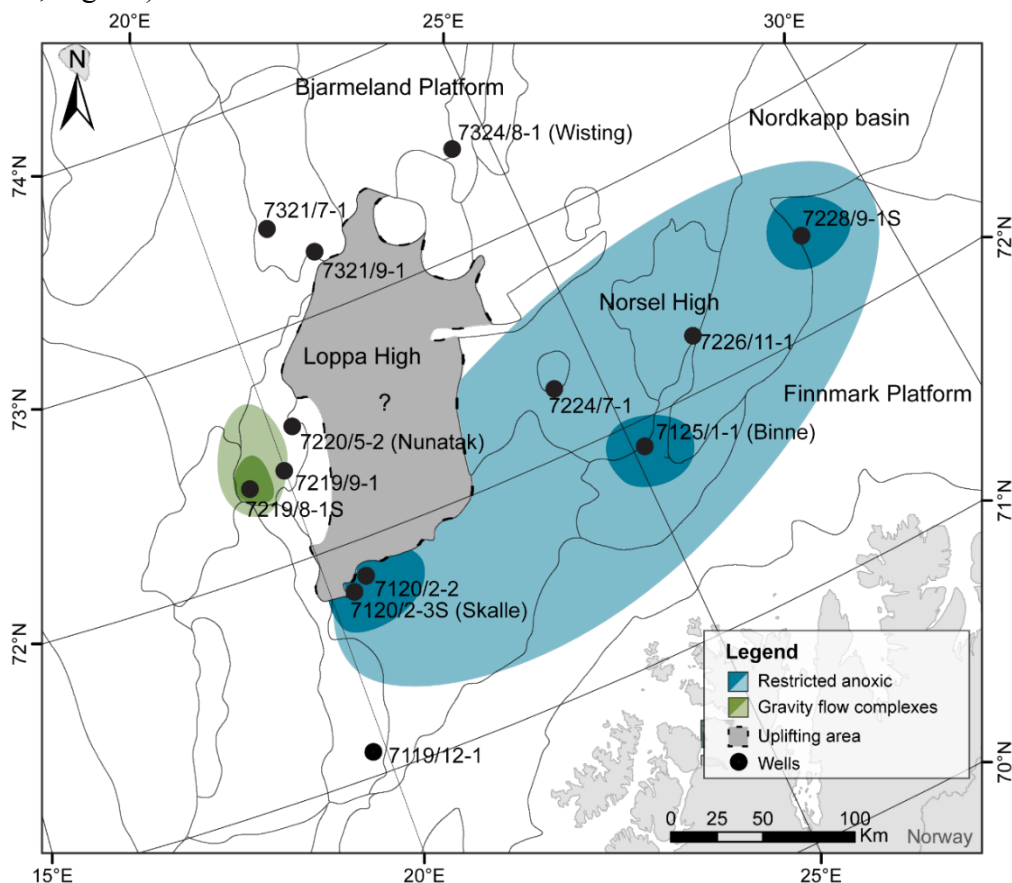


**Fig. 46** The lithofacies marked around the wells and the area between in shaded colour. The Alge Member is interpreted to have low energy anoxic deposition in the Hammerfest Basin and eastward to the areas surrounding the Nordkapp Basin. On the western side of the Loppa High, the depositional environment of the Alge Member is interpreted to be a gravity flow complexes (turbidity flow). The gravity flow complexes can be linked to the tectonic activity in the fault complexes (Bjørnøyrenna Fault Complex and the Ringvassøy-Loppa Fault Complex) located on the western side of the high (Fig. 6). Note that the great distance between the wells.

## 5. DISCUSSION

### 5.1 Compositional variations in the Alge Member

Principal component analyses do not show any correlation between the high-value gamma-ray spikes and any other of the investigated compositional elements of the Alge Member. However, a combination of the compositional elements might still point toward the origin of the spike. When studying the compositional elements and their geographical distribution in the area, there is a distinct difference in the composition of the Alge Member deposited west–northwest of the Loppa High and the Alge Member deposited in the areas south and toward the east (Ringvassøy-Loppa Fault Complex and toward the Nordkapp Basin). The same geographical separation is also found for the distribution of the wells where the Alge Member displays high-value gamma-ray spikes and where there are no spikes in the succession (Fig. 4; Marín, personal communication, October 15, 2018).

The westernmost area has an overall low gamma-ray signature in the Alge Member (Fig. 37). This area has chlorite present in the clay fraction, suggesting that the conditions have been less reducing than in the south and areas to the east where the chlorite is likely to have experienced reduction and thus is missing. The high mineral content and the high quartz content observed in the Alge Member at the northwestern part of the Loppa High indicate subaerial exposure of the high in during the deposition of the member. This is further supported by the terrestrial originating macerals present in the Alge Member. A potential source for both the quartz and the terrestrial material is Greenland as it at the time, as it according to plate tectonic reconstruction by Ziegler (1988), was located immediately west of the study area (Fig. 5). However, as the quartz content is higher toward the uplifting Loppa High (Fig. 22; Indrevaer et al., 2017), it suggests that the high the main source area. The west–northwestern area also displays overall lower source rock potential, both in lower TOC, Hi and S2, the latter two probably being caused by the higher maturity of the source rock in this area. The lower TOC can be related to the higher mineral count in this area, as organic matter is better preserved in finer grained material (Hedges & Keil, 1995). The seismic facies indicate tectonic activity, supported by the turbidity flow observed in the core log (Fig. 46).

The south and eastward area, from the Hammerfest Basin to the Nordkapp Basin, has experienced an anoxic deposition of the Alge Member with preservation of organic material. High values of TOC, S2 and HI are observed in the area, but the source rock is mainly immature

(Fig. 18). Thus, this area seems to follow the common perception and interpretation of the Hekkingen Formation as a restricted anoxic deposition (Leith et al., 1993; Mørk et al., 1999; Smelror et al., 2001). This is further supported by the higher count of macerals in this member. The minerals are mainly clay minerals, and the clay minerals lack the chlorite. Based on the examined cores, the Alge Member is suggested to be deposited in a restricted anoxic environment, with a high amount of pyrite formation observed in the cores. In this area, the high-value gamma-ray spikes and the overall gamma-ray value in the Alge Member is higher, indicating an indirect link between the observed high-value gamma-ray readings and the source rock quality, as both seem to be linked to an anoxic depositional environment.

The distribution of terrestrial-derived and marine-derived macerals in the samples may be used as an indicator of the proximity to the paleoshoreline. Samples with a high terrestrial input can be interpreted to have been deposited closer to a shoreline and possibly at a shallower water depth than the samples with mainly marine content (Fig. 47). The thickness of the Alge Member and the sedimentation rate may also suggest where the sediment input are likely to cause subsidence of the basin (e.g. well 7219/8-1S; Table 12). The maceral content suggests that the wells located around the Nordkapp Basin were deposited in shallow water at the time of deposition. The Hammerfest Basin, the Ringvassøy-Loppa Fault Complex and the Bjørnøyrenna Fault Complex have more marine maceral content, which suggests a more distal paleoshoreline (Fig. 47). The areas with interpreted shallow water correlate with the areas where the Alge Member have a high erratic gamma-ray signature. This suggests that water depth may influence the gamma-ray signature. Alge Member in well 7324/8-1 (Wisting) is interpreted to have been deposited in the shallowest water. The rather high quartz content in the Alge Member in this well may have been caused by erosion linked to activity in the Hoop Fault Complex during the Jurassic.

The succession of the Alge Member west of the Loppa High (green profile in Fig. 47) display closer proximity to the paleoshoreline for the wells in the Polhem Subplatform, but the Alge Member sampled from the basinward wells contains more marine macerals suggesting a greater water depth basinward. Based on the macerals, the deepest water depth is interpreted in the subsiding basin west of the Loppa High and well 7120/2-2 in the Hammerfest Basin. The

Hammerfest Basin show no sign of major subsidence during Jurassic (Fig. 3), suggesting that a restricted deposition with low terrestrial input may be mistaken to be a deep-water deposition.

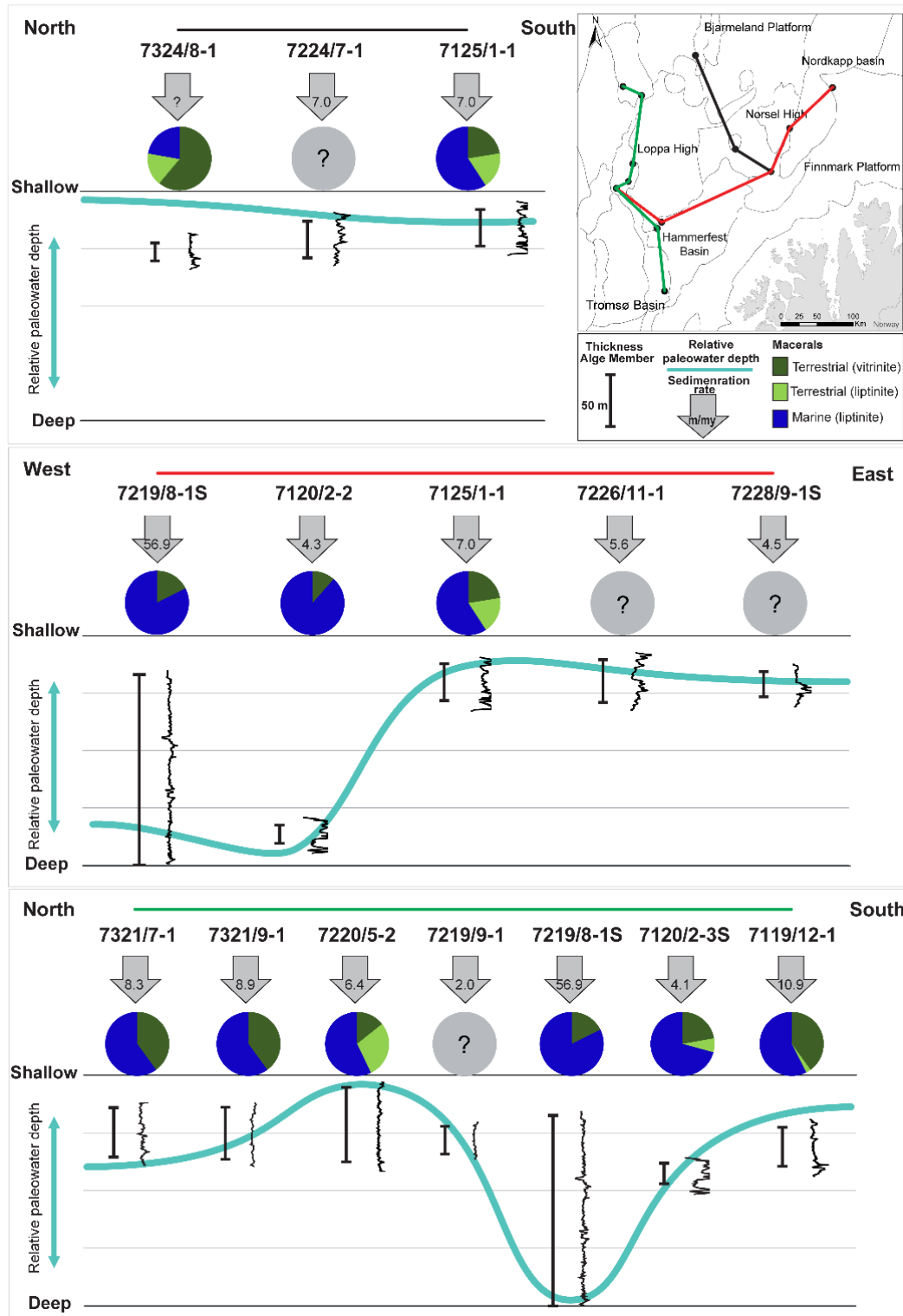


**Fig. 47** Relative paleowater depth based on the maceral content in the wells and compared with the thickness of the Alge Member. The gamma-ray signature of the Alge Member can be seen to the right of the thickness of the member. The gamma-ray shows a higher-value signature in the Alge Member deposited at shallower water depths.

The sampled MFSs with a prominent high-value gamma-ray spike all have a clay mineral composition consisting of interlayered illite-smectite and kaolinite. They are rich in clay minerals, some are pyrite rich, they have a high maceral count, a high TOC and a high generation potential (S2), and the Tmax defines them as immature to early mature. However, few of the sampled high-value spikes include all the mentioned compositional elements, and these elements are not restricted to the sampled high-value spike (Table 18). The composition observed in the sampled high-value spikes (i.e. clay content, clay composition and high organic content), points to an anoxic depositional environment, which also corresponds to the viewed cores and the observed seismic facies. However, this depositional environment is interpreted for the entire succession of the Alge Member for several of the wells in the study area, regardless of whether there is a high-value spike or not in the succession. Hence, the cause of the high-value gamma-ray spike seems to be changes in the depositional environment.

**Table 18** Summary of the observed compositional variation in the sampled MFSs.

<i>Well</i>	<i>Depth (m)</i>	<i>High-value spike</i>	<i>Clay mineral group</i>	<i>TOC</i>	<i>S2 (mg/g)</i>	<i>Tmax</i>	<i>Clay rich</i>	<i>Pyrite rich</i>	<i>Terrestrial or marine dominated</i>	<i>&gt;70 maceral counts</i>
7120/2-2	2640	X	3a	3.39	12.51	449	X		Marine	X
7120/2-3S	2003	X	3b	10.80	15.55	429	X	X	Marine	
7120/2-3S	2014		3c	13.10	39.49	438	X	X	Marine	X
7125/1-1	1366	X	3b	14.00	51.92	425	X		Marine	X
7125/1-1	1398	X	3b	15.40	54.80	422	X		Terrestrial	X
7219/9-1	1901		?	9.1	28.9	441	?		?	?
7220/5-2	1408		2a	3.29	5.59	432			Marine	
7224/7-1	836	X	3b	11.40	35.14	418	?		?	?
7228/9-1S	1055	X	?	8.60	32.60	415	?		?	?
7321/7-1	1933		3a	8.56	4.93	477			Marine	X
7324/8-1	620		2a	3.97	8.28	430			Terrestrial	

## 5.2 Uranium precipitation

It has been suggested by Bugge et al. (2002) that the higher TOC in the Alge Member causes it to be more radioactive than the overlying Krill, thus explaining the change in the gamma-ray log between the members. However, the sampled depths of high-value spikes show that high TOC content is not always the case (Table 18). Observations from the spectral gamma-ray logs show that the uranium content in the rock is closely related to the gamma-ray signatures and the prominent high-value spikes (Fig. 38).

Uranium is present in oxygenated seawater in a highly soluble and mobile hexavalent form, U(VI), whereas the immobile and insoluble tetravalent state, U(IV), occur in reducing conditions (Swanson, 1960; Langmuir, 1978; Anderson, 1982; Carpenter et al., 1984; Anderson, 1987). The absorption or precipitation of uranium is an ambiguous process, and a suite of processes often operates in parallel. However, two main processes seem to control the uranium precipitation in black shale. The reduction of uranium from U(VI) to U(IV) occurs at the same conditions, i.e. same redox potential, pH and alkalinity, as for Fe(III) reduction to Fe(II) (Swanson, 1960; Langmuir, 1978; Cochran et al., 1986; Cumberland et al., 2016). Reduced iron will react with sulfate being reduced from the seawater by sulfur reducing bacteria, and form pyrite (FeS) (Bjørlykke et al., 2015). Thus, implying that the precipitation of U(IV) and FeS formation occurs concurrently (Bargar et al., 2013). Iron significantly influences the uranium chemistry, and Fe(II) compounds, e.g. pyrite, have the ability to reduce uranium to U(IV), causing the U(VI) to precipitate onto the mineral surface (Descostes et al., 2010; Cumberland et al., 2016). Pyrite is a commonly observed mineral in the Alge Member, suggesting that the redox conditions in the member would allow uranium precipitation.

The redox state of solutions in sedimentary rock is mainly determined by the presence of sulfur in various oxidation states, e.g. sulfide ( $\text{H}_2\text{S}$ ), disulfide ( $\text{FeS}_2$ ), sulfate ( $\text{CaSO}_4$ ) and polysulfide ( $\text{S}_n\text{S}^{2-}$ ) (Spirakis, 1996). The balance between the reducing and oxidizing elements in the sediments control the redox chemistry of the sediments, the main oxidation elements being oxygen and sulfate, while the reducing agents are represented by organic carbon and reduced sulfur from organic material (e.g. pyrite and sulfide; Spirakis, 1996). Thus, the reduction and adsorption of uranium are connected to the amount of organic material in the sediments, explaining the correlation between higher TOC in the Alge Member and the increase in the gamma-ray values in the member.

The reduction of uranium must take place in the sediment-seawater interface, as the redox potential will not become low enough for the uranium to precipitate in the water column (Anderson, 1982). The precipitated uranium is, however, highly sensitive to changes in the redox conditions, and exposure experiments where anoxic sediments are exposed to air show that oxidation of the reduced uranium occurs rapidly (Nagao et al., 1992). Consequently, a shift from anoxic bottom conditions to oxic, would lead to the oxidation and removal of the deposited uranium in the sediments.

The hypoxia threshold in the water column was set to  $<63\mu\text{M O}_2$  by Jessen et al. (2017). At low bottom-water oxygen conditions, hypoxic or anoxic, the benthic fauna will not survive and need to relocate, leaving microbes to dominate the organic matter decomposition. Thus creating a restricted and ineffective depolymerisation of the complex molecules, as the microbes do not perturb the sediments (Diaz & Rosenberg, 2008). Thus, the hypoxic zone is optimal for uranium precipitation as the oxidized water supplies U(VI) to the hypoxic zone where it is precipitated in the anoxic sediment interface. During a transgression, the sea level will rise and the hypoxic zone will follow, and leave a trace of deposited uranium in the bottom sediments (Fig. 48). In the areas with a high-value gamma-ray signature is present at the top or the base of the Alge Member, this could suggest when the member was in the hypoxic zone. The thickness of the high-value gamma-ray spikes in the Alge Member suggests a range of ~100 000 to 500 000 years for a spike to be deposited, and consequently the time spent in the hypoxic zone. At shallower water depth, the hypoxic zone will be more sensitive to minor sea level fluctuations and responses in the hypoxia zone would allow of precipitation followed by oxidation and renewed precipitation of uranium. These fluctuations in sea level and the precipitation process may explain the erratic gamma-ray signature observed in the wells (Fig. 48). The areas where the Alge Member only displays low-value signatures, the deposition of the member could be at anoxic deep waters below the hypoxic zone, or at oxic shallow water above the hypoxic zone (Fig. 48).

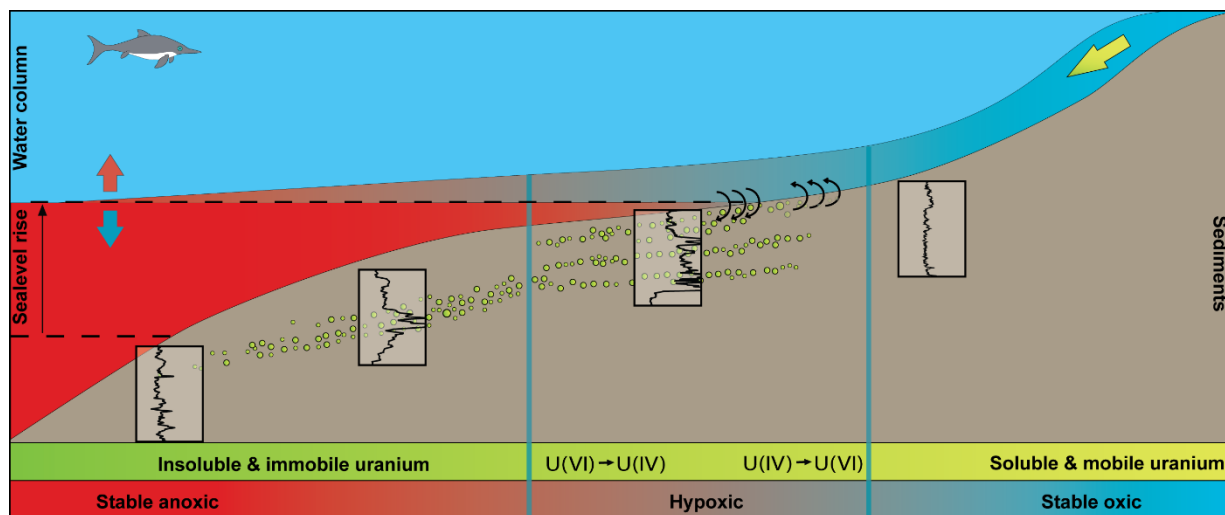


**Fig. 48** Conceptual model of uranium precipitation and relation to the gamma-ray signatures and the prominent gamma-ray spikes. The uranium is sourced from continental weathering and follow the oxic water in its soluble and mobile form U(VI). The hypoxic zone allows the oxic water to encounter anoxic sediments and uranium is precipitated as U(IV). With a rapid sea-level rise, the hypoxic zone will leave a trail of precipitated uranium, whereas at shallower water depth, the hypoxic zone will be more sensitive to minor changes in sea-level and get an erratic gamma-ray signature. Areas where the Alge Member has low value gamma-ray signatures are either deposited in deep-water environment with no oxic (or uranium) input or in shallow and oxic conditions.

Relating the spike to sea level fluctuations makes it possible to map out the change in the sea level during the deposition of the Alge Member, from the deposition of the MFS2 to the MFS3 (Fig. 49). During the deposition of the MFS2, the areas with no prominent spike in this MFS were either deposited at a shallow oxic environment or in anoxic deep water. No uranium will be precipitated in these environments, thus no prominent gamma-ray spike. The areas with a high-value gamma-ray spike at the MFS2 was in the hypoxic zone. As the Middle–Upper Jurassic transgression continues, these areas would become anoxic as the hypoxic zone reached the former shallow water depths, allowing for the deposition of the prominent spike in the MFS3. The areas with the erratic gamma-ray signature and prominent spikes at both MFSs are interpreted to be deposited at shallow water depth and stayed in the hypoxic zone throughout the deposition of the Alge Member (Fig. 49). In the area west of the Loppa High, the tectonic activity could have led to a rapid sea level rise inferring anoxic conditions, thus avoiding the enrichment of uranium causing the prominent spikes. Alternatively, the areas where the wells have no prominent spikes and a low-value signature are not encountered by the hypoxic zone at all; they may either be deposited too deep (constant anoxic) or too shallow (constant oxic) for the precipitation to take place. However, the paleo-configuration of the Loppa High seems to have functioned as a barrier between the northwestern and southeastern parts of the study area. In addition, the suggested change in sea level does not take into consideration that the deposition of the MFS did not occur as one simultaneous event, but was deposited at different times in the study area (Fig. 27; Fig. 28).

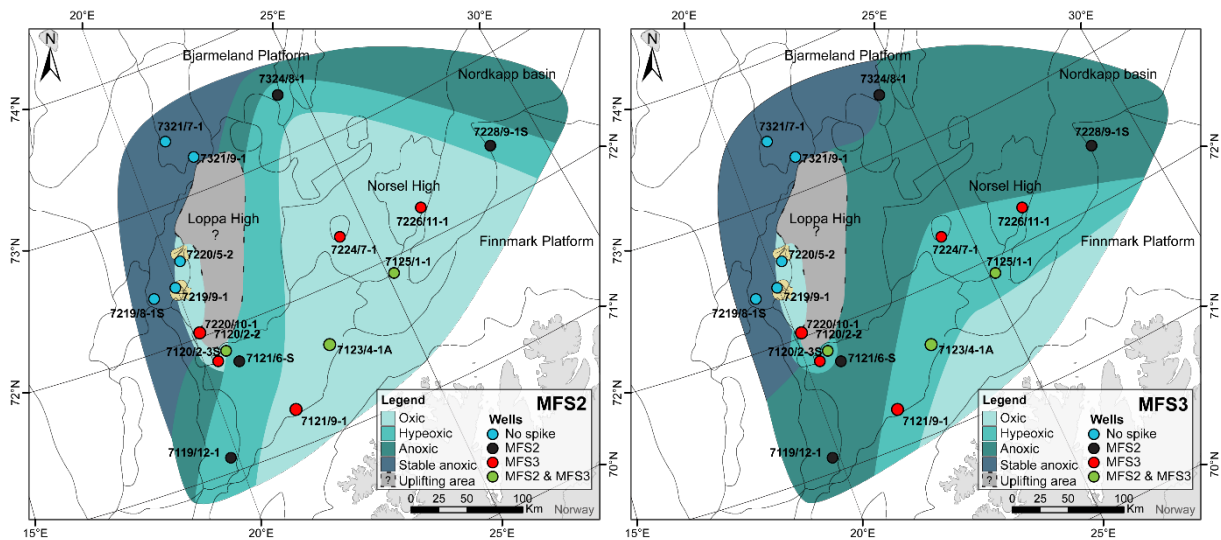


**Fig. 49** Paleogeographic map of the development of the anoxic zone the southwestern Barents Sea based on the model from Fig. 49 and the gamma-ray signature of the wells in the dataset. Left: Deposition of MFS2. Right: Deposition of MFS3.

Applying the suggested model (Fig. 48), to the wells in the study area gives a simple overview of the distribution of the anoxic and hypoxic environments in the study area, and it shows how the anoxic zone spread during the deposition of the Alge Member (Fig. 49). However, the model is not perfect, e.g the Alge Member in well 7125/1-1 has an erratic pattern in the gamma-ray log throughout deposition but is positioned on the middle of an oxic zone during the deposition of MFS2 (Fig. 49). The timing of deposition could influence this, as the deposition of MFS2 occurred later than in the neighbouring wells (Fig. 27). In order to produce a more detailed map, the framework was applied to all the wells in the study area where the high-value gamma-ray spikes in the MFSs were identified (Fig. 50; Marín, personal communication, October 15, 2018). Moreover, structural details were added to the maps (i.e. the subsiding Nordkapp Basin, the location of salt structures). During this study, the gamma-ray signature was redefined for one of the wells (7120/2-2; 4.4.4 Gamma-ray signature, p.63), indicating that some uncertainty should be considered when applying the model.

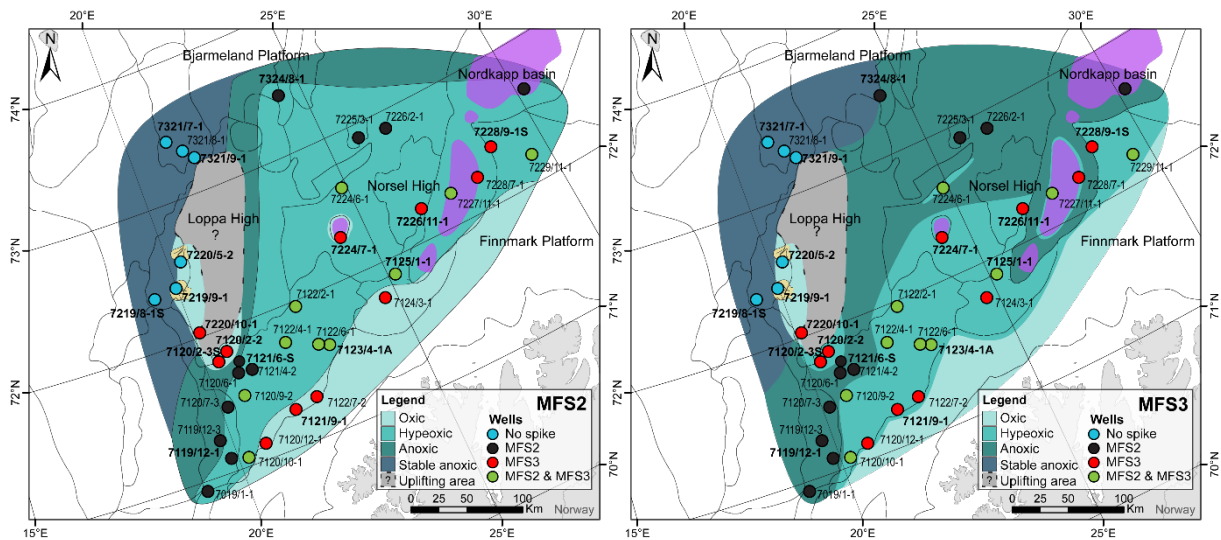


**Fig. 50** Paleogeographic map of the development of the anoxic zone the southwestern Barents Sea based on the wells analysed by Marin (personal communication, October 15, 2018). Left: Deposition of MFS2. Right: Deposition of MFS3. Pink areas represent salt structures with recorded halokinetic activity during the Late Jurassic (Gabrielsen et al., 1990; Rojo & Escalona, 2018).

The precipitation of uranium would occur as long as there is a change from anoxic to oxidic conditions in the water column combined with reducing bottom conditions. Hence, other factors may influence the anoxic-oxidic conditions in the marine environment (Table 19). Sea currents or hyperpycnal flows could introduce oxidized water and make U(VI) precipitate. The variation of gamma-ray signatures in the Alge Member could be a result of the ongoing rifting and high sediment input causing subsidence in the basin west of Loppa High, forming new pathways for oxygen-rich ocean currents. The time it takes to deposit a prominent spike rule out seasonal variation as a cause, but climate change may influence the oxygen level in the seawater. A warmer climate could lead to increased weathering and therefore more nutrition in the seawater followed by a blooming of marine organisms causing anoxic conditions at shallow water depth. Sediment input into the basin due to the rifting may be a source for uranium into the shelf. However, the overall low sedimentation rate in the Alge Member restrict the amount of uranium being transported onto the shelf. High-value spikes are also absent in the areas where the Alge Member has the highest sedimentation rates.

**Table 19** Summary of the possible reasons for oxic-anoxic changes leading to uranium precipitation and deposition of high-value gamma-ray spikes in the Alge Member.

<i>Influence</i>	<i>Effect</i>
<i>Sea level changes</i>	Explains the single spikes and the erratic signature observed when two prominent spikes are present
<i>Ocean currents</i>	Tectonic activity may result in oxygen rich ocean currents being diverged, bringing oxygen rich water to previously anoxic bottom conditions, hence precipitation of uranium
<i>Hyperpycnal flows</i>	Could potentially bring oxygen rich water to anoxic bottom sediments
<i>Seasonal changes</i>	Explains the erratic pattern
<i>Climate change</i>	May explain the precipitation and no precipitation in the erratic patterns, but do not explain the single peaks
<i>Sediment input</i>	Sediment input into the shelf and increase input during rifting would be a uranium source

An alternative theory for the presence of spikes in source rocks is linked to the permeability of these. Assuming that under the right conditions, uranium is deposited during the entire anoxic interval, resulting in a high gamma-ray signature (Fig. 51). Circulation of oxic formation fluids in the permeable layers of the source rock could dissolve the uranium and remove it from the succession, while the impermeable layers still would have a high uranium concentration and create prominent spikes in the gamma-ray log (Fig. 51). This theory is dependent on stable anoxic bottom conditions, and a constant supply of uranium throughout the deposition of the Alge Member. No permeability data are, however, available to test this hypothesis.

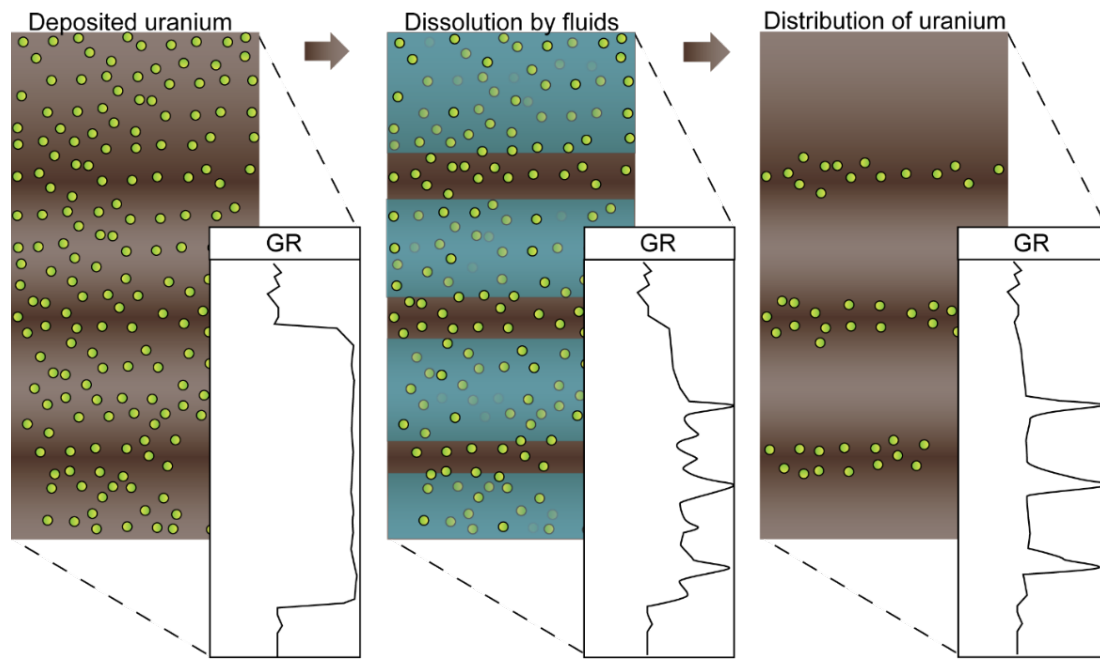


**Fig. 51** Conceptual sketch of distribution and preservation of uranium in the impermeable layers in the source rock. Assuming constant precipitation of uranium in anoxic conditions, the source rock would have an overall high gamma-ray reading throughout the succession. Circulation of oxic formation fluids would dissolve the precipitated uranium in the permeable layers of the source rock (illustrated with blue), leaving the uranium in the impermeable layers which caused the prominent spikes in the gamma-ray log.

## 6. CONCLUSION

The examination of the organic and inorganic content in the Alge Member of the Hekkingen Formation in order to define the origin of the prominent high-value gamma-ray spike leads to the following conclusions:

- Several of the compositional variations in the source rock are indirectly linked to the occurrence of high-value spikes.
- The high-value gamma-ray spikes occur in the source rock independent of the TOC-content.
- The prominent gamma-ray spikes observed in the Alge Member is be directly related to the uranium content in the source rock.
- The conditions needed for uranium precipitation is closely connected to anaerobic decomposition of organic content.
- The precipitation of the uranium is limited to the interface between anoxic sediments and oxic water transporting the uranium. Potential controls on the oxic-anoxic conditions include
  - Water depth and sea level fluctuations
  - Ocean currents
  - Hyperpycnal flows
  - Seasonal changes
- Assuming the uranium precipitation is controlled by changes in sea level, the occurrence of the high-value gamma-ray spikes makes it possible to model the development of the anoxic zone in the southwestern based on the gamma-ray signatures.
- The Alge Member show a large variation in facies both vertically in wells and laterally over the geographic area.
- The existence the high-value gamma-ray spikes and good source rock interals are indirectly linked, as both are the result of hypoxic-anoxic deposition.

## REFERENCES

- ABDI, H., & WILLIAMS, L. J. (2010). Principal component analysis. *Wiley Interdisciplinary Reviews: Computational Statistics*, 2(4), 433-459.
- ANDERSON, R. F. (1982). Concentration, vertical flux, and remineralization of particulate uranium in seawater. *Geochimica et Cosmochimica Acta*, 46(7), 1293-1299.
- ANDERSON, R. F. (1987). Redox behavior of uranium in an anoxic marine basin. *Uranium*, 3(2-4), 145-164.
- ASTM D7708 - 11. (2011). Standard Test Method for Microscopical Determination of the Reflectance of Vitrinite Dispersed in Sedimentary Rocks. from ASTM International [www.astm.org](http://www.astm.org)
- BARGAR, J. R., WILLIAMS, K. H., CAMPBELL, K. M., LONG, P. E., STUBBS, J. E., SUVOROVA, E. I., LEZAMA-PACHECO, J. S., ALESSI, D. S., STYLO, M., WEBB, S. M., DAVIS, J. A., GIAMMAR, D. E., BLUE, L. Y., & BERNIER-LATMANI, R. (2013). Uranium redox transition pathways in acetate-amended sediments. *Proceedings of the National Academy of Sciences of the United States of America*, 110(12), 4506-4511.
- BERGLUND, T., AUGUSTSON, J., FAERSETH, R., GJELBERG, J., & RAMBERG-MOE, H. (1986). The evolution of the Hammerfest Basin. In SPENCER, A. M. (Ed.), *Habitat of hydrocarbons on the Norwegian Continental Shelf* (pp. 319-338). London: Graham & Trotman for the Norwegian Petroleum Society.
- BJØRLYKKE, K., HELLEVANG, H., AAGAARD, P., & JAHREN, J. (2015). Finding oil and gas with pyrite. *Nyheter - Olje og gass*. Retrieved from <http://www.geoforskning.no/nyheter/olje-og-gass/1056-finding-oil-and-gas-with-pyrite>
- BLAICH, O. A., TSIKALAS, F., & FALEIDE, J. I. (2017). New insights into the tectono-stratigraphic evolution of the southern Stappen High and its transition to Bjørnøya Basin, SW Barents Sea. *Marine and Petroleum Geology*, 85, 89-105.
- BLATT, H., MIDDLETON, G. V., & MURRAY, R. C. (1972). Sedimentary Structures. In BLATT, H., MIDDLETON, G. V., & MURRAY, R. C. (Eds.), *Origin of sedimentary rocks* (pp. 111-184). Englewood Cliffs, N.J: Prentice-Hall.
- BOUMA, A. H. (1962). *Sedimentology of some Flysch deposits; a graphic approach to facies interpretation*. Amsterdam: Elsevier Pub. Co.
- BRAUT, T. I. (2018). *Middle to Upper Jurassic Depositional Setting in the Hammerfest Basin, Southwestern Barents Sea*. (M.Sc.), University of Stavanger, Stavanger

- BUGGE, T., ELVEBAKK, G., FANAVOLL, S., MANGERUD, G., SMELROR, M., WEISS, H. M., GJELBERG, J., KRISTENSEN, S. E., & NILSEN, K. (2002). Shallow stratigraphic drilling applied in hydrocarbon exploration of the Nordkapp Basin, Barents Sea. *Marine and Petroleum Geology*, *19*, 13-37.
- CARPENTER, R., PETERSON, M. L., BENNETT, J. T., & SOMAYAJULU, B. L. K. (1984). Mixing and cycling of uranium, thorium and <sup>210</sup>Pb in Puget Sound sediments. *Geochimica et Cosmochimica Acta*, *48*(10), 1949-1963.
- CATUNEANU, O., GALLOWAY, W. E., KENDALL, C. G. S. C., MIALI, A. D., POSAMENTIER, H. W., STRASSER, A., & TUCKER, M. E. (2011). Sequence stratigraphy: methodology and nomenclature. *Newsletters on stratigraphy*, *44*(3), 173-245.
- COCHRAN, J. K., CAREY, A. E., SHOLKOVITZ, E. R., & SURPRENANT, L. D. (1986). The geochemistry of uranium and thorium in coastal marine sediments and sediment pore waters. *Geochimica et Cosmochimica Acta*, *50*(5), 663-680.
- CUADROS, J., & LINARES, J. (1996). Experimental kinetic study of the smectite-to-illite transformation. *Geochimica et Cosmochimica Acta*, *60*(3), 439-453.
- CUMBERLAND, S. A., DOUGLAS, G., GRICE, K., & MOREAU, J. W. (2016). Uranium mobility in organic matter-rich sediments: A review of geological and geochemical processes. *Earth-Science Reviews*, *159*, 160-185.
- CURIALE, J. A. (1986). Origin of solid bitumens, with emphasis on biological marker results. *Organic Geochemistry*, *10*(1), 559-580.
- DESCOSTES, M., SCHLEGEL, M. L., EGLIZAUD, N., DESCAMPS, F., MISERQUE, F., & SIMONI, E. (2010). Uptake of uranium and trace elements in pyrite (FeS<sub>2</sub>) suspensions. *Geochimica et Cosmochimica Acta*, *74*(5), 1551-1562.
- DIAZ, R. J., & ROSENBERG, R. J. S. (2008). Spreading dead zones and consequences for marine ecosystems. *Science*, *321*(5891), 926-929.
- DORÉ, A. G. (1991). The structural foundation and evolution of Mesozoic seaways between Europe and the Arctic. *Palaeogeography, Palaeoclimatology, Palaeoecology*, *87*(1), 441-492.
- DORÉ, A. G. (1995). Barents Sea Geology, Petroleum Resources and Commercial Potential. *Arctic*, *48*(3), 207-221.
- DUFF, K. L. (1975). Palaeoecology of a bituminous shale—the Lower Oxford Clay of central England. *Palaeontology*, *18*(3), 443-482.
- FALEIDE, J. I., BJØRLYKKE, K., & GABRIELSEN, R. H. (2015). Geology of the Norwegian Continental Shelf. In BJØRLYKKE, K. (Ed.), *Petroleum Geoscience: From Sedimentary*

- Environments to Rock Physics* (pp. 603-637). Berlin, Heidelberg: Springer Berlin Heidelberg.
- FALEIDE, J. I., VÅGNES, E., & GUDLAUGSSON, S. T. (1993). Late Mesozoic-Cenozoic evolution of the south-western Barents Sea in a regional rift-shear tectonic setting. *Marine and Petroleum Geology*, 10(3), 186-214.
- GABRIELSEN, R. H., FÆRSETH, R. B., JENSEN, L. N., KALHEIM, J. E., & RIIS, F. (1990). Structural elements of the Norwegian continental shelf. *Norwegian Petroleum Directorate Bulletin*, 6 (Part I: The Barent Sea region), 1-33.
- GABRIELSEN, R. H., & KLØVJAN, O. S. (1997). Late Jurassic—early Cretaceous caprocks of the southwestern Barents Sea: Fracture systems and rock mechanical properties. In MØLLER-PEDERSEN, P. & KOESTLER, A. G. (Eds.), *Hydrocarbon Seals: Importance for Exploration and Production* (Vol. NPF Special Publications 7, pp. 73-89). Singapore: Elsevier.
- GALLEGO-TORRES, D., REOLID, M., NIETO-MORENO, V., & MARTÍNEZ-CASADO, F. J. (2015). Pyrite framboid size distribution as a record for relative variations in sedimentation rate: An example on the Toarcian Oceanic Anoxic Event in Southiberian Palaeomargin. *Sedimentary Geology*, 330, 59-73.
- GEORGIEV, S. V., STEIN, H. J., HANNAH, J. L., XU, G., BINGEN, B., & WEISS, H. M. (2017). Timing, duration, and causes for Late Jurassic–Early Cretaceous anoxia in the Barents Sea. *Earth and Planetary Science Letters*, 461, 151-162.
- GLØRSTAD-CLARK, E., FALEIDE, J. I., LUNDSCHIEN, B. A., & NYSTUEN, J. P. (2010). Triassic seismic sequence stratigraphy and paleogeography of the western Barents Sea area. *Marine and Petroleum Geology*, 27(7), 1448-1475.
- GRANTZ, A., HART, P. E., & CHILDERS, V. A. (2011). Geology and tectonic development of the Amerasia and Canada Basins, Arctic Ocean. In SPENCER, A. M., EMBRY, A. F., GAUTIER, D. L., STOUPAKOVA, A. V., & SØRENSEN, K. (Eds.), *Arctic Petroleum Geology* (Vol. 35, pp. 771-799): Geological Society, London, Memoirs.
- GROSSMAN, R. H., LIEBLING, R. S., & SCHERP, H. S. (1979). Chlorite and its relationship to pyritization in anoxic marine environments. *Journal of Sedimentary Research*, 49(2), 611-613.
- GRUNDVÅG, S. A., MARIN, D., KAIRANOV, B., ŚLIWIŃSKA, K. K., NØHR-HANSEN, H., JELBY, M. E., ESCALONA, A., & OLAUSSEN, S. (2017). The Lower Cretaceous succession of the northwestern Barents Shelf: Onshore and offshore correlations. *Marine and Petroleum Geology*, 86, 834-857.

- GUDLAUGSSON, S. T., FALEIDE, J. I., JOHANSEN, S. E., & BREIVIK, A. J. (1998). Late Palaeozoic structural development of the South-western Barents Sea. *Marine and Petroleum Geology*, 15(1), 73-102.
- HALDAR, S. K., & TIŠLJAR, J. (2014a). Metamorphic Rocks. In HALDAR, S. K. & TIŠLJAR, J. (Eds.), *Introduction to Mineralogy and Petrology* (pp. 213-232). Oxford: Elsevier.
- HALDAR, S. K., & TIŠLJAR, J. (2014b). Sedimentary Rocks. In HALDAR, S. K. & TIŠLJAR, J. (Eds.), *Introduction to Mineralogy and Petrology* (pp. 121-212). Oxford: Elsevier.
- HARDY, R., & TUCKER, M. (1988). X-ray power diffraction of sediments. In TUCKER, M. (Ed.), *Techniques in sedimentology* (pp. 191-229). London: Blackwell Science.
- HEDGES, J. I., & KEIL, R. G. (1995). Sedimentary organic matter preservation: an assessment and speculative synthesis. *Marine Chemistry*, 49(2), 81-115.
- HENRIKSEN, E., BJØRNSETH, H. M., HALS, T. K., HEIDE, T., KIRYUKHINA, T., KLØVJAN, O. S., LARSEN, G. B., RYSETH, A. E., RØNNING, K., SOLLID, K., & STOUPAKOVA, A. (2011a). Uplift and erosion of the greater Barents Sea: impact on prospectivity and petroleum systems. In SPENCER, A. M., EMBRY, A. F., GAUTIER, D. L., STOUPAKOVA, A. V., & SØRENSEN, K. (Eds.), *Arctic Petroleum Geology* (35 ed., Vol. 35, pp. 271-281). London: Geological Society.
- HENRIKSEN, E., RYSETH, A. E., LARSEN, G. B., HEIDE, T., RØNNING, K., SOLLID, K., & STOUPAKOVA, A. V. (2011b). Tectonostratigraphy of the greater Barents Sea: implications for petroleum systems. In SPENCER, A. M., EMBRY, A. F., GAUTIER, D. L. S., A V, & SØRENSEN, K. (Eds.), *Arctic Petroleum Geology* (Vol. 35, pp. 163-195). London: Geological Society Memoir No. 35.
- HILDEBRANDT, C., & EGENHOFF, S. (2007). Shallow-marine massive sandstone sheets as indicators of palaeoseismic liquefaction — An example from the Ordovician shelf of Central Bolivia. *Sedimentary Geology*, 202(4), 581-595.
- HILLIER, R. D., & COSGROVE, J. W. (2002). Core and seismic observations of overpressure-related deformation within Eocene sediments of the Outer Moray Firth, UKCS. *Petroleum Geoscience*, 8(2), 141-149.
- HUANG, W.-L., LONGO, J. M., & PEVEAR, D. R. (1993). An Experimentally Derived Kinetic Model for Smectite-to-Illite Conversion and Its Use as a Geothermometer. *Clays and Clay Minerals*, 41(2), 162-177.
- HUNT, J. M. (1996). How Oil Forms: Generated Hydrocarbons. In HUNT, J. M. (Ed.), *Petroleum Geochemistry and Geology* (2 ed., pp. 743). New York: W.H. Freeman.

- HURST, A., SCOTT, A., & VIGORITO, M. (2011). Physical characteristics of sand injectites. *Earth-Science Reviews*, 106(3), 215-246.
- INDREVAER, K., GAC, S., GABRIELSEN, R. H., & FALEIDE, J. I. (2017). Crustal-scale subsidence and uplift caused by metamorphic phase changes in the lower crust a model for the evolution of the Loppa High area, SW Barents Sea from late Paleozoic to present. *Journal of the Geological Society of London*, 175(3), 497-508.
- JACOB, H. (1989). Classification, structure, genesis and practical importance of natural solid oil bitumen (“migrabitumen”). *International Journal of Coal Geology*, 11(1), 65-79.
- JAKOBSSON, M., MAYER, L., COAKLEY, B., DOWDESWELL, J. A., FORBES, S., FRIDMAN, B., HODNESDAL, H., NOORMETS, R., PEDERSEN, R., & REBESCO, M. (2012). The international bathymetric chart of the Arctic Ocean (IBCAO) version 3.0. *Geophysical Research Letters*, 39, 1-6.
- JARVIE, D. M., HILL, R. J., RUBLE, T. E., & POLLASTRO, R. M. (2007). Unconventional shale-gas systems: The Mississippian Barnett Shale of north-central Texas as one model for thermogenic shale-gas assessment. *AAPG Bulletin*, 91(4), 475-499.
- JESSEN, G. L., LICHTSCHLAG, A., RAMETTE, A., PANTOJA, S., ROSSEL, P. E., SCHUBERT, C. J., STRUCK, U., & BOETIUS, A. (2017). Hypoxia causes preservation of labile organic matter and changes seafloor microbial community composition (Black Sea). *Science Advances*, 3(2), e1601897.
- JOHNSON, R. A., & WICHERN, D. W. (2003). *Applied multivariate statistical analysis* (Vol. 5). Upper Saddle River, N.J: Pearson Prentice Hall.
- JONK, R., CRONIN, B., & HURST, A. (2007). Variations in sediment extrusion in basin-floor, slope, and delta-front settings: Sand volcanoes and extruded sand sheets from the Namurian of County Clare, Ireland. In HURST, A. C., J. (Ed.), *Sand injectites: Implication for hydrocarbon exploration and production* (pp. 221–226.): AAPG Memoir 87.
- KAIRANOV, B., MARÍN, D., ESCALONA, A., & CARDOZO, N. (2019). Growth and linkage of a basin-bounding fault system: Insights from the Early Cretaceous evolution of the northern Polhem Subplatform, SW Barents Sea. *Journal of Structural Geology*, 124, 182-196.
- KOEVOETS, M. J., HAMMER, Ø., OLAUSSEN, S., SENGER, K., & SMELROR, M. (2018). Integrating subsurface and outcrop data of the Middle Jurassic to Lower Cretaceous Agardhfjellet Formation in central Spitsbergen. *Norwegian Journal of Geology*, 98(4), 1-34.

- LANGMUIR, D. (1978). Uranium solution-mineral equilibria at low temperatures with applications to sedimentary ore deposits. *Geochimica et Cosmochimica Acta*, 42(6, Part A), 547-569.
- LANGMUIR, D. (1997). The Geochemistry of Clay Minerals. In LANGMUIR, D. (Ed.), *Aqueous environmental geochemistry* (pp. 312-342). Upper Saddle River, N.J: Prentice Hall.
- LECKIE, M., YURETICH, R. F., SNOEYENBOS-WEST, O., FINKELSTEIN, D., & SCHMIDT, M. (1998). Paleooceanography of the southwestern Western Interior Sea during the time of the Cenomanian/Turonian Boundary (Late Cretaceous). In WALTER E. DEAN & ARTHUR, M. A. (Eds.), *Stratigraphy and paleoenvironments of the Cretaceous Western Interior Seaway, USA. SEPM Concepts in Sedimentology and Paleontology* (Vol. 6, pp. 101-126). Tulsa: Society of Economic Paleontologists and Mineralogists.
- LEITH, T. L., WEISS, H. M., MØRK, A., ÅRHUS, N., ELVEBAKK, G., EMBRY, A. F., BROOKS, P. W., STEWART, K. R., PČELINA, T. M., BRO, E. G., VERBA, M. L., DANYUSHEVSKAYA, A., & BORISOV, A. V. (1993). Mesozoic hydrocarbon source-rocks of the Arctic region. In VORREN, T. O., BERGSAGER, E., DAHL-STAMNES, Ø. A., HOLTER, E., JOHANSEN, B., LIE, E., & LUND, T. B. (Eds.), *Arctic Geology and Petroleum Potential* (Vol. NPF Special Publications 2, pp. 1-25). Amsterdam: Elsevier.
- LEVENTHAL, J. (1993). Metals in Black Shales. In ENGEL, M. H. & MACKO, S. A. (Eds.), *Organic Geochemistry: Principles and Applications* (pp. 581-592). Boston, MA: Springer US.
- LØSETH, H., WENSAAS, L., & GADING, M. (2011a). Deformation structures in organic-rich shales. *AAPG Bulletin*, 95(5), 729-747.
- LØSETH, H., WENSAAS, L., GADING, M., DUFFAUT, K., & SPRINGER, M. (2011b). Can hydrocarbon source rocks be identified on seismic data? *Geology*, 39(12), 1167-1170.
- MARÍN, D., ESCALONA, A., GRUNDEVÅG, S.-A., NØHR-HANSEN, H., & KAIRANOV, B. (2018). Effects of adjacent fault systems on drainage patterns and evolution of uplifted rift shoulders: The Lower Cretaceous in the Loppa High, southwestern Barents Sea. *Marine and Petroleum Geology*, 94, 212-229.
- MIDDLETON, G. (1993). Sediment deposition from turbidity currents. *Annual Review of Earth and Planetary Sciences*, 21(1), 89-114.
- MØRK, A., DALLMANN, W. K., DYPVIK, H., JOHANNESSEN, E. P., LARSEN, G. B., NAGY, J., NØTTVEDT, A., OLAUSSEN, S., PČELINA, T. M., & WORSLEY, D. (1999). Mesozoic Lithostratigraphy. In DALLMANN, W. K. (Ed.), *Lithostratigraphic lexicon of Svalbard*:

- review and recommendations for nomenclature use : Upper Palaeozoic to Quaternary bedrock* (pp. 127-214). Tromsø: Norsk polarinstitutt.
- NADEAU, P. H., & REYNOLDS, R. C. (1981). Burial and Contact Metamorphism in the Mancos Shale. *Clays and Clay Minerals*, 29(4), 249-259.
- NAGAO, S., NARITA, H., TSUNOGAI, S., HARADA, K., & ISHII, T. J. G. J. (1992). The geochemistry of pore water uranium in coastal marine sediments from Funka Bay, Japan. 26(2), 63-72.
- NPD. (2019). Norwegian Petroleum Directorate Factpages. Retrieved from <https://npdfactpages.npd.no/factpages/Default.aspx?culture=en>
- NYLAND, B., JENSEN, L. N., SKAGEN, J., SKARPNES, O., & VORREN, T. (1992). Tertiary Uplift and Erosion in the Barents Sea: Magnitude, Timing and Consequences. In LARSEN, R. M., BREKKE, H., LARSEN, B. T., & TALLERAAS, E. (Eds.), *Structural and Tectonic Modelling and its Application to Petroleum Geology* (Vol. 1, pp. 153-162). Amsterdam: Elsevier.
- ODIN, G. S., & MATTER, A. (1981). De glauconiarum origine. *Sedimentology*, 28(5), 611-641.
- OHM, S. E., KARLSEN, D. A., & AUSTIN, T. J. F. (2008). Geochemically driven exploration models in uplifted areas: Examples from the Norwegian Barents Sea. *AAPG Bulletin*, 92(9), 1191-1223.
- OLJEDIREKTORATET. (2019). *Petroleumsvirksomhet i nordområdene*. (OD-15-17). Retrieved from <https://www.npd.no/globalassets/1-npd/publikasjoner/rapporter/petroleumsvirksomhet-i-nordomradene.pdf>
- OWEN, G. (2003). Load structures: gravity-driven sediment mobilization in the shallow subsurface. *Geological Society, London, Special Publications*, 216(1), 21-34.
- PETROV, O. V., SOBOLEV, N. N., KOREN, T. N., VASILIEV, V. E., PETROV, E. O., LARSEN, G. B., & SMELROR, M. (2008). Palaeozoic and Early Mesozoic evolution of the East Barents and Kara Seas sedimentary basins. *Norwegian Journal of Geology*, 88(4), 227-234.
- PEVEAR, D. R., DETHIER, D. P., & FRANK, D. (1982). Clay Minerals in the 1980 Deposits from Mount St. Helens. *Clays and Clay Minerals*, 30(4), 241-252.
- POTTER, P. E., MAYNARD, J. B., & DEPETRIS, P. J. (2005). Burial. In POTTER, P. E., MAYNARD, J. B., & DEPETRIS, P. J. (Eds.), *Mud and mudstones : introduction and overview* (pp. 55-73). Berlin: Springer.
- RIDER, M. H. (1990). Gamma-ray log shape used as a facies indicator: critical analysis of an oversimplified methodology. In HURST, A., LOVELL, M. A., & MORTON, A. C. (Eds.),

- Geological Applications of Wireline Logs* (Vol. 48, pp. 27-37). London: Geological Society Special Publications.
- RIIS, F., & FJELDSKAAR, W. (1992). On the magnitude of the Late Tertiary and Quaternary erosion and its significance for the uplift of Scandinavia and the Barents Sea. In LARSEN, R. M., BREKKE, H., LARSEN, B. T., & TALLERAAS, E. (Eds.), *Structural and Tectonic Modelling and its Application to Petroleum Geology* (Vol. 1, pp. 163-185). Amsterdam: Elsevier.
- RITZMANN, O., & FALEIDE, J. I. (2007). Caledonian basement of the western Barents Sea. *Tectonics*, 26(5).
- ROJO, L. A., & ESCALONA, A. (2018). Controls on minibasin infill in the Nordkapp Basin: Evidence of complex Triassic syndepositional deposition influenced by salt tectonics. *AAPG Bulletin*, 102(7), 1239-1272.
- RUSSELL, W. L. (1941). Well logging by radioactivity *Bulletin of the American Association of Petroleum Geologists*, 25(9), 1768-1788.
- SMELROR, M., MØRK, A., MØRK, M. B. E., WEISS, H. M., & LØSETH, H. (2001). Middle Jurassic-Lower Cretaceous transgressive-regressive sequences and facies distribution off northern Nordland and Troms, Norway. In MARTINSEN, O. J. & DREYER, T. (Eds.), *Sedimentary Environments Offshore Norway - Paleozoic to Recent* (Vol. NPF Special Publication, pp. 211-232). Amsterdam: Elsevier Science B.V.
- SMELROR, M., PETROV, O., LARSEN, G. B., & WERNER, S. (2009). *Atlas: Geological history of the Barents Sea*. Trondheim: Geological Survey of Norway.
- SPIRAKIS, C. S. (1996). The roles of organic matter in the formation of uranium deposits in sedimentary rocks. *Ore Geology Reviews*, 11(1), 53-69.
- SRODON, J. (1999). Use of clay minerals in reconstructing geological processes; recent advances and some perspectives. *Clay Minerals*, 34(1), 27-37.
- SURLYK, F., & NOE-NYGAARD, N. J. B. O. T. G. S. O. D. (2001). Sand remobilisation and intrusion in the Upper Jurassic Hareelv Formation of East Greenland. 48, 169-188.
- SWANSON, V. E. (1960). *Oil yield and uranium content of black shales* (356A). Retrieved from Washington: <http://pubs.er.usgs.gov/publication/pp356A>
- TAYLOR, J. D., & LEWIS, M. S. (1970). The flora, fauna and sediments of the marine grass beds of Mahé, Seychelles. *Journal of Natural History*, 4(2), 199-220.
- TRIPLEHORN, D. M. (1965). Origin and Significance of Glauconite in the Geologic Sequence. *Tulsa Geological Digest*, 33, 282-283.

- VELDE, B., & VASSEUR, G. (1992). Estimation of the diagenetic smectite to illite transformation in time-temperature space. *American Mineralogist*, 77(9-10), 967-976.
- WEAVER, C. E. (1958). Geological interpretation of argillaceous sediments: Part I. Origin and significance of clay minerals in sedimentary rocks. *AAPG Bulletin*, 42(2), 254-271.
- WEISS, H. M., WILHELMS, A., MILLS, N., SCOTCHMER, J., HALL, P. B., LIND, K., & BREKKE, T. (2000). *The Norwegian Industry Guide to Organic Geochemical Analyses*. In *NIGOGA* (pp. 102). Retrieved from <https://www.npd.no/globalassets/1-npd/regelverk/rapportering/bronner/eng/guide-organic-geochemical-analyses.pdf>
- WILKIN, R. T., BARNES, H. L., & BRANTLEY, S. L. (1996). The size distribution of framboidal pyrite in modern sediments: An indicator of redox conditions. *Geochimica et Cosmochimica Acta*, 60(20), 3897-3912.
- WORSLEY, D. (2008). The post-Caledonian development of Svalbard and the western Barents Sea. *Polar Research*, 27(3), 298-317.
- WORSLEY, D., AGDESTAIN, T., GJELBERG, J. G., KIRKEMO, K., MØRK, A., NILSSON, I., OLAUSSEN, S., STEEL, R. J., & STEMMERIK, L. (2001). The geological evolution of Bjørnøya, Arctic Norway: Implications for the Barents Shelf. *Norwegian Journal of Geology*, 81, 195-234.
- ZIEGLER, P. A. (1988). *Evolution of the Arctic-North Atlantic and the Western Tethys*. Tulsa, Oklahoma: AAPG Memoir 43.